

Non-linear transverse dynamics at the Cooler Synchrotron COSY

Citation for published version (APA):

Leunissen, L. H. A. (1997). *Non-linear transverse dynamics at the Cooler Synchrotron COSY*. [Phd Thesis 1 (Research TU/e / Graduation TU/e), Applied Physics and Science Education]. Technische Universiteit Eindhoven. <https://doi.org/10.6100/IR502906>

DOI:

[10.6100/IR502906](https://doi.org/10.6100/IR502906)

Document status and date:

Published: 01/01/1997

Document Version:

Publisher's PDF, also known as Version of Record (includes final page, issue and volume numbers)

Please check the document version of this publication:

- A submitted manuscript is the version of the article upon submission and before peer-review. There can be important differences between the submitted version and the official published version of record. People interested in the research are advised to contact the author for the final version of the publication, or visit the DOI to the publisher's website.
- The final author version and the galley proof are versions of the publication after peer review.
- The final published version features the final layout of the paper including the volume, issue and page numbers.

[Link to publication](#)

General rights

Copyright and moral rights for the publications made accessible in the public portal are retained by the authors and/or other copyright owners and it is a condition of accessing publications that users recognise and abide by the legal requirements associated with these rights.

- Users may download and print one copy of any publication from the public portal for the purpose of private study or research.
- You may not further distribute the material or use it for any profit-making activity or commercial gain
- You may freely distribute the URL identifying the publication in the public portal.

If the publication is distributed under the terms of Article 25fa of the Dutch Copyright Act, indicated by the "Taverne" license above, please follow below link for the End User Agreement:

www.tue.nl/taverne

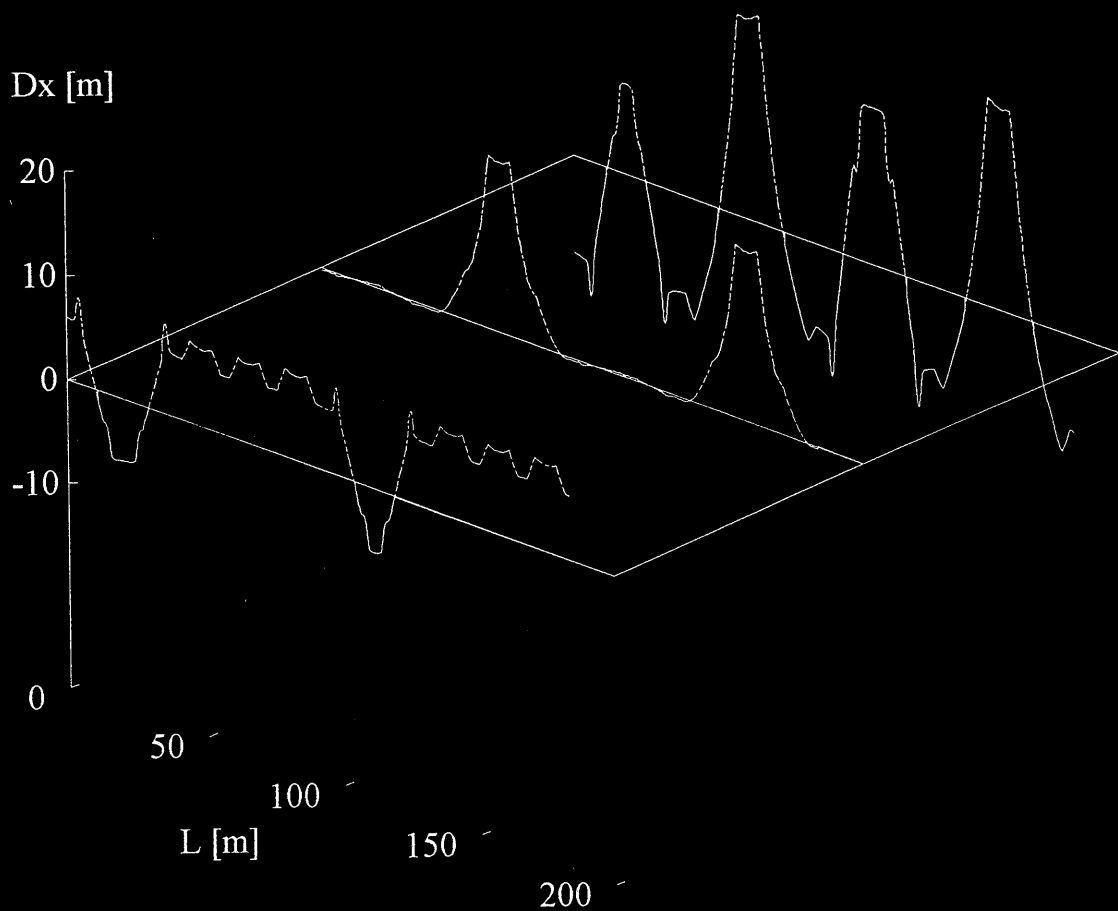
Take down policy

If you believe that this document breaches copyright please contact us at:

openaccess@tue.nl

providing details and we will investigate your claim.

Non-linear transverse dynamics at the Cooler Synchrotron COSY



L.H.A. Leunissen

Non-linear transverse dynamics
at the Cooler Synchrotron COSY

Copyright ©1997 L.H.A. Leunissen

CIP-DATA LIBRARY TECHNISCHE UNIVERSITEIT EINDHOVEN

Leunissen, Leonardus Hendrikus Albertino

Non-linear transverse dynamics at the Cooler Synchrotron COSY / by
Leonardus Hendrikus Albertino Leunissen. -
Eindhoven : Technische Universiteit Eindhoven, 1997. -
Proefschrift.

ISBN 90-386-0617-6

NUGI 812

Trefw.: deeltjesversnellers / mechanica / niet lineaire optica / lie-algebras

Subject headings : particle accelerators / mechanics / nonlinear optics / lie algebras

Non-linear transverse dynamics
at the Cooler Synchrotron COSY

PROEFSCHRIFT

ter verkrijgen van de graad van doctor aan de
Technische Universiteit Eindhoven, op gezag van de
Rector Magnificus, prof.dr. M. Rem, voor een
commissie aangewezen door het College voor
Promoties in het openbaar te verdedigen
op maandag 8 december 1997 om 16.00 uur

door

Leonardus Hendrikus Albertino Leunissen

geboren te Heerlen

Dit proefschrift is goedgekeurd door de promotoren
prof.dr.ir. H.L. Hagedoorn
en
prof.dr. F.W. Sluijter

en de copromotor
dr. R. Maier

The work described in this thesis was carried out at the "Forschungszentrum Jülich",
Jülich, Germany.

*Aan mijn ouders
en Angelique*

Cover illustration: the curves represent the calculated dispersion function during acceleration to maximal energy. The changing of the dispersion shifts transition energy and demonstrates the flexibility of the ion optics in the accelerator.

Contents

1	Introduction	1
1.1	General layout	1
1.2	Electron cooling	4
1.3	Stochastic cooling	5
1.4	Acceleration structure	7
1.5	Magnets	7
1.5.1	Dipole magnets	8
1.5.2	Quadrupole magnets	8
1.5.3	Sextupole magnets	8
1.6	Beam diagnostics	9
1.7	General concept of particle motion	10
1.8	Scope of this thesis	11
2	Basic concepts	15
2.1	Introduction	15
2.2	Hamilton equations	15
2.3	Expansion of the magnetic field	17
2.4	The linear equations of motion	18
2.5	Action angle variables for the linear equations of motion	19
2.6	Lattice of COSY	19
3	Linear modeling of the accelerator	27
3.1	Closed orbit description	27
3.1.1	Horizontal closed orbit	30
3.1.2	Vertical closed orbit	34
3.2	Calculation of the effective quadrupole gradient	35
3.2.1	Telescope quadrupole and steerer	36
3.2.2	Dipole with C- or H-steerer	37
3.2.3	Dipole with quadrupole	38
3.3	Modeling	39
3.4	Measurements	41
3.4.1	Steerer measurements at 295 MeV/c	41
3.4.2	Comparison with other energies	42

3.5	Orbit correction	44
3.6	Orbit bumps	47
4	Higher-order modeling of the accelerator	53
4.1	Multipole coefficients of dipole magnets	53
4.1.1	Tune-shift due to dipoles	57
4.2	Hamilton formalism for non-linear equations	59
4.3	Non-linear resonances	60
4.3.1	Third-order resonance	61
4.3.2	Fifth-order resonance	63
4.4	Measurements of resonances	65
4.4.1	Measurement of the linear coupling resonance $Q_x - Q_z$	66
4.4.2	Measurement of third integer resonance 1	72
4.4.3	Measurement of third integer resonance 2	74
4.4.4	Calibration of the fast quadrupole by means of the half integer resonance	78
5	Determination of Hamilton coefficients	83
5.1	Non-linear equations of motion	83
5.1.1	Factorisation properties of Lie transformations	85
5.2	Non-linear Hamiltonian coefficients	85
5.3	Example: magnetic sextupole	86
5.3.1	First-order terms	88
5.3.2	Second-order terms	88
5.4	Third-order Hamiltonian coefficients	90
5.5	Calculation of third-order Hamilton orbit response	92
5.6	Simulations of orbit response	93
5.7	Wobbling measurements	99
5.7.1	Introduction	99
5.7.2	Unperturbed measurement with steerer magnets	100
5.7.3	Evaluation of data	101
5.7.4	Amplitude dependence of non-linear terms	103
5.7.5	Measurement errors	110
6	Conclusions	113
	Appendix	115
	Summary	118
	Samenvatting	120
	Nawoord	122
	Danksagung	123
	Curriculum Vitae	124
	Publications	125

Chapter 1

Introduction

This study was performed to investigate non-linear effects in the cooler synchrotron (COSY). Therefore, a general outline of the accelerator is presented first. Then, elements of the accelerator ring are pointed out and explained briefly. Finally, an outline of the present study as described in this thesis is given.

1.1 General layout

The cooler synchrotron (COSY) at the Institut für Kernphysik (IKP) of the Forschungszentrum Jülich is an accelerator and storage ring for protons [1]. It is designed to deliver high precision beams for medium energy physics (proton momentum range from 600 to 3300 MeV/c). To accomplish this goal two cooling systems are used. First, an electron-cooling system that reaches up to a momentum of 645 MeV/c and secondly a stochastic cooling system that covers the upper momentum range from 1500 to 3300 MeV/c. Proton beams in a wide energy range have been delivered to internal as well as external experiments.

The COSY accelerator consists of several ion sources, an isochronous cyclotron, a 100 m long injection line, the COSY-ring with a circumference of 184 m and an extraction beamline to three different external experiments, see figure 1.1. The ion sources are a H^- and a H^- polarised ion source. The injector runs continuously with H^- beams which are accelerated in the cyclotron to an energy of 45 MeV. Currents of approximately 10 μ A are obtained and fed into the accelerator ring via stripping injection. The protons are then accelerated to the required energy.

The extraction beamline guides the beam to three different external experimental areas. These are the magnetic spectrometer BIG KARL [2], the Time of Flight facility (TOF) [3] and the third is a low energy measuring site where the proton momentum is limited to 800 MeV/c [4].

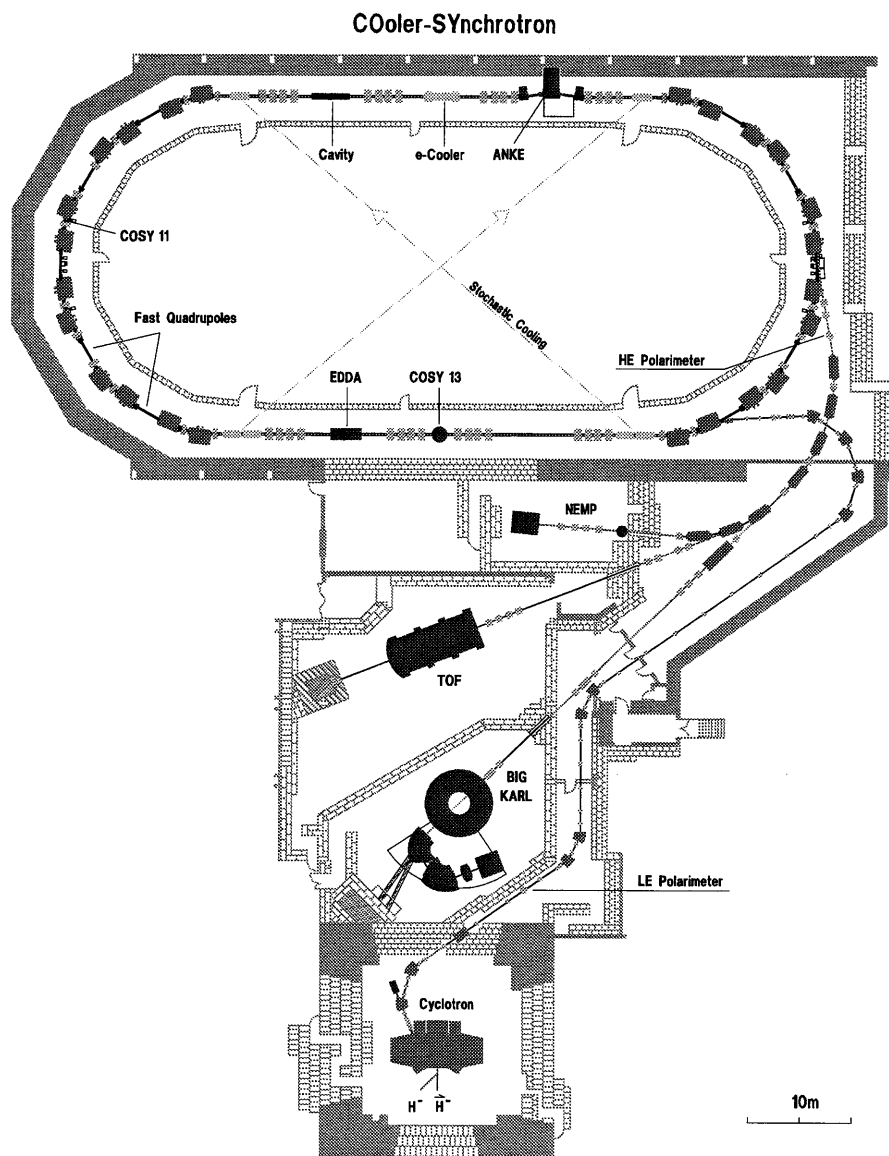


Figure 1.1: *General layout of COSY-accelerator. The WCM, BCT, Schottky-pickups and scrapers are not indicated in this figure.*

The COSY-ring has a race-track design with 40 m long straight sections. Sixteen quadrupoles in each of these sections grouped as four quadruplets allow the ion optics to be tuned such that the sections act as telescopes with a 1:1 imaging giving either a π or a 2π phase advance. One straight section contains the accelerating RF-cavity, the electron cooler, kicker electrodes for stochastic cooling, scrapers, the 0° -facility ANKE [6] and the beam current transformer. The other straight section is used for internal experimental stations COSY13 [7] and EDDA [8], pick-up tanks for stochastic cooling and the wall current monitor. The arc sections have a length of 52 m each. They are composed of three identical unit cells that have a mirror symmetry in themselves. A half-cell has focusing quadrupole, bend, defocusing quadrupole, bend structure [5]. In total there are 24 bending magnets and 24 quadrupoles in the arcs. This structure leads to a six fold symmetry for the total magnetic lattice in the ring.

General COSY design parameters	
Particles	Protons
Lattice type	OFOBODOBOBODOBOFO
Number of cells	6
Circumference (C)	184 m
Number of protons	$2 \cdot 10^{11}$
Proton momentum (p_0)	0.28 ... 3.3 GeV/c
Kinetic energy	45 ... 2500 MeV
relative proton velocity ($\beta = v_p/c$)	0.28 ... 0.97
Revolution frequency (f_0)	0.460 ... 1.573 MHz
Mean radius	16.5 m
Betatron tune Q_x, Q_z	3.5 ... 3.7, 3.5 ... 3.7
Energy gain per turn	1.28 keV (ramping speed dipoles 1 T/s)
Ramping speed	± 1 GeV/s
Average beam current	15 ... 50 μ A
Number of dipole magnets	24
Curvature bending magnet (ρ)	7 m
Magnetic field of the dipoles	0.13 ... 1.8 T
Number of quadrupoles	56
Harmonic number ($h = f_c/f_0$)	1
Peak RF structure power	100 kW
Average RF power	10 kW

Table 1.1: *General parameters of the COSY accelerator.*

In one arc section the following elements are located: the stripping foil and bumper magnets for injection, the Schottky-pickups, the electrostatic and magnetic septum for extraction. The other arc contains the diagnostic kicker and the elements for ultra slow extraction and the internal target station COSY11 [9]. In this arc two extra air-quadrupoles are present which are used for the preservation of the spin of polarised protons. Polarimeters in the injection beamline and the extraction

beamline are installed to detect the degree of polarisation. In table 1.1 the general design parameters of the COSY-accelerator are shown.

The interaction between the beam and the remaining gas in the vacuum chamber (mainly Coulomb scattering) limits the lifetime of the beam. To ensure sufficient lifetime of the beam (26 sec at injection energy) the COSY vacuum is specified to operate at an average pressure of 10^{-8} Pa in the cooler-ring.

1.2 Electron cooling

The electron cooler has been designed, constructed and tested during the years 1989 to 1992. Then the electron cooler was mounted in the COSY ring and first cooling tests took place in 1993.

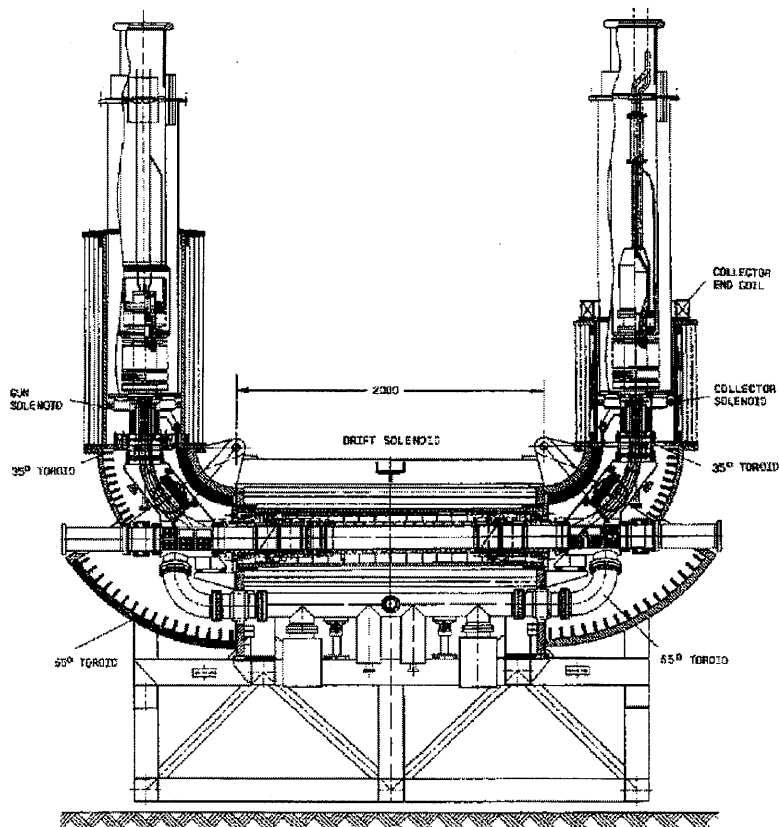


Figure 1.2: Schematic view of electron cooler.

The COSY electron cooler is designed for electron energies between 20 and 100 keV and an electron current up to 4 A. With these parameters COSY is able to provide high brilliance proton beams at energies between 40 and 200 MeV (270 MeV/c - 645 MeV/c) [10].

A continuous mono-energetic electron beam is superimposed to the proton beam by means of a toroidal field, see schematic picture of figure 1.2. The maximal solenoid field of the electron cooler amounts to 0.15 T. The electrons are allowed to interact with the protons in an area of approximately two meters length. When we look at the interacting system from a co-moving reference frame, we will see that the protons move through the electron cloud with different directions and velocities. The protons gain or lose energy through Coulomb interaction in the electron cloud. The proton energy is changed so they move with the velocity of the electrons at the end of the cooling period. During the interaction, the transverse motion of the protons is reduced, and the transverse motion of the electrons increased. This is repeated in every turn (500000 times per second), so that the beam size in transverse direction is decreased. The result is an emittance of approximately 0.3π .mm.mrad in the horizontal plane and 0.4π .mm.mrad in the vertical plane. The uncooled proton beam emittance is about 60π .mm.mrad in the horizontal plane and 15π .mm.mrad in the vertical plane. The momentum spread is decreased by approximately a factor 10 (from $2 \cdot 10^{-3}$ to $1 \cdot 10^{-4}$).

The cooling time depends on several parameters like the electron-density (n_e) and the kinetic energy of the protons (γ). When the width of the proton velocity distribution is larger then of the electrons simple scaling laws for the cooling time (τ) can be used [11]:

$$\begin{aligned} \tau &\propto \frac{1}{n_e}, \\ \tau &\propto \gamma^2 \end{aligned} \quad (1.1)$$

τ is independent of the number of protons. The cooling time is in the order of several seconds.

1.3 Stochastic cooling

At higher energies (> 200 MeV), the beam has to be cooled with other means. In this case, stochastic cooling is used which consists of pick-ups and kickers [12]. The pick-up detects a deviation of the centre of the charged cloud of a bunch of protons with respect to the reference trajectory, see schematic picture in figure 1.3. This deviation is corrected by a kicker that is situated downstream in the accelerator. The protons in the ring have small deviations in position and angle from the ideal reference trajectory. Through focusing, the deviations are kept small and the particles oscillate around the reference trajectory. To damp these oscillations a stochastic cooling system is installed in the following manner: every turn the pick-up electrode measures the position of the protons. The amplitude of the signal is a measure for the deviation of the protons (measurement between 1.0 and 3.0 GHz). The signal is amplified and sent to the kicker electrode to compensate the deviation from the reference orbit. In the simplest case the pick-up consists of

two parallel plates and the kicker electrode is built in a similar way. The kicker modifies the proton path by applying a high frequency electric field on the plates. At this moment the stochastic cooling is not yet complete, only the pick-up tanks and vertical kickers are installed.

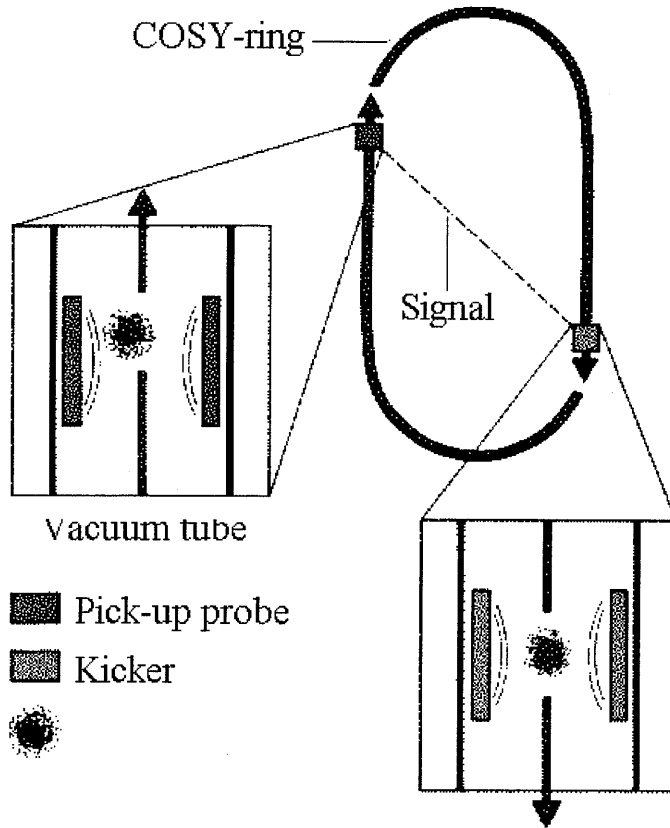


Figure 1.3: *Schematic view of stochastic cooling.*

The cooling time for the stochastic cooling is proportional to the proton density (n_p). A crude estimate of the cooling time is given by:

$$\tau \approx n_p 10^{-8} s. \quad (1.2)$$

The time required for transverse cooling from emittances of 5π .mm.mrad to about 1π .mm.mrad for 10^{10} protons at an energy of larger than 1.5 GeV will be in the order of 30 sec. Large emittances lead to smaller cooling times because the signals on the pick-ups are larger and the signal-noise ratio is improved.

1.4 Acceleration structure

The main purpose of the RF-cavity is to accelerate the injected beam to the desired energy. The particles are injected in bunches that have been formed in the cyclotron into the synchrotron [13]. A few milli-seconds after stripping injection, the beam loses its bunched structure. The beam is adiabatically bunched on the first harmonic and then accelerated. The RF-acceleration structure is a ferrite-loaded co-axial cavity of 50 kW which is driven by a programmable RF-waveform generator. The revolution frequency of the accelerated particles changes from 488 kHz to 1.6 MHz. The operation of the cavity can be separated into three different tasks: First of all, the injected beam has to be captured in "standing buckets" without acceleration.

Particles moving through an accelerating structure (cavity) will see a time varying electric field. The voltage changes as function of time to give the particle an energy gain. The particles move through the accelerating structure at different times and will gain more or less energy and need less or more time to complete one revolution. In this time-dependent field the particles perform synchrotron oscillations ensuring longitudinal stability of the beam.

Cavity tuning is possible with a pre-magnetisation of the ferrite rings inside the cavity by loop currents. These change the magnetic permeability, thereby changing the cavity's inductance. A second control task is to keep the bunch and the RF-cavity voltage at a predetermined phase. During acceleration (the particle energy is increased) this phase is nonzero and at areas of constant energy (flat bottom of flat top) the phase is returned to zero.

1.5 Magnets

In general, the magnets of the synchrotron have to be ramped synchronously with the accelerating RF-cavity during acceleration from their values at injection energy to their value at the desired energy. The acceleration is started after the phase of the bucket with respect to the RF-voltage ($\phi_s = 0$) is unequal to zero ($\phi_s \neq 0$). How fast ϕ_s is changed depends on the guiding field change. When the phase-angle is increased, the RF-amplitude (U_0) has to be increased to maintain the available phase-space. The dipole magnets can be ramped with a maximal speed of $dB/dt = 1$ T/s. Therefore, the RF-cavity needs to compensate the change of magnetic rigidity with a maximal energy-gain of:

$$\Delta T_{max} = eU_0 \sin \phi_s. \quad (1.3)$$

With an RF-amplitude of 5 kV the corresponding phase-angle is 15 degree and the maximal energy-gain is 1.28 keV. The quadrupole fields are increased during acceleration too to maintain the focusing. To give the reader an idea of the magnets that are present in the accelerator, the following summation is made in the next subsections.

1.5.1 Dipole magnets

The main magnet system of the cooler synchrotron consists of 24 dipoles. All the 24 dipoles are connected and fed by one power supply in which the current can vary between about 300 A and 5000 A. This corresponds to a magnetic induction in the middle of the magnet between 0.13 T and 1.8 T. The bending angle $\alpha = \int Bdl/B\rho$ must be the same for all 24 dipole magnets. This requires an identity of $\int Bdl$ between the bending magnets better than $2 \cdot 10^{-4}$. For correction of the magnetic length, which defines the bending angle, the pole endpieces are removable and allow us to shim the length by adding or removing sheets of lamination with different thickness. The $\int Bdl$ was measured for all dipoles at 300 A, 1120 A, 2244 A, 3885 A and 5000 A as function of the transverse position in the median plane.

For the correction of the proton beam 40 correction dipoles are introduced in the lattice. These magnets are designed to deflect the protons by about 1 mrad at maximal energy. There are two kind of steering magnets. Windowframe magnets (H-steerers) having a length of 100 mm or 200 mm and c-shaped steerer magnets (C-steerers) because they have to share the place with pumping nozzles of the vacuum system.

1.5.2 Quadrupole magnets

There are two kinds of quadrupole magnets installed in the accelerator ring. The two types differ only in their mechanical length. The 32 quadrupoles in the straight sections are called MQT's and have an iron length of 570 mm, the 24 quadrupoles in the arcs are 300 mm long and are called MQU's. The aperture is 170 mm and the maximal gradient inside the magnet is 7.6 T/m. The quadrupole magnets are grouped into 14 different families, where each family has its own power supply with a maximal current of 550 A. Four quadrupoles are connected with each other which yields 6 families, MQU1 to MQU6. In each telescope we have four families, each consisting of 4 quadrupoles. This is explained further in the next chapter.

1.5.3 Sextupole magnets

The sextupole magnets are used for correction of non-linear magnetic fields that are present due to non-ideal dipole and quadrupole magnets. They are also used for chromaticity control, that is to change the betatron oscillation frequency as function of the momentum-deviation of the protons. There are three different types of sextupole magnets in the COSY machine. The differences between the magnets are the iron length and the aperture. The 12 MXL sextupoles have an iron length of 200 mm, the 4 MXS sextupoles of 90 mm and the 2 MXG sextupoles of 260 mm. The apertures of the MXL and MXS sextupoles are both equal to 170 mm, for the MXG sextupoles the aperture is 250 mm. All MXS sextupoles are positioned in the arcs of the ring and connected to one power supply. The MXG sextupoles are each situated in the middle of an arc and connected to their own power supply. Four sextupoles of the type MXL are also positioned in the arc and connected to one power supply. All other MXL sextupoles have an individual power supply and in

each quadruplet in the telescope section one sextupole is placed. The power supplies yield a maximal current of 300 A which gives a maximal strength of 37 T/m^2 for the MXL and MXS sextupoles and 31 T/m^2 for the MXG sextupoles, respectively.

1.6 Beam diagnostics

For diagnostic purposes several elements are present which are described below [14].

A *wall current monitor* (WCM) is used for monitoring the bunches of the circulating beam. A *beam current transformer* (BCT) is designed to measure the DC-current of the stored coasting beam. It is also used for mean value measurements of the RF-bunched beam current and the BCT is useful for a qualitative look on performance and losses of COSY during ramping. To do beam position diagnostics, 29 horizontal and 27 vertical *beam position monitors* (BPM's) are available around the ring. The BPM consists of two electrostatic pick-ups, see figure 1.4, where the difference of the two signals determines the transverse displacement of the beam and the sum of both signals the longitudinal spectrum. These signals are digitized and can be used to read out the beam position in the horizontal and vertical plane.

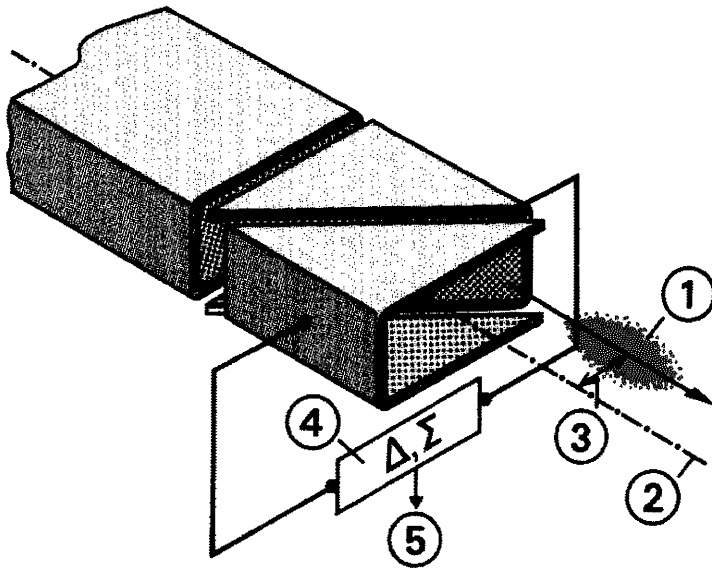


Figure 1.4: *Beam position monitor with (1) bunch, (2) centre of BPM, (3) deviation of bunch, (4) sum- and difference signal. The measured signals are digitised and evaluated (5).*

Schottky pick-ups are utilised to measure the longitudinal (sum of electrode signals) and transverse (difference of the signals) Schottky-noise spectrum. By means

of resonant tuning the sensitivity is enhanced (narrow band) and shifted to a proper frequency band. The longitudinal Schottky-noise spectrum is used to determine the revolution frequency and from it the particle energy, the relative momentum spread of the particles and the synchrotron frequency. The transverse Schottky-noise spectrum allows the determination of the non-integer part of the betatron oscillation (tune), of chromaticity, beam emittance and closed orbit displacement. At COSY two pick-ups, each 1 m long, are installed for horizontal and vertical measurements. They are electrostatic pick-ups with electrodes 70 mm apart.

The purpose of a *kicker* is to excite the beam particles to collective transverse oscillations, running with betatron frequency. This method allows a fast determination of the non-integer part of the tune and, in addition, can be performed with a higher sensitivity as can be achieved by transverse Schottky-noise measurements. By means of the kicker magnet the beam is deflected within one turn and the resulting beam position oscillations is measured in one BPM for, i.e. up to 200 successive turns. The number of betatron oscillations are determined by $q = N/n$, with N the number of oscillations around the reference trajectory in transverse direction and n the number of turns. Via a *stripline unit* the beam is excited with a frequency tracked RF-voltage. A resonance occurs if the exciting frequency corresponds to a combination of betatron frequency and a harmonic of the revolution frequency, thus enabling to measure the betatron oscillations during acceleration.

To measure the tune during the acceleration ramp the resonant excitation by the stripline unit and with the kicker-deflection can be used. The stripline unit can be used for horizontal and vertical beam deflections, whereas the kicker magnet is suitable only for the horizontal plane.

1.7 General concept of particle motion

A central trajectory (reference orbit) is defined in the median plane, which is a plane of symmetry perpendicular to the vertical axis with a curvilinear coordinate system (s, x, z) . In general, the equations of motion are non-linear. In figure 1.5, x is taken radially and z is taken to be vertical. The coordinate s denotes the arc length along the reference orbit. The particles deviating from the central trajectory will execute betatron oscillations.

The linear equations of motion in the x and z direction ($y \in \{x, z\}$) are given by:

$$\frac{d^2y}{ds^2} + \left(\frac{1}{\rho^2(s)} - K_y(s) \right) y = \frac{1}{\rho(s)} \left(\frac{\Delta p}{p} \right) = \frac{\delta}{\rho(s)}. \quad (1.4)$$

where $K_y(s) = -(dB/dy)/(p/e)$ and $\rho(s) = (p/e)/B(s)$. Here $\rho(s)$ is the local radius of curvature, $K_y(s)$ the focusing magnetic field, p the momentum of the particle, e the charge of the particle and Δp the momentum difference between a generic particle and a particle with a given energy travelling at the reference trajectory. The equations are examples of Hill's equation. The two independent solutions of the homogeneous equations can be described as sine- $S(s)$ and cosine- $C(s)$ -like functions. The dispersion function $D(s)$ is a solution of the inhomogeneous

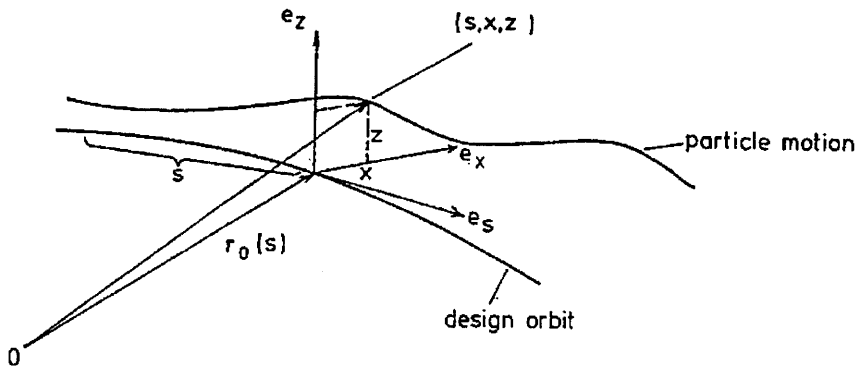


Figure 1.5: Reference trajectory and curvilinear coordinate system (s, x, z) .

equation. The solutions for the horizontal and vertical plane can be arranged in a transfer matrix $M(s)$:

$$\begin{pmatrix} y \\ y' \\ \delta \end{pmatrix} = M(s) \begin{pmatrix} y_0 \\ y'_0 \\ \delta_0 \end{pmatrix} = \begin{pmatrix} C(s) & S(s) & D(s) \\ C'(s) & S'(s) & D'(s) \\ 0 & 0 & 1 \end{pmatrix} \begin{pmatrix} y_0 \\ y'_0 \\ \delta_0 \end{pmatrix}, \quad (1.5)$$

where y_0 and y'_0 are the initial conditions ($y \in \{x, z\}$). The prime denotes differentiation with respect to s and y' is called the divergence.

1.8 Scope of this thesis

This thesis deals with the modeling of the non-linear motion in a particle accelerator with analytical and numerical tools. The layout of the accelerator has been described shortly. Then, a numerical model for the description of the ring and the beam properties is presented in which the magnetic fields are expanded to first-order. To reduce the discrepancy between the numerical calculations and experimental results a fit procedure is used and calibration factors are deduced. These calibration factors are used to improve the linear model for the accelerator. Misalignments of the optical elements in the ring, fringing fields and non-linear magnetic fields change the properties of the ideal synchrotron. These perturbations are investigated and their influence on the circulating beam are determined. For this purpose several numerical program packages are used. Then, the perturbations (e.g. misalignments and non-linear magnetic fields) are added in the model. This study was performed to investigate the deviations of the accelerator with respect to the ideal machine. In particular, when the deviations are known we can try to correct or compensate them.

Furthermore, non-linear elements (e.g. sextupoles) can be used to induce non-linear behavior in the machine. In contrast to the unintentional non-linearities

these magnets can be used to improve the optical behavior of the machine. First of all, they can be used to compensate for the magnetic field errors in the magnets. Secondly, the sextupoles can be used for extraction purposes. Their influence can be determined with analytical tools (such as perturbation theory and Lie algebraic tools which are presented here). Another method of investigation are numerical codes such as COSY INFINITY [15] and SIXTRACK [16]. Measurements were done to verify the acquired numerical and analytic results.

In chapter 2 some general concepts and analytical expressions are given. Optical properties and lattice parameters are defined and calculated in first-order in chapter 3. In chapter 4, the higher-order machine is defined and higher-order magnetic field measurements are shown. In addition, experimental results of resonances will be presented in that chapter. In chapter 5 the sextupole-induced non-linearities will be calculated. Furthermore, measurements with respect to the presented topics will be shown. In the last chapter the concluding remarks are presented.

Bibliography

- [1] R. Maier, U. Bechstedt, J. Dietrich, U. Hacker, S. Martin, D. Prasuhn, P. v. Rossen, H. Stockhorst and R. Tölle, *Status of COSY*, Proc. EPAC 94 (London) p. 165.
- [2] R. Joosten, *Aufbau und Inbetriebnahme eines hochgranularen Vertexdetektors aus szintillierenden Fasern für das Experiment MOMO an COSY; Erste Ergebnisse zur Reaktion $p + d \rightarrow {}^3\text{He} + \pi^+ + \pi^-$* , PhD-thesis
- [3] COSY proposal #9, 1990. Annual report 1991, Jül-2590, March 1992.
- [4] U. Linz and R. Maier, *A First Concept to use the Cooler Synchrotron COSY-Jülich for Cancer Therapy*, Proc. EPAC 92 (Berlin) p. 1672.
- [5] K. Bongardt, D. Dinev, S. Martin, P.F. Meads, D. Prasuhn, H. Stockhorst and R. Wagner, *The Cosy Lattice*, Proc. EPAC 90 (Nice) p. 1492.
- [6] W. Borgs et al., *Proc. Top. Conf. in Particle Production near Treshold*, Am. Inst. of Phys., Conf. Proceedings, No. 221, p.299.
- [7] O. Schult et al., *Nucl. Instr. Meth.* A585 (1995), p.247.
- [8] J. Bisplinghoff et al., *AIP Conf. Proc.* 221, Am. Inst. of Phys. 1990 p.312.
- [9] S. Brauksiepe et al., *Nucl. Instr. Meth.* A376 (1996), p.397.
- [10] R. Maier, D. Prasuhn, W. Schwab, H.J. Stein and J. Witt, *Operational characteristics of the COSY electron cooler*, Proc. EPAC 94 (London) p.1200.
- [11] R. Maier, *Strahl-optische Gesichtspunkte bei der Auslegung hochbrillanter Speicherringe*, Berichte des Forschungszentrum Jülich Jül-3120.
- [12] P. Brittner, H.U. Hacker, D. Prasuhn, G. Schug, H. Singer, W. Spieß and R. Stassen, *Stochastic cooling system in COSY*, Proc. EPAC 94 (London) p.1203.
- [13] A. Schnase, H. Rongen and H. Meuth, *A Digital Synthesizer and Phase Control System for RF-Acceleration in COSY*, Proc. EPAC 92 (Berlin) p.1220.
- [14] J. Bojowald et al., *Beam Diagnostics at COSY-Jülich*, Proc. EPAC 92 (Berlin) p.1088.

- [15] M.Berz, *COSY INFINITY User's manual*, Michigan State University Cyclotron Laboratories 869 (1993).
- [16] F.Schmidt, *SIXTRACK, Version 1, Single particle tracking code treating transverse motion with synchrotron oscillations in a symplectic manner*, CERN/SL/90-11(AP) (1990).

Chapter 2

Basic concepts

In this chapter the basic equations of the Hamilton mechanics for charged particles are given. The linear solution of these equations define several optical properties of charged particles. These properties can be calculated using numerical programs. Measurements are compared to the ideal model for the COSY synchrotron.

2.1 Introduction

First of all, a Hamiltonian is derived for a curvilinear coordinate system upto order 3. Then the equations of motion are solved to first order. A few optical functions are derived from these equations of motion, for example: beta-function and dispersion function. Assuming that the accelerator consist of an ideal machine perturbed by small "field errors", the non-linear equations of motion can be derived using this Hamiltonian. In the following chapters the Hamilton equation is expanded to keep only dominant terms (resonance approach). The governing perturbation is so large that the other terms can be neglected. The Hamilton formalism can be used to obtain the perturbations to second order as function of sextupole fields (non-linear magnetic field). To do this, Lie algebraic tools are introduced and the equations of motion are solved.

2.2 Hamilton equations

The particle motion in a magnetic field is described by a relativistic Hamiltonian H with charge e and rest mass m_0 :

$$H(\vec{x}, \vec{p}, t) = \sqrt{m_0^2 c^4 + c^2(\vec{p} - e\vec{A}(\vec{x}; t))^2} \quad (2.1)$$

where c is the speed of light and \vec{p} is the canonically conjugated momentum. Here, ϕ and \vec{A} are the scalar and a vector potential, respectively. These potentials are

defined in such a way that the electric field \vec{E} and magnetic field \vec{B} obey the relations

$$\begin{aligned}\vec{B} &= \vec{\nabla} \times \vec{A}, \\ \vec{E} &= -\vec{\nabla}\phi - \frac{\partial \vec{A}}{\partial t}.\end{aligned}\quad (2.2)$$

The canonically conjugate variables x_i and p_i are given by Hamilton's equations of motion

$$\begin{aligned}\frac{\partial x_i}{\partial t} &= \frac{\partial H}{\partial p_i}, \\ \frac{\partial p_i}{\partial t} &= -\frac{\partial H}{\partial x_i}.\end{aligned}\quad (2.3)$$

For our purpose curvilinear coordinates are used (see figure 1.5). Then the representation for H becomes

$$H_1 = c\sqrt{m_0c^2 + (p_x - eA_x)^2 + \left(\frac{p_s}{1+hx} - eA_s\right)^2} + (p_z - eA_z)^2 \quad (2.4)$$

with $h(s) = 1/\rho(s)$ where A_x , A_s and A_z are the components of the vector potential in the curvilinear system. When A_x , A_s and A_z are time-independent then H_1 is a constant of motion which is identified as the energy E with

$$H_1 = E = \sqrt{p^2c^2 + m_0^2c^4} \quad (2.5)$$

where p is the total momentum. Because H_1 is constant it is convenient to change from t to s as independent variable, and taking $-p_s$ as a new Hamiltonian. The new Hamiltonian H_2 is given by

$$H_2 = -p_s = -(1+hx) \left[eA_s + \sqrt{p^2 - (p_x - eA_x)^2 - (p_z - eA_z)^2} \right]. \quad (2.6)$$

To investigate perturbation, the square root in the Hamiltonian H_2 is expanded. We expand in powers of deviation from a reference orbit x , p_x , z , p_z and δ , where δ is defined in Eq. 1.4. After a scaling of the Hamiltonian H_2 with $H_3 = H_2/p$ we get

$$H_3 = -(1+hx) \left[\frac{e}{p}A_s + \sqrt{1 - (p_x - \frac{e}{p}A_x)^2 - (p_z - \frac{e}{p}A_z)^2} \right]. \quad (2.7)$$

Expansion of the square root yields

$$\sqrt{1+\alpha} = 1 + \frac{1}{2}\alpha - \frac{1}{8}\alpha^2 + \frac{1}{16}\alpha^3 + \mathcal{O}(4). \quad (2.8)$$

The Hamiltonian H_3 to third power is then given by

$$\begin{aligned}H_3 &= -(1+hx) \left[\frac{e}{p_0(1+\delta)}A_s + 1 - \frac{1}{2} \left(p_x - \frac{e}{p_0(1+\delta)}A_x \right)^2 - \right. \\ &\left. \frac{1}{2} \left(p_z - \frac{e}{p_0(1+\delta)}A_z \right)^2 \right] + \mathcal{O}(4).\end{aligned}\quad (2.9)$$

In Eq. 2.12 the vector potential will be expanded and then it will be shown that H_3 is of order 3.

2.3 Expansion of the magnetic field

To describe the motion in a synchrotron the magnetic field has to be given as a series in which each term corresponds to a magnetic field distribution with a certain number of poles.

In the symmetry plane $z = B_x = B_s = 0$, which is usually the situation in particle accelerators. The magnetic fields are then expanded in the curvilinear coordinates as in [2]

$$\begin{aligned}\frac{e}{p_0}B_x(s) &= k(s)z + m(s)xz + \mathcal{O}(3), \\ \frac{e}{p_0}B_s(s) &= -\frac{dh(s)}{ds}z + \mathcal{O}(2), \\ \frac{e}{p_0}B_z(s) &= -h(s) + k(s)x + \frac{1}{2}m(s)x^2 - \frac{1}{2}\left[m(s) + h(s)k(s) - \frac{d^2h(s)}{ds^2}\right]z^2 + \mathcal{O}(3).\end{aligned}\tag{2.10}$$

Here, h , k and m are the given strengths of respectively the dipole, quadrupole and sextupole by

$$\begin{aligned}h &= -\frac{e}{p_0}B_z, \\ k &= \frac{e}{p_0}\frac{\partial B_z}{\partial x} = \frac{e}{p_0}\frac{\partial B_x}{\partial z}, \\ m &= \frac{e}{p_0}\frac{\partial^2 B_z}{\partial x^2}.\end{aligned}\tag{2.11}$$

A corresponding vector potential is given by

$$\begin{aligned}\frac{e}{p_0}A_x(s) &= -\frac{1}{2}\frac{dh(s)}{ds}z^2 + \mathcal{O}(3), \\ \frac{e}{p_0}A_s(s) &= -h(s)x + \frac{1}{2}[k(s) + h^2(s)]x^2 - \frac{1}{2}k(s)z^2 + \\ &\quad \frac{1}{6}[m(s) - h(s)k(s) - 3h^3(s)]x^3 - \frac{1}{2}m(s)xz^2 + \mathcal{O}(4), \\ \frac{e}{p_0}A_z(s) &= 0 + \mathcal{O}(3).\end{aligned}\tag{2.12}$$

By using the Hamiltonian 2.9 expanded to third power in the canonical variables, and using the expansion of the vector potential as given in Eq. 2.12, a Hamiltonian is obtained of the form

$$H = H_0 + H_p,\tag{2.13}$$

with H_0 the Hamiltonian describing the linear equations of motion (terms in x , z , p_x and p_z of order two) and H_p describing the non-linear equations of motion (terms of order 3 and higher) given by:

$$\begin{aligned}H_0 &= -\delta h(s)x + \frac{1}{2}[h^2(s) - k(s)]x^2 + \frac{1}{2}k(s)z^2 + \frac{1}{2}p_x^2 + \frac{1}{2}p_z^2, \\ H_p &= \delta^2 h(s)x - \frac{1}{6}\delta[h^2(s) - k(s)]x^2 - \frac{1}{2}\delta k(s)z^2 - \frac{1}{6}[m(s) + 2h(s)k(s)]x^3 + \\ &\quad \frac{1}{2}[m(s) + h(s)k(s)]xz^2 + \frac{1}{2}\frac{dh(s)}{ds}z^2 p_x + \frac{1}{2}h(s)x p_x^2 + \frac{1}{2}h(s)x p_z^2 + \mathcal{O}(4).\end{aligned}\tag{2.14}$$

2.4 The linear equations of motion

First the linear equations of motion and their solution are discussed. These results are already derived by Courant & Snyder, see ref. [1]. The linear dispersion function and the action-angle variables are introduced.

The linear equations of motion follow from H_0 as given in Eq. 2.14:

$$\begin{aligned} \frac{d^2 x}{ds^2} + [h^2(s) - k(s)] x &= \delta h(s), \\ \frac{d^2 z}{ds^2} + k(s) z &= 0. \end{aligned} \quad (2.15)$$

The differential equation for the horizontal motion is inhomogeneous, it is customary to introduce a linear dispersion function $D_0(s)$ which is defined by $x(s) = \delta D_0(s)$. That is, particles with a momentum deviation δ will travel on a orbit defined by the dispersion function. For a circular accelerator the dispersion function has a periodic solution (closed orbit). By a canonical transformation this orbit is put in the centre of phase space [3]. The corresponding generating function with old coordinates and new momenta (capitals) is given by:

$$F_2(x, P_x; s) = [x(s) - x_{ref}(s)] [P_x + p_{ref}(s)] \quad (2.16)$$

where p_{ref} is obtained from $p_{ref}(s) = dx_{ref}(s)/ds = d\delta D_0(s)/ds$. For the new Hamiltonian the following equations of motion apply.

$$\begin{aligned} \frac{d^2 x}{ds^2} + [h^2(s) - k(s)] x &= 0 \\ \frac{d^2 z}{ds^2} + k(s) z &= 0 \end{aligned} \quad (2.17)$$

where small letters for the new canonical variables are used. The equations of motion have the general form

$$\frac{d^2 y}{ds^2} + K(s)y = 0 \quad (2.18)$$

where $y \in \{x, z\}$. They describe an oscillatory motion (betatron motion) around a reference curve with a restoring force $K(s)$. The force $K(s)$ is periodic for a circular accelerator. The solution in a phase-amplitude form can be obtained by the Ansatz [1]

$$y(s) = \Re \left(\sqrt{\beta_y(s)} e^{i\Psi_y(s)} \right). \quad (2.19)$$

Here, $\beta_y(s)$ is referred to as the beta-function and $\Psi(s)$ is called the betatron phase. After substitution in Eq. 2.17 and integrating twice gives

$$\Psi_y(s) = \int_{s_0}^s \frac{d\tau}{\beta_y(\tau)} + \phi_y. \quad (2.20)$$

ϕ_y is a constant given by the initial conditions. For a circular accelerator $\beta_y(s)$ is a periodic solution of Eq. 2.17. The integration of 2.20 with $s = s_0 + C$ yields the number of betatron oscillation wavelengths in one revolution, where the length of the accelerator is C and $Q_y = (\Psi(s) - \Psi(s_0))/2\pi$.

2.5 Action angle variables for the linear equations of motion

Action angle variables will be needed in chapter four. The Hamilton equation from the last section can be rewritten in action-angle variables. This is done with the generation function [4]

$$F_1(x, z, \phi_x, \phi_z; s) = -\frac{x^2}{2\beta_x(s)} [\tan \phi_x + \alpha_x(s)] - \frac{z^2}{2\beta_z(s)} [\tan \phi_z + \alpha_z(s)], \quad (2.21)$$

where for every $y \in \{x, z\}$ the function α_y is defined by

$$\alpha_y(s) \equiv -\frac{1}{2} \frac{d\beta_y(s)}{ds}. \quad (2.22)$$

The new Hamiltonian is:

$$K_0 = \frac{J_x}{\beta_x(s)} + \frac{J_z}{\beta_z(s)}, \quad (2.23)$$

with

$$\begin{aligned} J_x &= \frac{x^2}{2\beta_x(s) \cos^2 \phi_x(s)} \\ p_x &= -\frac{x}{\beta_x(s)} [\tan \phi_x(s) + \alpha_x(s)]. \end{aligned} \quad (2.24)$$

The corresponding Hamilton equations are

$$\begin{aligned} \frac{\partial J_x}{\partial t} = -\frac{\partial K_0}{\partial \phi_x} = 0, & \quad \frac{\partial \phi_x}{\partial t} = \frac{\partial K_0}{\partial J_x} = \frac{1}{\beta_x(s)}, \\ \frac{\partial J_z}{\partial t} = -\frac{\partial K_0}{\partial \phi_z} = 0, & \quad \frac{\partial \phi_z}{\partial t} = \frac{\partial K_0}{\partial J_z} = \frac{1}{\beta_z(s)}, \end{aligned} \quad (2.25)$$

If the equations are integrated, J_x and J_z are constants given by initial conditions and for ϕ_y with $y \in \{x, z\}$ the solution yields

$$\phi_y(s) = \int_{s_0}^s \frac{d\tau}{\beta_y(\tau)} + \Psi_{0,y} \quad (2.26)$$

where $\Psi_{0,y}$ the initial condition for the horizontal, respectively vertical motion is.

The relation between the old coordinates and the new coordinates is given by:

$$\begin{aligned} y &= \sqrt{2J_y \beta_y(s)} \cos \phi_y(s) \\ p_y &= -\sqrt{\frac{2J_y}{\beta_y(s)}} [\sin \phi_y(s) + \alpha_y(s) \cos \phi_y(s)]. \end{aligned} \quad (2.27)$$

2.6 Lattice of COSY

For the treatment of the numerical calculations we are going to introduce the lattice of the COSY accelerator. Some lattice functions are introduced that are calculated in this and further chapters.

The basic lattice structure of an arc consists of 12 quadrupoles and 12 dipoles which are grouped in the sequence as shown in figure 2.1. The structure of a telescope section is shown in figure 2.2. The quadrupoles in the arcs and the telescope sections are grouped into families. Each family is connected to one power supply and can be driven to a specified current. The quadrupoles Q1, Q4, Q21 and Q24 (the last two quadrupoles are situated on a mirror position in the opposite arc) are one family called MQU1. The quadrupoles Q2, Q3, Q22 and Q23 (MQU2) are another family with opposite sign for the current. The families MQU3, MQU4, MQU5 and MQU6 are build up in a similar way to yield a mirror-symmetrical FODO-structure. The space between the quadrupoles is occupied with homogeneous bending magnets (D).

The even numbered quadrupoles are driven at a current so that their strength is about 0.38 m^{-2} and the odd numbered quadrupoles have a gradient of about -0.27 m^{-2} . When γ is near transition energy ($\gamma_{tr} = 1/\sqrt{\alpha}$) the beam must cross an instable area in which the chance of beam losses is present. The momentum compaction factor α is defined by:

$$\alpha = \frac{1}{C} \oint \frac{D_x(s)}{\rho(s)} ds. \quad (2.28)$$

The phase stability of the accelerated beams is no longer on the falling side of the RF-wave when γ_{tr} is crossed. The γ_{tr} can be increased by changing the currents in MQU2 and MQU6 to 80% of their nominal value and simultaneously increasing the current of MQU4 by about 40% of their nominal value. The dispersion function is larger in the arcs and therefore γ_{tr} is increased. Then it is possible to accelerate to higher energies without crossing the transition energy.

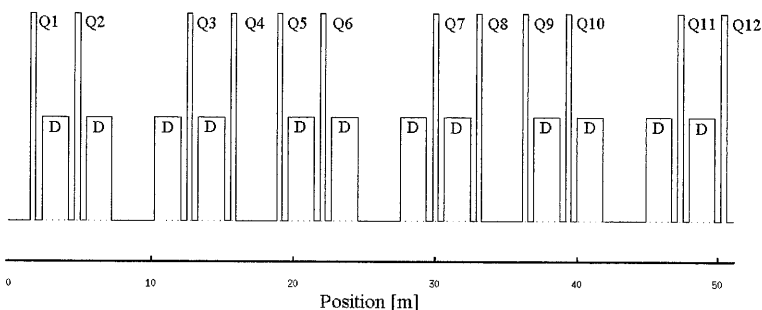


Figure 2.1: *Quadrupole and dipole magnets in one arc section.*

The 32 quadrupoles in the straight section are grouped in 8 families with one power supply called MQT's. The quadrupoles Q1, Q4, Q13 and Q16 are one family called MQT1. The quadrupoles Q2, Q3, Q14 and Q15 have an opposite sign and are the family MQT2. The eight quadrupoles near the centre are connected similarly yielding a $fddf - dfdf$ configuration with f for focusing and d for defocusing quadrupoles. The quadrupole families MQT5, ..., MQT8 in the opposite straight section are connected identically.

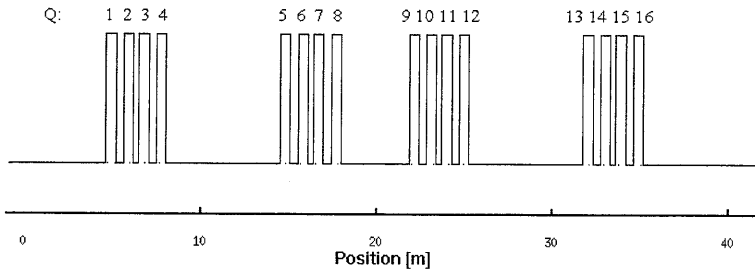


Figure 2.2: *Quadrupole magnets in straight section (target telescope).*

Each straight section consists of two mirror symmetrical quadrupole structures which may provide a 1:1 non-inverted imaging of the beam from the exit of an arc to the beginning of the other arc. The straight section is tuned such that the section acts as a 1:1 imaging with a phase advance of 2π . To achieve this, the quadrupoles have to be adjusted to make a specified gradient as shown in table 2.1. Several modes are possible, here only two are presented.

Quadrupole family	optic 1 [m^{-2}]	optic 2 [m^{-2}]
MQT1	-0.552	-0.669
MQT2	+0.516	+0.582
MQT3	+0.730	+0.669
MQT4	-0.670	-0.582
MQT5	-0.675	-0.669
MQT6	+0.622	+0.582
MQT7	+0.584	+0.669
MQT8	-0.544	-0.582

Table 2.1: *Settings of straight section to ensure phase advance of 2π .*

With the basic parameters given above and the geometrical positions of the elements known (see appendix) of the COSY-lattice the optical functions such as $\beta_x(s)$, $\beta_z(s)$, $D_x(s)$, $D_z(s)$ and the tune are calculated. The two modes, optic 1 and optic 2, correspond to settings that can be chosen for a specific imaging in the telescope [6]. For example, the two optics for the telescope section are shown in figure 2.3 and 2.4. The optic for the arc-section is not changed in the two calculations (MQU1=MQU3=MQU5=-0.27 m^{-2} and MQU2=MQU4=MQU6=0.38 m^{-2}).

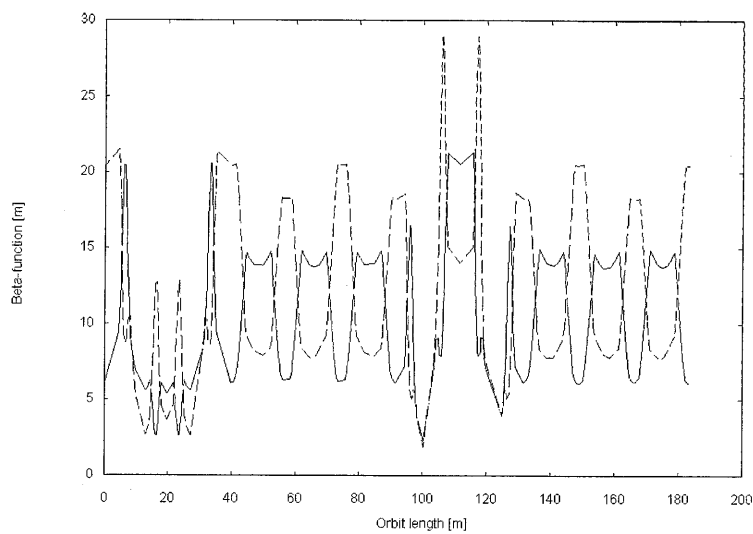


Figure 2.3: Calculated horizontal (solid line) and vertical (dashed line) β -function with optic 1.

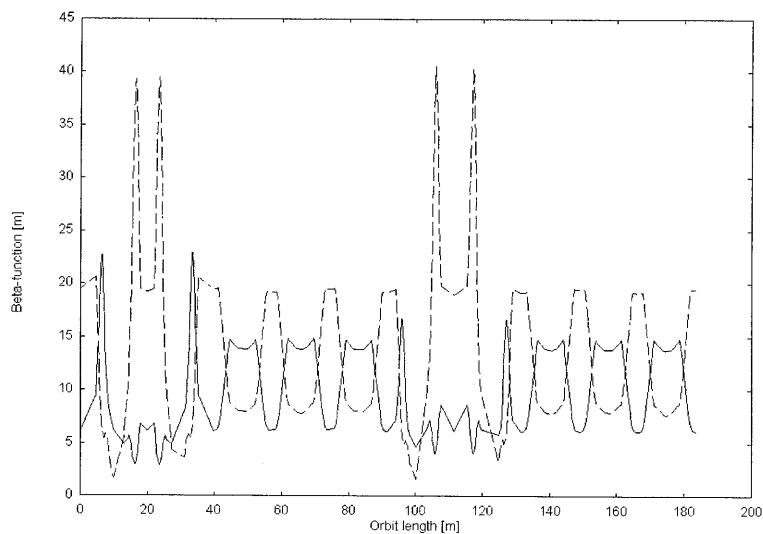


Figure 2.4: Calculated horizontal (solid line) and vertical (dashed line) β -function with optic 2.

The pictures start at the beginning of the target telescope (containing the EDDA and COSY13 experiments). The optic that is chosen depends on the optical parameters that are required for a specific experiment. For example, for electron cooling (at position 110 m in figure 2.3 and 2.4) it is necessary that the horizontal and vertical beta-functions are small. First of all, for good cooling results β_y -function must be about 5 m. Secondly, due to the toroidal magnetic fields of the electron cooler the horizontal closed orbit deviation is large in the electron cooler. To avoid beam losses, the beam diameter ($\propto \sqrt{\beta_y}$) has to be small and therefore optic 2 is preferred.

Comparison between calculation and measurements is done in table 2.2. To measure the β -function the gradient of a quadrupole family is changed about 1%. The tune in the horizontal and vertical plane is measured in both cases. The tune-shift is a measure for the β -function as shown by [5]

$$\beta_y(s) = 4\pi \frac{\Delta\nu_y}{L\Delta k_1} \quad (2.29)$$

with $\Delta\nu_y$ the tune-shift, L the quadrupole length, $\Delta k_1 = \Delta B'/B\rho$ and $\Delta B'$ is the change in the gradient of the quadrupole.

Quadrupole family	Measurement		Calculation	
	β_x [m]	β_z [m]	β_x [m]	β_z [m]
MQU1	7	15	7	20
MQU2	14	9	15	10
MQU3	7	15	7	19
MQU4	15	11	14	8
MQU5	7	15	7	20
MQU6	14	10	16	11
MQT1	16	11	11	10
MQT2	20	7	21	6
MQT3	4	33	5	21
MQT4	2	33	4	27
MQT5	9	27	6	20
MQT6	5	33	3	36
MQT7	15	10	11	12
MQT8	19	7	20	8

Table 2.2: Comparison between calculation and measurement of the averaged β_y -function.

The dispersion can be measured by applying a momentum deviation (Δp) on the closed orbit. The closed orbit is measured with and without Δp . The relation

$$x_{co} = D_x(s) \frac{\Delta p}{p_0} \quad (2.30)$$

shows the dependence of the measured closed orbit (x_{co}) on the dispersion function. The resulting measurement is shown together with a calculated curve in figure 2.5 for a typical optic before acceleration (flat bottom). The dots connected with a dashed line indicate the measured dispersion at a beam position monitor. The vertical dispersion is zero because there are no vertical dipole fields in the ring structure. This fact is confirmed by measurements.

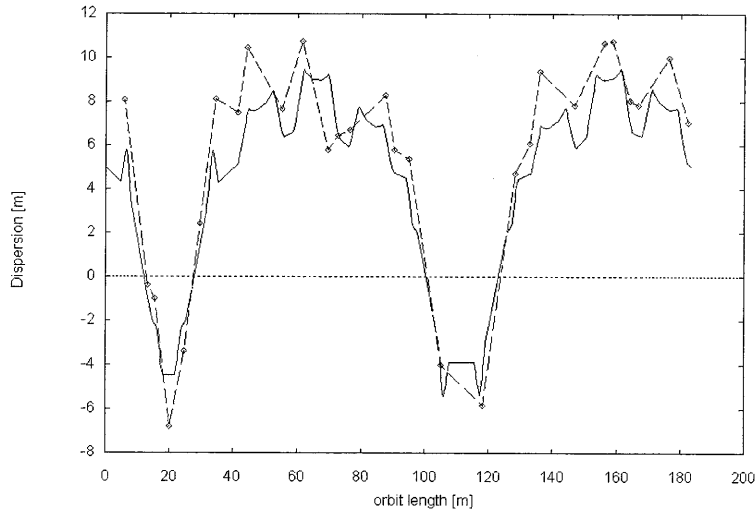


Figure 2.5: *Measured and calculated horizontal dispersion (calculation indicated with solid line).*

The integral of the β -function is the tune, see Eq. 2.20. For a certain optic it is calculated to be 3.555 in the horizontal plane and 3.626 in the vertical plane. The measured tunes for this optic yield 3.577, 3.605 in the horizontal and vertical plane, respectively.

Discrepancies between the calculations and measurements of the optical functions are present. To minimise these discrepancies, the description of the ideal machine has to be altered. For example, the magnetic field of an individual magnet is not identical to the ideal value. The magnets are not positioned at their ideal position, misalignments of the magnets occur. The magnets are positioned at a certain distance of each other. Hence interference of magnetic fields between two nearby magnets is possible and thus changes in the function of the element occur. These errors are investigated in the following chapter and used to improve the linear model.

Bibliography

- [1] E.D. Courant, H.S. Snyder, *Theory of the Alternating-Gradient Synchrotron*, Annals of Physics 3 (1958) p.1.
- [2] K. Steffen, *Proc. CERN Accelerator School on General Accelerator Physics Gif-sur-Yvette*, CERN 85-19 (1985) p.25.
- [3] E.D. Courant, R.D. Ruth and W.T. Weng, *Stability in Dynamical systems*, SLAC-PUB-3415 (1984).
- [4] R.D. Ruth, *Nonlinear Dynamics Aspects of Particle Accelerators*, Proc. Joint US-CERN School of Particle Accelerators, Sardinia 1985 Lecture Notes in Physics, vol. 247 (1986) p.37.
- [5] N.M. Gelfand, *Beta Measurements and Modeling The Tevatron*, FERMILAB-Conf-93/173 (1993).
- [6] A. Lehrach, L.H.A. Leunissen, H.J. Stein, R. Maier, *Tuning of the COSY telescopes*, Annual report 1996, p.228.
- [7] J. Bentsson, *Non-Linear Transverse Dynamics for Storage Rings with Applications to the Low-Energy Antiproton Ring (LEAR) at CERN*, CERN 88-05 (1988) p.3.

Chapter 3

Linear modeling of the accelerator

In the previous chapter the ideal accelerator COSY is introduced. In reality however, misalignments and non-ideal magnets are present. The effects of these distortions are studied in this chapter. First of all, the closed orbit distortion is investigated. Secondly, numerical calculations are done for magnetic field modeling to understand interference between magnets in the lattice. Finally, a fit-procedure for quadrupole strengths, corrector strengths and calibration factors for beam position monitors is presented.

3.1 Closed orbit description

For the calculation of the particle motion, an ideal system is assumed, i.e. a system with perfectly aligned dipoles and quadrupoles. In reality however, misalignments are present. In this section, the effect of misalignments of the bending magnets and the quadrupoles in the accelerator is studied. These misalignments have been measured and used for numerical calculations of the closed orbit distortion. Apart from alignment errors, magnetic field variations in the dipoles occur also, which are included in the calculations.

The transverse motion of the particles in a cyclic accelerator is a superposition of a motion along a closed trajectory (closed orbit) and betatron oscillations around this curve. In a real accelerator both the closed orbit and the betatron oscillations are distorted due to misalignments and errors in the magnetic fields, ground movements and stray fields. The maximal deviation of the distorted orbit from the ideal orbit (reference orbit) is limited by the vacuum chamber and reaches up to a few centimeters. For the compensation of the closed orbit either small correcting magnets and additional correction coils in the main dipole magnets are used. These

correcting systems reduce the closed orbit deviation to a sufficiently small value. For the description of particle motion through a magnetic field we make use of the Hamilton formalism. The relativistic Hamiltonian for a particle in curvilinear coordinates (s, x, z) is given by Eq. 2.14. We introduce the following perturbations in the Hamiltonian:

- magnetic field error in the dipole magnets: ΔB_z
- magnetic element misalignments: Δx and Δz
- dipole tilts around the longitudinal axis: θ

When linear perturbations are introduced into the Hamiltonian [1], we get $H = H_0 + \delta H^D + \delta H^Q$ with

$$\delta H^D = -e\Delta B_z x + h\theta z + (1+n)h^2 x \Delta x - nh^2 z \Delta z + (1+hx)\delta \quad (3.1)$$

for the dipole with n the field index given by $n = -(\rho/B_0)(\partial B_z/\partial x)$ and

$$\delta H^Q = k(x\Delta x - z\Delta z) \quad (3.2)$$

for the quadrupole. The linear part of δH describes the distance with respect to the unperturbed Hamiltonian. The quadratic part of the Hamiltonian H_0 describes the particle oscillations.

The new orbit is a periodical solution of the Hamilton equations. The particle motion is described as followed

$$\begin{aligned} x &= x_0 + \Delta x, \\ p &= p_0 + \Delta p_x. \end{aligned} \quad (3.3)$$

After performing a canonical transformation from the variables x_0, p_0 to x, p using as generating function:

$$F_2(x_0, p; s) = (p_0(s) + p(s)) x(s) - x_0(s) p(s). \quad (3.4)$$

a new Hamiltonian is derived from which one can deduce the equations of the transverse particle motion. Hill's equations with a non-zero right hand side:

$$\begin{aligned} \frac{\partial^2 x}{\partial s^2} + k_x(s)x &= F_x(s); \\ \frac{\partial^2 z}{\partial s^2} + k_z(s)z &= F_z(s). \end{aligned} \quad (3.5)$$

For the dipole we have $k_x(s) = (1-n)h^2$ and $k_z(s) = nh^2$. The non-zero right hand side for dipoles (F^D) and quadrupoles (F^Q) are given by:

$$\begin{aligned} F_x^D(s) &= -\frac{\Delta B_z}{B\rho} - (1+n)h^2 \Delta x; & F_z^D(s) &= nh^2 \Delta z - \theta h \\ F_x^Q(s) &= -k_x(s) \Delta x & F_z^Q(s) &= k_z(s) \Delta z. \end{aligned} \quad (3.6)$$

The particle oscillation are the homogeneous solution of Eq. 3.5 described by Courant-Snyder variables:

$$x(s) = a\sqrt{\beta_x(s)} \cos\left(Q_x \int_0^s \frac{ds}{Q_x\beta_x(s)}\right) \quad (3.7)$$

where Q_x is the number of the betatron oscillations per turn. After introducing new variables φ and η , respectively the generalised azimuth and the normalised deviation are:

$$\varphi = \int_0^s \frac{ds}{Q_x\beta_x(s)}; \eta = \frac{x}{\sqrt{\beta_x(s)}}. \quad (3.8)$$

In these new variables, the oscillation can be written as $\eta(\varphi) = a \cos(Q\varphi)$. Using the method of varying the integration constants the following particular solution can be obtained:

$$\eta = \frac{Q_x}{2 \sin \pi Q_x} \int_{\varphi}^{\varphi+2\pi} f(t) \cos(\varphi + \pi - t) dt \quad (3.9)$$

with $f(t) = \beta^{3/2}(\varphi)F(\varphi)$. A matrix approach for the treatment of the solution can be used for the calculation of the average transverse position of the closed orbit. The integral is transformed to a sum when the elements are short enough compared to the accelerator circumference (i.e. the length $\Delta\varphi_j = l_{\varphi,j} \ll 2\pi$). The distortion at a position $\eta(\varphi)$ is a result of all the errors at position j in the ring

$$\eta(\varphi) = \frac{Q_x}{2 \sin \pi Q_x} \sum_{j=1}^{M+L} \bar{f}_i(t) l_{\varphi,j} \cos Q_x(\varphi + \pi - \varphi_j) \quad (3.10)$$

where $\bar{f}_i l_{\varphi,j}$ are the generalised perturbations with the bar indicating averaging over the magnetic element, M is the total number of dipoles and L the number of quadrupoles. For the dipoles the quantities $\bar{f}_i l_{\varphi,j}$ have the following form:

$$\frac{Q_x \bar{\beta}_j^{3/2} l_{\varphi,j} \Delta B_j}{2B\rho \sin \pi Q_x} - \frac{Q_x \bar{\beta}_j^{3/2} n_j l_{\varphi,j} \Delta x_j}{2\rho^2 \sin \pi Q_x} \quad (3.11)$$

and for the quadrupoles:

$$\frac{Q_x \bar{\beta}_j^{3/2} g_j l_{\varphi,j} \Delta x_j}{2B\rho \sin \pi Q_x} \quad (3.12)$$

The misalignments and the magnetic field deviations are known. These values can be used to calculate the distorted closed orbit, see next subsection. The rms-values of the misalignments of the dipoles are: $\Delta s_{rms} = 0.085$ mm, $\Delta x_{rms} = 0.065$ mm. The rms-values of the misalignments of the quadrupoles are: $\Delta s_{rms} = 0.71$ mm, $\Delta x_{rms} = 0.23$ mm. When the following formula is used, the rms-value of the horizontal closed orbit can be calculated [2]:

$$x_{rms} = \frac{\sqrt{\bar{\beta}_x}}{2\sqrt{2} \sin \pi Q_x} \left[\frac{\Delta B^2}{B^2} \sum_i \beta_{x,i} + \Delta x^2 \sum_i k l^2 \beta_{x,i} \right]^{1/2} \quad (3.13)$$

In the case of COSY, a closed orbit deviation of about 25 mm is expected when $\Delta B/B = 2 \cdot 10^{-4}$.

3.1.1 Horizontal closed orbit

For the orientation in space one uses a bending magnet or a quadrupole, each having six degrees of freedom: three translations, in the horizontal, vertical and longitudinal plane and three rotations about the different axis. After the design and building of the cooler-synchrotron, the position of all the elements have been measured [3]. The measurements have been carried out as followed: each of the dipoles has three reference-points in which a tripod is placed to determine the position of the dipole. For the quadrupoles there is one difference, five reference points are known here. The accuracy of the measurements is 0.05 mm. The quadrupoles in the telescopes are placed in a straight line (with minimal transverse deviations) between the arcs and their longitudinal position is only known with an accuracy of 0.5 cm (which does not influence the optic, however). To determine the transverse misalignment, we need to know the distance between the reference positions of the magnets and the measured positions. These distances are known and it is now possible to determine the translations in the three independent directions (x, z, s) and the rotations about these axis. These calculations have been used to determine the distortion of the closed orbit with the numerical code MAD [4]. The result of this calculation is shown in figure 3.1. However, measurements show that the misalignments of the reference trajectory is larger (about 20 mm) then the calculations.

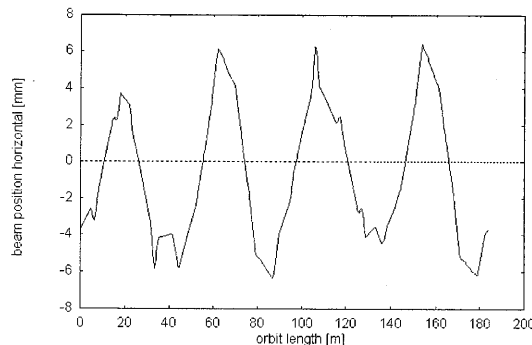


Figure 3.1: *Horizontal closed orbit displacement due to longitudinal, horizontal and vertical misalignments of dipoles and quadrupoles.*

Furthermore, the error in the power supply settings of the quadrupoles is $8 \cdot 10^{-4}$ and for the dipoles it is 10^{-4} at flat top, $4 \cdot 10^{-4}$ at flat bottom and $8 \cdot 10^{-4}$ during acceleration. When this is taken into account, the deviation of the particle trajectory from the reference trajectory is much larger. A power supply error of $8 \cdot 10^{-4}$ of all magnets is in agreement with measurements of the particle trajectory at flat top, see figure 3.2. These measurements were taken at two different days

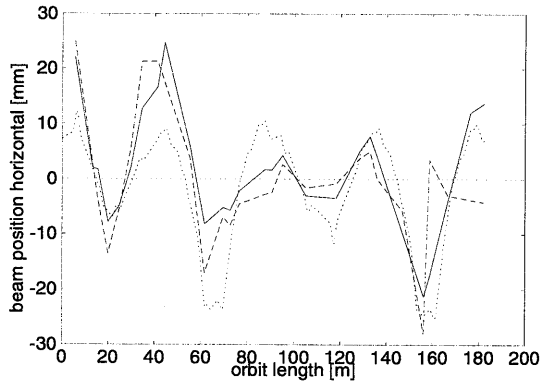


Figure 3.2: Calculation of closed orbit with misalignments of dipoles and quadrupoles and a power supply error of $8 \cdot 10^{-4}$, dotted line. The other lines indicate measurements of the closed orbit at flat top at an energy of 1250 MeV/c (solid line) and 2750 MeV/c (dashed line).

at two different momenta, namely 1250 MeV/c and 2750 MeV/c. As is shown, the closed orbit is reproducible.

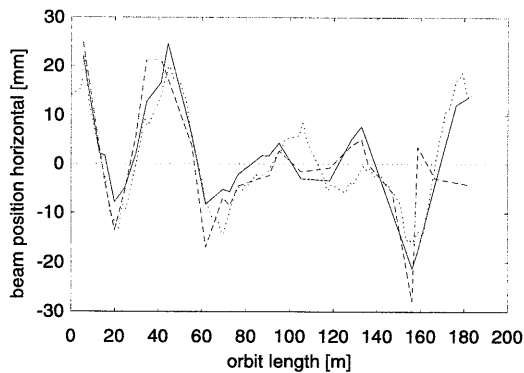


Figure 3.3: Calculation of closed orbit with misalignments of dipoles and quadrupoles, a power supply error of $4 \cdot 10^{-4}$ and individual field errors of the dipoles, dotted line. The other lines indicate measurements of the closed orbit at flat top at an energy of 1250 MeV/c (dashed line) and 2750 MeV/c (solid line).

The calculations are not in complete agreement with the measurements. This can be improved by using magnetic field errors from the individual dipoles with respect to each other. The values are measured at several currents, from which we will use the values of 200 A, which are close to the current used for the dipoles at injection energy. In the calculation shown in figure 3.3 we have used the misalignments of the dipoles and quadrupoles in the arcs, a power supply error for all quadrupoles of $8 \cdot 10^{-4}$. For the dipoles, a power supply error of $4 \cdot 10^{-4}$ is used and the magnetic field errors for all the dipoles are included.

These measurements were taken at two different days at two different momenta, namely 1250 MeV/c and 2750 MeV/c. As shown, the calculations are in better agreement with the measurements.

Another point of study is the development of the closed orbit as function of energy. The error in the power supply setting is time-dependent which yields a problem for closed orbit control during acceleration. In the calculations the power supply error is varied from $-8 \cdot 10^{-4}$ to $4 \cdot 10^{-4}$. The beam is accelerated from 269.4 MeV/c to 1150 MeV/c in a period of approximately 1100 ms. The numerical calculations and the measurements of the closed orbit during acceleration are shown in figure 3.4 and in figure 3.5, respectively. They develop both in the same manner if the general behavior of the shapes is investigated.

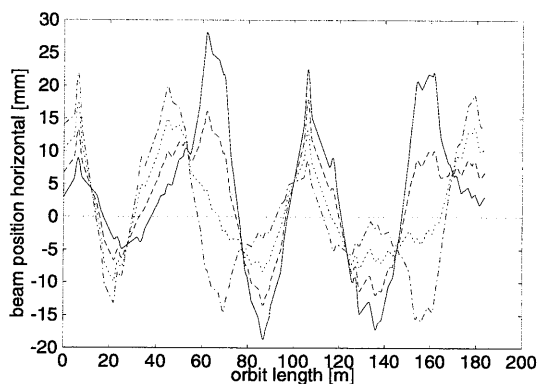


Figure 3.4: Calculation of closed orbit with power supply errors varied during acceleration. A power supply error of $-8 \cdot 10^{-4}$, indicated with a solid line. $-4 \cdot 10^{-4}$, dashed line, $0 \cdot 10^{-4}$ dotted line and $4 \cdot 10^{-4}$ indicated with a dash-dot line.

Comparing with a real power supply error measurement shows that the size of the error is of the same magnitude.

The calculated closed orbit is sufficiently described, the compensation of the deviations is the next goal. Several schemes have been proposed for this purpose. The closed orbit can be influenced by adjusting the independent sources. First of all, the misalignments of the dipoles and quadrupoles can be minimised. Secondly, the field errors of the independent dipoles can be altered by using correction coils that are mounted on the dipoles. These correction coils can also be used to minimise the effect of the misalignments.

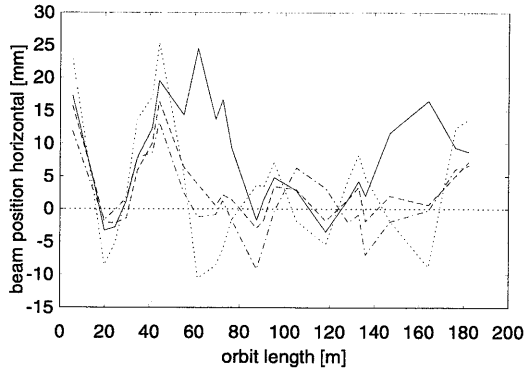


Figure 3.5: *Measurement of closed orbit during acceleration. The momenta at which the orbits are measured are indicated as followed. 393.7 MeV/c with a solid line. 681.5 MeV/c, dashed line, 969.3 MeV/c, dotted line and 1049.9 MeV/c indicated with a dash-dot line.*

Calculations have shown that the improvement of the position of the individual elements in the ring only change the maximal displacement of the closed orbit by approximately 4 mm. More can be achieved when the individual field errors of the dipoles or the power supply error are minimised. For this purpose small correction coils in the dipole magnets, back-leg windings (BLW), can be used. BLW8 (of dipole 8, numbering starts in the arc containing the fast quadrupoles) is connected to a power supply unit and can be used for measurements. The BLW can change the main magnetic field by a few percent, depending on the current through the dipole, see figure 3.6. For example, the main magnetic field can be changed by approximately 0.03 T at 1000 A and 0.008 T at 5000 A.

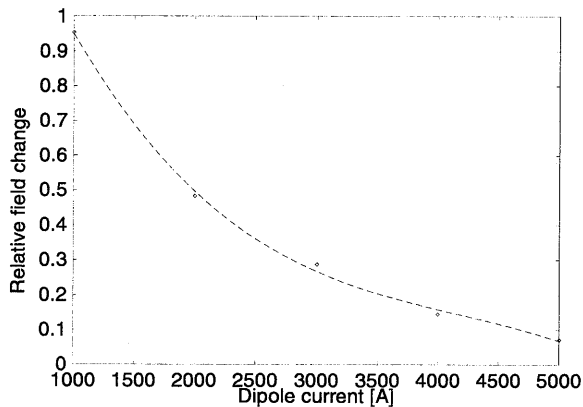


Figure 3.6: *Relative field change in main dipole field by BLW in pro mille. The current of the back-leg winding is 1 A.*

The dots are used to extrapolate the relative field change at flat bottom (285 A for 269 MeV/c), which is about $1.47 \cdot 10^{-4}$ when the current through the BLW is 1 A. The closed orbit is measured at flat bottom and the power supply error is determined to be $-16 \cdot 10^{-4}$. The BLW is given currents of -3 A and +3 A. In both cases a closed orbit is measured. The calculations show that a relative field error in BLW8 of $\pm 50 \cdot 10^{-4}$ is in agreement with the measured closed orbit, see figure 3.7. In this figure the reference orbit is not shown, only the orbits that are shifted because of BLW8.

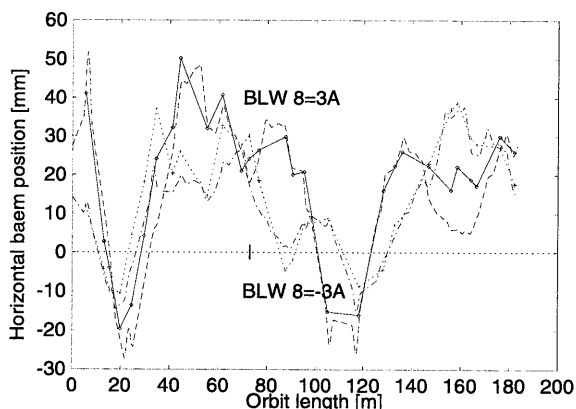


Figure 3.7: *BLW 8 excited to 3A (solid line) and -3 A (dotted line). Corresponding calculations with MAD for +2.5 A (dashed line) and -2.5 A (dash-dotted line).*

The current that corresponds to the field error is 2.5 A, which is close to the setting of the power supply unit which was 3 A. The same measurements are done at flat top. Measurements done with BLW 22 yield comparable results.

3.1.2 Vertical closed orbit

The position of all elements were measured in the vertical direction. The measurements are done as followed. On each of the dipoles, quadrupoles and sextupoles a chassis is placed to determine the vertical position on each corner of the dipole, and to determine the vertical position of the five reference points of the quadrupoles. For the sextupoles only two positions are known along the axis and the perpendicular rotation is corrected to less than 0.1 mrad. From these positions it is possible to determine the translation in z-direction and to calculate the rotation-angle about the x- and z-axis. The translation in the vertical plane was about 0.1 mm, the angles were smaller then 0.7 mrad. The vertical closed orbit calculated from the misalignments is shown in figure 3.8.

A calculated closed orbit distortion of about 1 mm is observed, which is smaller than the measured closed orbit which has an amplitude of about 3 mm, as shown in figure 3.8. The closed orbit deviations are small in comparison with the horizontal closed orbit and as such difficult to determine. In this measurement steerer magnets

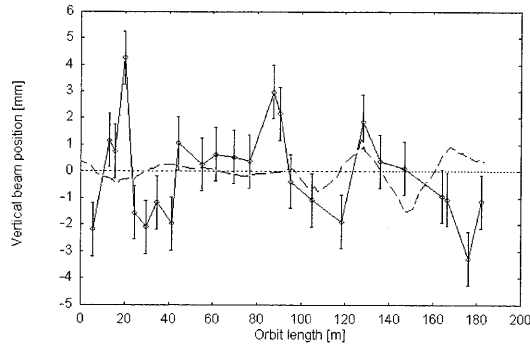


Figure 3.8: *Calculated vertical closed orbit displacement due to misalignments of dipoles and quadrupoles (dashed line). Measured vertical closed orbit (solid line) and indicated errorbars.*

were used to determine the vertical closed orbit. The experimental setup is as follows: the vertical closed orbit is measured at flat top with a steerer with a certain current. The closed orbit distortion is in the order of 10 mm (easy to measure) and the same measurement is done with the same current, only with the opposite sign. The averaged values of these measurements describe the vertical closed orbit. These measurements were done for several vertical steerer magnets and the gained vertical closed orbits are averaged to determine the vertical orbit. The errorbars indicate the inaccuracy in the determination of the vertical orbit. In this figure measurements are shown of the closed orbit for a specific energy at flat top (800 MeV/c). As a remark, during acceleration the maximal vertical closed orbit deviation changes approximately 1 mm.

3.2 Calculation of the effective quadrupole gradient

The magnetic field inside a perfect quadrupole is constant along the longitudinal axis at a certain transverse position. Outside of this quadrupole, the magnetic field should drop to zero instantly. However, a real magnet has some field outside the iron. The ends of the magnets in the lattice of an accelerator constitute only a small fraction of the integrated field. The circulating beam is not much influenced by the small curvature of the central trajectory through the fringing fields. However, when the length of the magnet is comparable to the aperture much of the magnet's effect comes from the fringing fields in which the particle is deflected. In a small ring where many magnets are placed close to each other the influence of nearby magnets can not be neglected without consideration.

In the COSY-ring the aperture of the quadrupoles is 170 mm. The length of the quadrupoles in the telescopes is 570 mm and in the arcs 300 mm. The distance between the quadrupoles in the telescopes is 290 mm between the middle quadrupoles

and 430 between the outer quadrupoles. At several positions a sextupole (iron length 200 mm) is placed between the outer quadrupoles. At a distance of 125 mm at the end of the quadrupole quadruplet a steerer magnet is placed. In the arcs similar problems occur. Near the quadrupoles dipoles are positioned at 508 mm. Occasionally a sextupole (iron length 110 mm) or a steerer magnet (iron length 132 mm) is placed between a dipole and a quadrupole. For a more detailed overview see the appendix and figure 1.1. To estimate the influence of the fringing fields calculations [5] and magnetic field measurements [6] were carried out.

To estimate the magnetostatic influence of individual magnets with respect to each other several calculations have been made with the program MAFIA [7]. This code solves the Maxwell equations for the electromagnetic field. The following calculations were done for the magnetostatic case in which two magnets (dipole and quadrupole, quadrupole and steerer) are placed near each other and the influence is determined. In the following subsections three examples are presented in which the influence of a nearby element is calculated. In the first example a comparison with an experimental setup is given (quadrupole with nearby steerer magnet). In the second example a description of a dipole magnet is given and the influence of a nearby steerer magnet is calculated. In the third example the mutual influence between a dipole magnet and a quadrupole is examined.

3.2.1 Telescope quadrupole and steerer

The influence of a steerer magnet on the fringing field of a quadrupole in the straight section is examined. The geometry of the iron of both the quadrupole (MQT) and H-type steerer are inserted and the coils for the quadrupoles are defined. The magnets are placed at a distance of 120 mm from each other. Measurements were carried out in an experimental test situation. To verify the experimental results a distance of 120 mm was taken in the calculations (120 mm is not in agreement with the positioning in the ring). We calculate the magnetic field of the quadrupole at, for example 20 A. The magnetic field is dependent on the transverse position of the particle. Therefore, the magnetic field is calculated in a straight line with a horizontal displacement of 60 mm and no vertical displacement. First without and then with the steerer iron, the two calculated curves are subtracted from each other to determine the change in the magnetic field. The resulting curve is shown in figure 3.9. The difference in effective length of the quadrupole is changed by about 1.5% because now the field drops faster to zero. The left side of the quadrupole is at the origin of the plot (end of quadrupole at 570 mm), the steerer iron is positioned at 690 mm from the origin.

A similar experimental test set-up was made and the measurements [6] show similar results. The two measured curves were subtracted from each other and the resulting curve is plotted in figure 3.10. The magnetic field inside the quadrupole is 0.018 T.

When comparing figure 3.9 with figure 3.10 the agreement between calculation and measurement is shown.

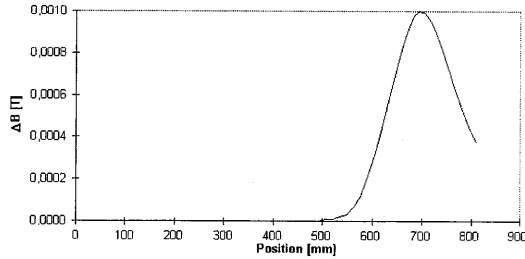


Figure 3.9: *Difference between MAFIA calculation of quadrupole (at 20 A) with and without steerer iron at 120 mm distance.*

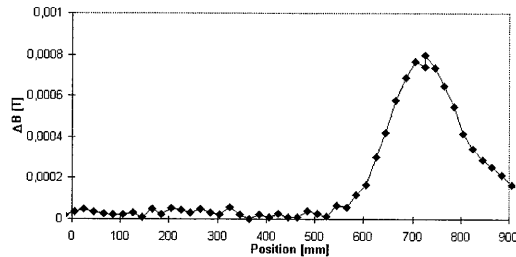


Figure 3.10: *Difference between measurement of quadrupole (at 20 A) with and without steerer iron at 120 mm distance.*

3.2.2 Dipole with C- or H-steerer

For the following calculations a dipole magnet (iron length 1.755 m) is simulated with MAFIA. The numerical results have been compared with Hall-probe measurements [8]. The measured magnetic field is indicated with a dashed line and the MAFIA calculation with a solid line in figure 3.11. The origin of the plot is situated in the centre of the dipole. The absolute value of the magnetic induction at the centre of the dipole in the calculations is different with respect to the measurement by about 0.3 % at 1 T. At other currents the agreement with the measured magnetic induction is < 0.8%. The fringing fields of the dipole are described accurately. The only difference is the value of the effective length of the dipole. Because the magnets are laminated, small gaps between the iron layers change the magnetic length.

To resolve the influence of the steerer magnets on the fringing field of the dipoles several calculations were done. First of all, the situation of a COSY dipole with a H-type steerer at a distance (iron to iron) of 216 mm was reproduced (BE11 and SH19). Due to the presence of the steerer iron the magnetic field of the dipole is changed. The calculated effective length of the dipole is shortened by 0.34 %. Similar calculations were done for a dipole (BE24) with a C-type steerer (SH41) at a distance of 222 mm. The effective length of the dipole is 0.26 % smaller. Because the steerer magnet is not parallel to the dipole (curved trajectory), the distance between both magnets is not constant. When a particle travels 25 mm off axis the

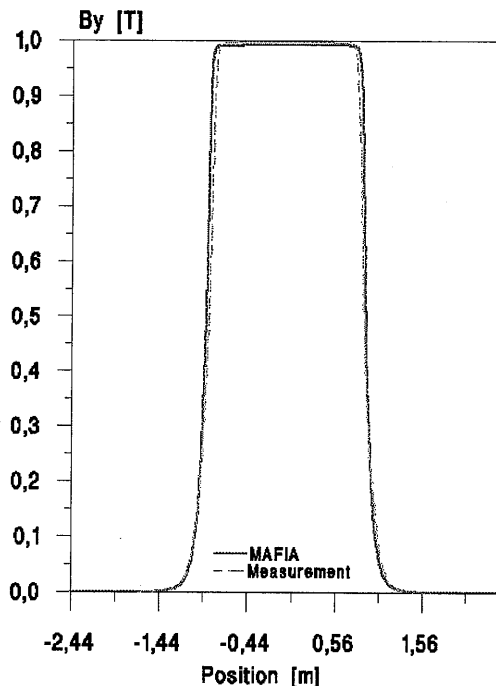


Figure 3.11: Magnetic field at 2244 A of a COSY dipole. The solid line indicates the measured vertical induction and the dashed line indicates a MAFIA approximation.

additional effective length of the dipole it sees is 0.01 % larger when the distance increases or 0.01 % smaller when the distance decreases.

3.2.3 Dipole with quadrupole

The calculation of the typical situation with a dipole and a quadrupole (MQU) at a distance of 508.5 mm are performed. Calculations have been done for several cases in which the currents in the individual magnets were changed. The distance between a dipole and a quadrupole is so large that the influence of the quadrupole on the dipole is negligible. The magnetic field in the quadrupole is dependent on the presence of the magnetic field in the dipole. The magnetic field in the quadrupole becomes smaller after increasing the current in the dipole. In figure 3.12, the situation is plotted in which the dipole has a current of 2244 A and the quadrupole is excited at 200 A. The magnetic field at 100 mm off axis (in the horizontal plane) is plotted to clearly show the magnetic field inside the quadrupole.

The origin is positioned in the centre of the dipole and the solid line indicates a calculation where both the dipole and the quadrupole are present. When the magnetic field inside the quadrupole is calculated without the presence of the dipole it is 1.8 % higher. Calculations show that the magnetic field inside the quadrupole

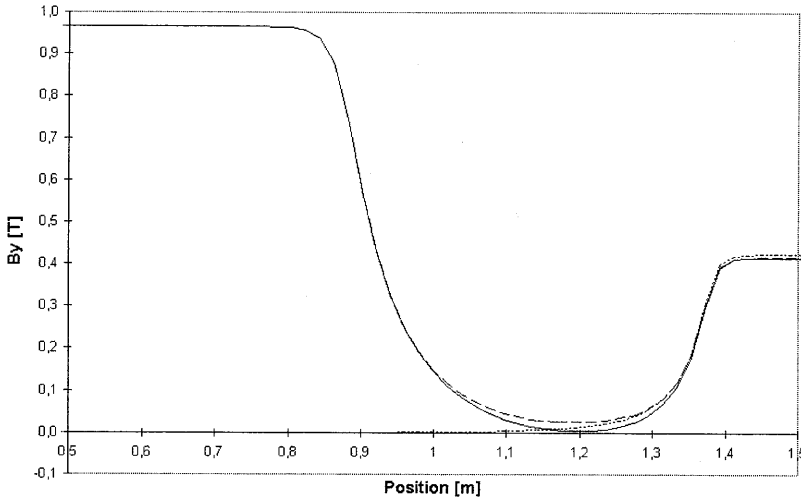


Figure 3.12: *MAFIA* calculation of magnetic field between dipole magnet (2244A) and quadrupole magnet (200A). The solid line indicates the magnetic field where both magnets are present, the dotted line indicates calculation where the dipole magnet is not present (dashed line: only dipole magnet).

does not change anymore with higher dipole fields. If the dipole current is changed to 1122 A (50%) the effect in the quadrupole is 20 times smaller.

The influence of a steerer magnet between the quadrupole and dipole is examined. The steerer magnet continues to function as field clamp for both magnets. However, the magnetic field in the quadrupole is still influenced by the magnetic field of the dipole.

3.3 Modeling

To understand the particle accelerator, an accurate model is required. This model should be at least accurate in first-order. For the COSY accelerator ring, a procedure has been developed in which a consistent computer model is obtained based on a set of difference orbit measurements. From the difference orbit measurements, the response matrix coefficients M_{ij} are determined which are defined by

$$M_{ij} = \frac{\Delta x_i}{\Delta x'_j}. \quad (3.14)$$

The matrix elements are the orbit deviation x_i at BPM i divided by the kick angle of a steering magnet j . Using a numerical code, for example MAD, the response matrix coefficients C_{ij} are calculated. The corrector scale factors can be determined by solving the linear equation

$$M = C \cdot s \quad (3.15)$$

in which s is a diagonal matrix containing the steerer calibration factors for each steerer. However, when using a first-order perturbation approach, errors in our model can be found by adjusting the following parameters.

1. Quadrupole gradients
2. Steerer scaling factors
3. BPM scaling factors
4. BPM resolution errors

For the computer model the response matrix coefficients are calculated and their derivatives with respect to the gradient of a particular quadrupole. These $\partial C_{ij}/\partial k_q$ are easily calculated by a numerical code such as MAD. The following equations have to be solved

$$M_{ij} = p_i C_{ij} s_j - \sum_q \frac{\partial C_{ij}}{\partial k_q} \delta k_q. \quad (3.16)$$

Here, p_i is the scaling factor for the beam position monitor which is unity for the moment, s_i are the individual steerer scale factors and ∂k_q are the quadrupole gradient errors which all are fitted in order to minimise the difference between the measured and the calculated matrices. When the fitting parameters are known, the same fit-function can be used to calibrate the individual BPM scaling factors p_i with Eq. 3.16 in which the scaling factors s_j are kept constant. After this fit, Eq.3.16 is used again. However, this time the BPM scaling factors are included in the fit-function as constants and again the individual steerer scale factors and the quadrupole gradient errors are fitted. After these calculations are done, the difference between the calculated and measured difference orbits are smaller than the measurement inaccuracy which is about 0.2 mm.

The fitting procedure has one restriction: it is not possible to determine the fitting parameter for each individual quadrupole because of degeneracy of the quadrupole families. Since the magnetic field of the individual quadrupoles at each currents is known, each individual quadrupole gradient error is known. We introduce 9 parameters that are used to determine any quadrupole errors. This is coherent with the position of each quadrupole in the accelerator ring. Some quadrupoles have other magnets in their vicinity, like a steerer magnet, a sextupole magnet, none or both (see past section). To show the influence of other magnets near the quadrupoles following calculations and measurements in the next paragraph are done. Due to this fact, four parameters are introduced which are determined through the position of the element in the ring. Since two kinds of quadrupoles (small ones in the arcs and large ones in the telescopes) are present in the ring 8 parameters are needed in total. One extra parameter is introduced to determine the change in the effective magnetic length (read change in the gradient) which is equal for each quadrupole in the ring. This parameter is introduced to account for the presence of the vacuum chamber and because of a possible systematical error during the measuring of the quadrupoles. However, the difference response matrix is calculated and for each

quadrupole its corresponding matrix is also calculated. It takes about 3 hours of computer time to calculate all required matrices.

3.4 Measurements

At several energies the difference orbits are measured with each individual steerer which is excited at a certain current so that the amplitude of the closed orbit was large, but small enough to ensure that no particles are lost. The same measurement is carried out with the same current with the opposite sign. From both measurements the change in the position is calculated with respect to the current flowing in the steerer magnet. From each steerer the elements of the matrix M_{ij} are measured. This measurement has to be repeated for each steerer and thus complete the matrix M_{ij} . Several measurements have been done to obtain the calibration factors.

3.4.1 Steerer measurements at 295 MeV/c

At the energy of 295 MeV/c two measurements were done. They yield both similar results and the data from one measurement are shown in figure 3.13. Here the steerer calibration factors are shown for all horizontal steerers. The calibration values have negative signs because of a sign convention between the numerical program MAD and the steerers that are used in the ring. The steerers SH29-SH37 are used for extraction. Therefore they are altered to give larger kicks to the orbit. These results are in agreement with other measurements done at the same energy.

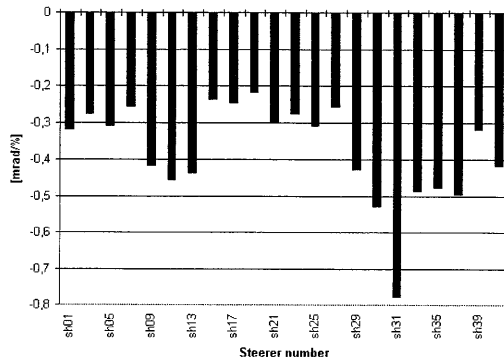


Figure 3.13: Steerer calibration factors at 295 MeV/c for the horizontal plane.

The BPM calibration factors are extracted from the same measurements. For the ideal BPM they should be 1, however, the deviations are at the most 20% from this value. The BPM scaling factors are shown in fig. 3.14. A second measurement done at this energy showed the same response for the BPM scaling factors. The difference between both of the measurements was an overall amplitude factor of

about 10%. During these measurements BPM 3 was not operating, its scaling factor was correctly predicted to be zero in the fitting procedure.

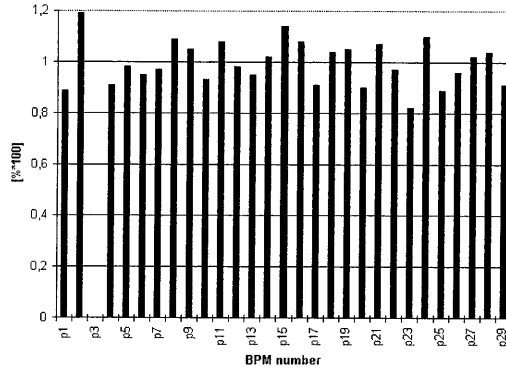


Figure 3.14: *BPM calibration factors at 295 MeV/c in the horizontal plane.*

3.4.2 Comparison with other energies

Until the end of 1996 five complete horizontal response matrices are measured (combined measurement of the horizontal and vertical response matrix are time-consuming and can not be completed in the timespan available for the measurements). At the following momenta: 295 MeV/c, 825 MeV/c, 1200 MeV/c, 1673 MeV/c and 2500 MeV/c. the steerer calibration factors, BPM scaling factors and the quadrupole errors were determined from the measured response matrix. The BPM scaling factors and the steerer calibration factors are easy to determine. The quadrupole errors are more difficult to resolve because of the small changes they make on the closed orbit. For example: the steerer magnets gives changes to the closed orbit with amplitudes of a few millimetres whereas the quadrupole errors only change it less then a millimetre. The inaccuracy with which the closed orbit is measured (approximately 0.2 mm) gives large errors on the changes of the quadrupole gradients.

The steerer calibrations as function of the momentum are shown in figure 3.15 and 3.16 for some steerer in the telescope section and in the arcs, respectively. The steerer factors are scaled with their corresponding $B\rho$ value which should yield a momentum independent calibration factor for each individual steerer magnet.

The steerers in the telescope sections show roughly a momentum independent calibration factor. However, in the arcs the steerers give smaller kicks at higher momenta. Calculations with the code MAFIA show that the fringing field of the steerer magnet is very large. Due to the dipole and quadrupole magnets along the steerer magnet the effective length of the corrector is changed at higher currents. For example: at 30% of the steerer magnets maximal current the effective length is 4.3% smaller then at lower currents. At 60% the effective length is 8.6% shortened.

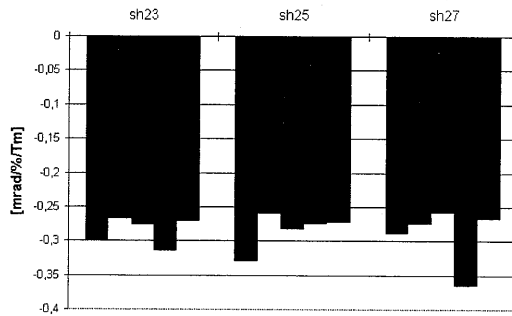


Figure 3.15: Steerer calibration factors scaled with $B\rho$ as function of momentum (295, 825, 1200, 1673 and 2500 MeV/c). All three steerer magnets are positioned in the cooler telescope.

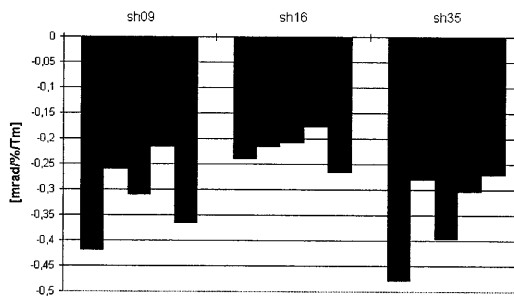


Figure 3.16: Steerer calibration factors scaled with $B\rho$ as function of momentum (295, 825, 1200, 1673 and 2500 MeV/c). All three steerer magnets are positioned in one of the arcs of the accelerator.

In the telescope sections this effect is much smaller. To measure difference orbits at higher currents it is necessary to increase the current on the respective steerer and thus showing the decrease of the steerer response. The optic is not the same for all measurements the current at which the steerer is driven is not increased linearly for higher energies. Therefore the plots show some peaks that are higher than expected.

The quadrupole errors for the measured energies (825 MeV/c, 1200 MeV/c, 1455 MeV/c, 1673 MeV/c, 2500 MeV/c, 3000 MeV/c, 3400 MeV/c) are plotted in figure 3.17. The quadrupole errors are classified in eight groups, namely: (k) single MQT, (ks) MQT with sextupole beside it, (kst) MQT with steerer magnet beside it, (kss) with MQT positioned between a steerer and a sextupole magnet, (u) single MQU, (us) MQU with sextupole beside it, (ust) MQU with steerer magnet beside it and (uss) with MQU between a steerer and a sextupole magnet. Values smaller than 0.4 % are expected for the u's values (MAFIA calculations). For the k's values smaller than 0.2 % are expected. An energy dependence of the quadrupole errors is not

noticed, merely a fingerprint that is dependent of the specific machine settings.

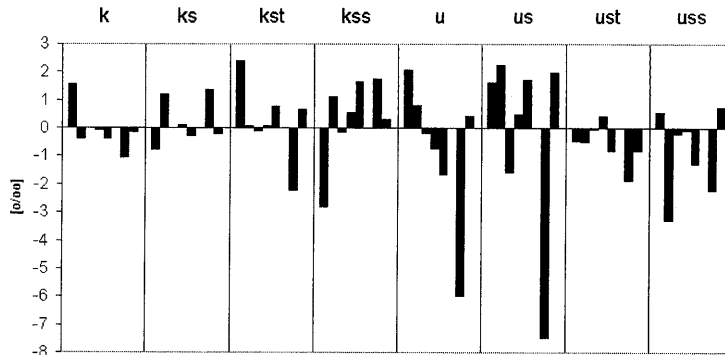


Figure 3.17: *Quadrupole gradient errors as function of momentum (825, 1200, 1455, 1673, 2500 (2 \times), 3000 and 3400 MeV/c). The quadrupole errors are indexed in 8 groups, see text.*

The quadrupole errors can be used for the adjustment of the linear model of the accelerator. The horizontal and vertical betatron tune are not included in the fit-procedure. However, the discrepancy for the prediction of the betatron tunes between the model and the measurement is minimal after the quadrupole errors are included in the model. The numerical model predict a tune of 3.6170 in the horizontal plane and 3.6213 in the vertical plane before correction. After correction the calculated tunes were 3.6334 and 3.6282, respectively horizontally and vertically. The measured tunes in this case were 3.633 ± 0.001 in the horizontal plane and 3.618 ± 0.001 in the vertical plane.

The suggested calibration method for the COSY accelerator as presented in the preceding section is used to determine several fitting parameters. The steerer calibration factors as well as the BPM electronic scaling factors are determined. The energy dependence of the steerer magnets is measured and understood. The quadrupole errors are small and difficult to obtain from the measured response matrix. The size of the errors is in agreement with MAFIA calculations as presented in section 3.2.

3.5 Orbit correction

In the last section the machine characteristics are learned by studying and analysing the orbit response to "kicks". The better the model of the machine is known, the better predictions on the behavior of the machine (inverse modeling) can be made and the more accurate we can control the accelerator. For orbit correction there are four general methods used.

1. Harmonic

In the harmonic method (e.g. [9]), the harmonic content of the orbits are determined and selected harmonics are corrected. The corrector strengths are calculated, assuming the harmonic composition of the dipole field errors reflect that of the orbit. This method yields good results when the position of the correctors and BPM's are close to being $\pi/2$ phase apart.

2. Least-square

A set of linear equations is solved in which the kicks that correct the orbit are calculated. The following equation is solved:

$$\vec{X} = M\vec{\theta}, \quad (3.17)$$

where the components of \vec{X} are the measured orbit deviations at the N_m monitors, the components of $\vec{\theta}$ are the kicks from the N_c correctors and M is the $N_m \times N_c$ response matrix. In the least-square method the residual rms-orbit (\vec{r}) around the machine is minimised

$$|\vec{r}| = |\vec{X} + M\vec{\theta}|. \quad (3.18)$$

Good results are obtained with this method. A small number of dipole errors in the ring are determined and compensated. An example of this method is Micado [10]. It decomposes the response matrix into an $N_m \times N_m$ upper diagonal matrix

$$H_n \dots H_1 M = \begin{pmatrix} U_0 \\ 0 \end{pmatrix} = U \quad (3.19)$$

where $H_1 \dots H_n$ are Housholder transformation matrices. When asked to use N correctors out of the available total of N_c , the algorithm is choosing the "most effective" N correctors. This method does not point to the actual error in the machine. Also, when the number of correctors is increased, the correctors start to "fight" each other, resulting in very large kicks.

3. Regularisation

The "fighting" of the correctors is caused by the ill-posedness of eq. 3.17. When M is singular or almost singular it leads to large θ 's for small X 's. In the Tikhonov regulation method [11] the equation

$$|\vec{X} + M\vec{\theta}|^2 + \alpha|\vec{X}|^2 \quad (3.20)$$

with α a positive stabiliser is minimised. This results in the following equation for the matrix:

$$(M^T M + \alpha I)\vec{\theta} = M^T \vec{X}. \quad (3.21)$$

Here, I is the unit matrix and M^T is the transposed response matrix M . The method is sensitive to the choice of α , which depends on the magnitude of the M_{ij} elements.

4. Singular value decomposition (SVD)

Using the technique of SVD [12], the response matrix is written as

$$M = UWV^T \quad (3.22)$$

where U and V are unitary matrices and W is an $N_m \times N_c$ diagonal matrix with non-negative elements. This transformation reconfigures the correctors and BPM such that each transformed monitor is coupled to one transformed corrector with coupling strengths W .

In the COSY accelerator the Micado algorithm and the SVD method are used for orbit correction. The vertical closed orbit is small, therefore an orbit correction is not necessary. Orbit correction for the horizontal plane is done for the whole energy range. When the mismatch between the RF-frequency and the dipole current is minimised, a typical horizontal closed orbit with deviations from the ideal orbit of about 10 mm can be corrected. The mismatch results in a closed orbit with a dispersive part that increases linearly as function of this mismatch. The result of orbit corrections yields to a closed orbit with rms-values of < 2 mm. An example of a closed orbit that has to be corrected is presented in figure 3.18 (momentum 1673 MeV/c).

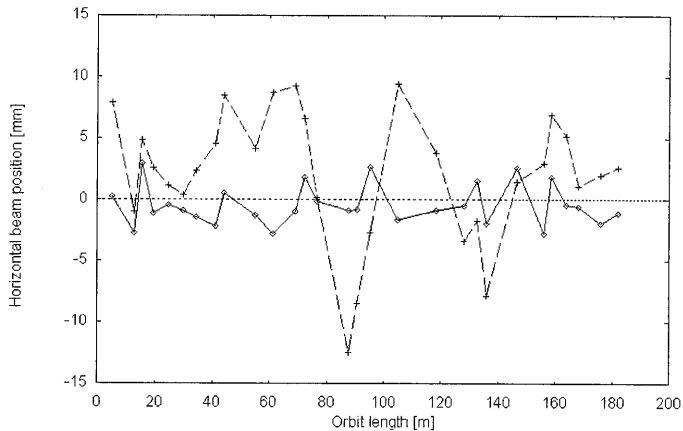


Figure 3.18: *Horizontal orbit correction with combined micado and SVD method. The dashed line indicates the closed orbit before correction, the solid line after correction.*

The correction is calculated with a maximum of four steerer magnets (chosen by algorithm at each correction). After the first correction the process is repeated. The correction after 3 iterations yields a rms-value for the closed orbit deviation of 2.5 mm. The final corrections are done with the SVD-method in which all correctors are used for correction. The result is an closed orbit with a rms-value of 1.5 mm.

3.6 Orbit bumps

Local bumps (without affecting the orbit outside the correctors) with a specified beam displacement and/or angle at a specified location can be created using three correctors [13] or four correctors [14]. For example, these bumps can be used to move the closed orbit near the extraction septum. In this case an orbit deviation is needed at an adjustable position x_p with fixed angle x'_p at point p . Four steerer magnets are needed in this case. Starting with 2 steerers with strength ε_1 and ε_2 that are positioned before p , the position vector is given by

$$\begin{pmatrix} x_p \\ x'_p \end{pmatrix} = M_1 \begin{pmatrix} 0 \\ \varepsilon_1 \end{pmatrix} + M_2 \begin{pmatrix} 0 \\ \varepsilon_2 \end{pmatrix} = \begin{pmatrix} a_{11} & a_{12} \\ a_{21} & a_{22} \end{pmatrix} \begin{pmatrix} 0 \\ \varepsilon_1 \end{pmatrix} + \begin{pmatrix} b_{11} & b_{12} \\ b_{21} & b_{22} \end{pmatrix} \begin{pmatrix} 0 \\ \varepsilon_2 \end{pmatrix} \quad (3.23)$$

with M_1 and M_2 the transfer matrices from the corrector magnet to point p . These equations can be solved with the following solutions for the corrector strengths

$$\begin{aligned} \varepsilon_1 &= \frac{b_{22}x_p - b_{12}x'_p}{a_{12}b_{22} - a_{22}b_{12}} \\ \varepsilon_2 &= \frac{a_{12}x_p - a_{22}x'_p}{a_{12}b_{22} - a_{22}b_{12}} \end{aligned} \quad (3.24)$$

The four bump has to be completed with two steerer magnets after point p to ensure that the closed orbit deviation and angle are the same as before the orbit bump was inserted.

After substituting the matrix elements with the optical Twiss parameters the following solutions for the corrector strengths are found

$$\varepsilon_1 = \frac{1}{\sqrt{\beta_1\beta_p}} \frac{\cos(\Psi_p - \Psi_2) - \alpha_p \sin(\Psi_p - \Psi_2)}{\sin(\Psi_2 - \Psi_1)} x_p - \sqrt{\frac{\beta_p}{\beta_1}} \frac{\sin(\Psi_p - \Psi_2)}{\sin(\Psi_2 - \Psi_1)} x'_p \quad (3.25)$$

and

$$\varepsilon_2 = -\frac{1}{\sqrt{\beta_2\beta_p}} \frac{\cos(\Psi_p - \Psi_1) - \alpha_p \sin(\Psi_p - \Psi_1)}{\sin(\Psi_2 - \Psi_1)} x_p - \sqrt{\frac{\beta_p}{\beta_2}} \frac{\sin(\Psi_p - \Psi_1)}{\sin(\Psi_2 - \Psi_1)} x'_p. \quad (3.26)$$

A horizontal corrector changes the closed orbit in the dipole magnets. The path length changes about $\Delta l_j = D_j \theta_j$. Here, D_j is the dispersion at corrector j and θ_j is the corrector kick. In the presence of RF the beam's momentum is changed by an amount of

$$\frac{\Delta p}{p} = -\frac{D_j \theta_j}{\left(\alpha - \frac{1}{\gamma^2}\right)C} \quad (3.27)$$

to leave the revolution frequency unchanged. Here, C is the circumference of the accelerator. The energy change will be visible at BPM i as additional orbit shift:

$$\Delta x_i = -\frac{D_i D_j}{\left(\alpha - \frac{1}{\gamma^2}\right)C} \theta_j. \quad (3.28)$$

To check this result, two measurements are done. First of all, an orbit bump is made in the target telescope. The steerer magnets: SH01, SH03, SH07 and SH09 are used to give a 20 mm bump at the position of BPM07. The resulting curve is shown in figure 3.19.

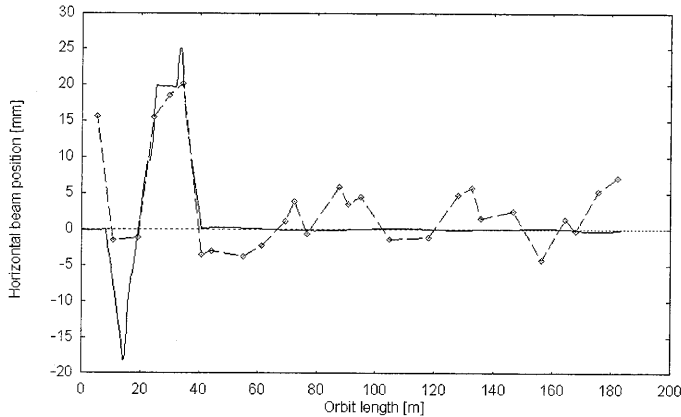


Figure 3.19: Calculated horizontal 20 mm orbit bump with SH01, SH03, SH07 and SH09. The angle at BPM07H is set to 0 mrad. The solid line indicates the MAD calculation, dashed line with dots indicates the measured closed orbit.

The calculated closed orbit without dispersion correction (see Eq. 3.28) is also shown in figure 3.19. The calculated correction in this case yields a Δx_i of 0.03 mm at each BPM. We see small deviations of about 5 mm from zero in the measurement. These are present when the steerer magnets have small deviations from their ideal setting ($< 5\%$).

In the second measurement the steerer magnets SH29, SH31, SH35 and SH37 are applied to achieve a 20 mm bump with a zero degree angle at the electrostatic septum. A dispersion correction is larger in this case and shown in figure 3.20. The dispersive term is not implemented in the numerical code MAD and represents the ideal bump which is indicated with a solid line. The dashed line indicates the calculation with dispersion correction that was evaluated numerically after the dispersion and the orbit bump were calculated with MAD. The corresponding measurement is shown with a dotted line.

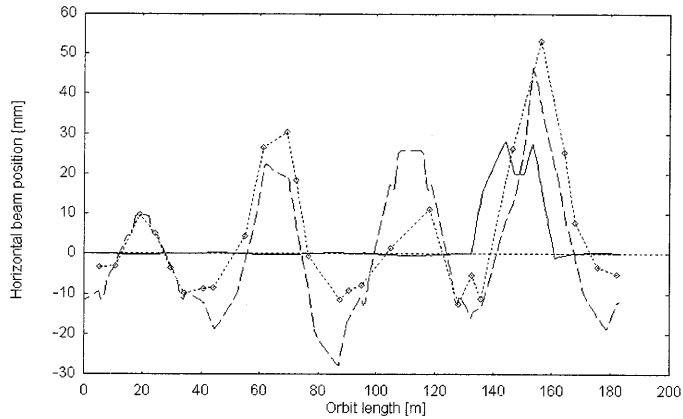


Figure 3.20: Calculated horizontal 20 mm orbit bump with SH29, SH31, SH35 and SH37. The angle at electrostatic septum is set to 0 mrad. The solid line indicates the MAD calculation, dashed line indicates MAD calculation with dispersion correction and dotted line indicates the measured closed orbit.

The measured dispersive part of the closed orbit differs at some places from the calculations. However, it gives a clear indication for the disagreement of the MAD calculation with the measurement. Normally this dispersive part in the closed orbit bump is compensated by adjusting the magnetic field or the RF-frequency to correspond to the energy change to diminish the deviations drastically.

Bibliography

- [1] D. Dinev, *Simulation and Correction of the Closed Orbit in the Cooler Synchrotron COSY*, KFA Internal Report, Jül-2406, 1991.
- [2] R. Maier, *Strahloptische Gesichtspunkte bei der Auslegung hochbrillanter Speicherringe*, Berichte des Forschungszentrum Jülich Jül-3120.
- [3] U. Bechstedt, W. Ermer, A. Hardt, G. Krol, J. Rook, D. Rosin, Th. Sagefka, *Geodetical Concept and Alignment of COSY*, Institut für Kernphysik Annual Report 1992, p.191.
- [4] H. Grote, F. Ch. Iselin, *The MAD Program (Methodical Accelerator Design) Version 8.1, User's Reference Manual*, CERN/SL/90-13 (AP) (revision 1)
- [5] V. Nelyubin, H.J. Stein internal communication
- [6] Th. Sagefka, internal communication
- [7] MAFIA, the MAFIA collaboration, *Status and Future of the 3D MAFIA group codes*, Proc. of the COMPUMAC 1989, Tokyo, IEEE-MAG 26 (1990)
- [8] M. Rook, Diplomarbeit, Jülich, Sept. 1990
- [9] A. Jackson, SLAC report No. SRC/NSS/75/103 (1975).
- [10] B. Autin, Y. Marti, CERN ISR-MA/73-17 (1973).
- [11] Y. Tang and S. Krinsky, Proc. IEEE PAC (1993).
- [12] W.H. Press et al., Numerical recipes, Cambridge Univ. Press (1986).
- [13] N. Nakamura and T. Katsura, Proc. IEEE PAC (1993).
- [14] G. Portmann and J. Bentsson, Proc. IEEE PAC (1993).

Chapter 4

Higher-order modeling of the accelerator

The model of the linear accelerator is described accurately in the previous chapter. Now, the higher-order effects of the machine are investigated. The influence of higher-order magnetic fields on the dynamics is calculated. Measurements are presented that investigate resonances.

4.1 Multipole coefficients of dipole magnets

Now, we want to determine the higher-order multipole components of the dipoles. In further sections will be shown that each higher-order multipole term is responsible for the excitation of a resonance. By assuming that $A_x = 0$ and $A_z = 0$, only transverse magnetic fields are present. The magnetic vector potential of a magnet with $2n$ poles in Cartesian coordinates is then given by:

$$A_s = \sum_n A_n f_n(x, z), \quad (4.1)$$

where f_n is a homogeneous function in x and z of order n . For example: $f_2 = x^2 - z^2$, $f_3 = x^3 - 3xz^2$, where f_2 and f_3 are components of a vector potential for a normal quadrupole and sextupole, respectively. These functions can be obtained for other multipoles from the expansion $f_n(x, z) = (x + iz)^n$. The real part corresponds to the regular multipoles and the imaginary part to the skew multipoles. For regular magnetic fields the relation between the vector potential A_n and the magnetic field is:

$$B_z(z=0) = \frac{\partial A_s}{\partial x} = \sum_{n=1}^{\infty} n A_n x^{n-1} \text{ with } A_n = \frac{1}{n!} \left(\frac{d^{n-1} B_z}{dx^{n-1}} \right)_{z=0}. \quad (4.2)$$

Looking at an ideal dipole magnet, we see that the magnetic field distribution is symmetrical with respect to the vertical median plane. The field distribution will

contain even components of x , the transverse direction, corresponding with odd n values: dipole, sextupole, decapole etc. In reality however, also other multipole components are present. In the following context, the different multipole components are defined as: B_0 : dipole, B_1 : quadrupole, B_2 : sextupole component of the measured magnetic field in transverse direction in the median plane of the dipole.

The coefficients can be obtained from $\int Bdl$ measurements with a long coil at several transverse positions in the magnets in the median plane at several currents. An example is given in figure 4.1, where strong multipole terms are present. Here the $\int Bdl$ is measured at a current of 2244 A for the dipole. The data are fitted with a sixth order polynomial to determine the multipole components.

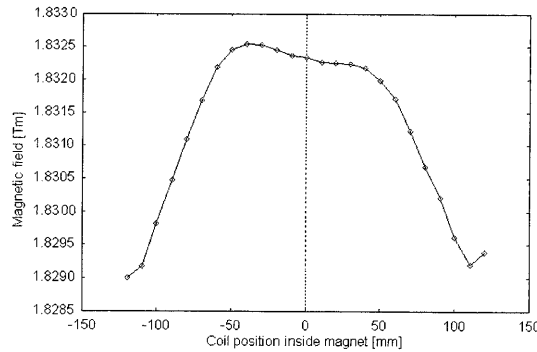


Figure 4.1: $\int Bdl$ measurements of dipole MD1 at 2244 A.

The dipole, quadrupole and sextupole coefficients from these measurements are presented in table 4.1. The measurements are accurate for the evaluation, because the particle travels through the whole dipole and not only a small section of it. In the $\int Bdl$ measurements the multipole components over the whole length of the dipole are measured. The measurements are done for all 25 dipoles at 5 different currents, namely 289 A, 1120 A, 2244 A, 3885 A and 5000 A (corresponding to proton momenta of: 269 MeV/c, 1056 MeV/c, 2120 MeV/c, 3670 MeV/c and 4720 MeV/c). The strengths of the magnetic field are also given as relative strength after dividing the value by $B\rho$. This yields an momentum independent strength.

Current [A]	B_0 [T]	B_1 [T/m]	$B_1/B\rho$ [m ⁻²]	B_2 [T/m ²]	$B_2/B\rho$ [m ⁻³]
289	0.130	-0.00132	-0.00116	-0.0200	-0.0227
1120	0.500	0.00015	0.00004	-0.0850	-0.0241
2244	1.000	0.00227	0.00032	-0.1622	-0.0229
3885	1.593	0.00439	0.00036	-0.5069	-0.0415
4000	1.618	-0.00396	-0.00031	-0.7919	-0.0629
5000	1.824	0.00838	0.00053	-9.78	-0.0621

Table 4.1: Multipole components of the $\int Bdl$ measurements in transverse direction at several dipole currents.

The quadrupole component of the 25 dipoles (one additional dipole build) at the different currents is shown in figure 4.2. The sextupole components are shown in figure 4.3. The large spread at the lowest current is due to errors in the magnetic field measurements and the geometrical differences between the magnets.

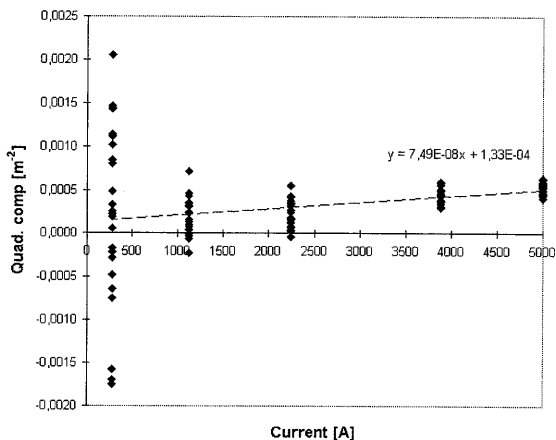


Figure 4.2: *Transverse quadrupole component of dipoles as function of current.*

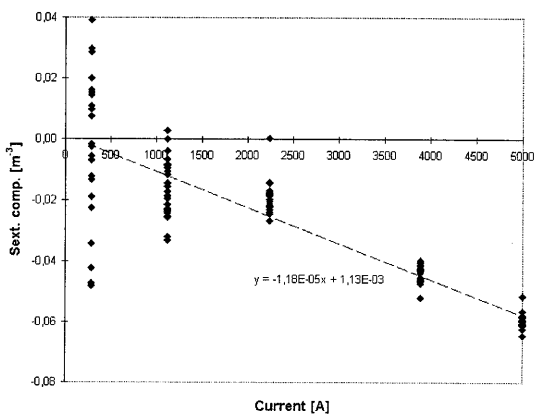


Figure 4.3: *Sextupole component of all dipoles as function of current.*

The dipoles are so arranged in the ring that 12 have the gap pointing toward the centre of the ring and the others are pointing outwards. As a result of this, the quadrupole components of the dipoles (linear field component) change their sign. The proton enters the dipole at a distance of 29.94 mm from the centre of the gap and has a curved trajectory through the dipole. In order to transform the multipole components for the proton, the following has to be done: first of all, the

quadrupole component depends on the position where the particle enters the dipole. Secondly, the sextupole component is almost constant as function of the position of the particle. We assume that the sextupole component is constant over the length of the dipole, since the sextupole component does not change very much ($<10\%$). The average transverse position of the proton inside the dipole is calculated and shown in figure 4.4. The quadrupole component is calculated with respect to the averaged position inside the dipole.

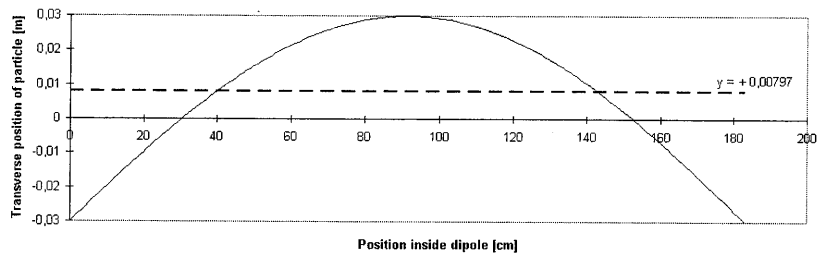


Figure 4.4: The average transverse position of the proton inside the dipole is 0.00797 m.

The quadrupole component as function of the current is shown in figure 4.5. In this case, the closed orbit is the ideal orbit. In figure 4.6, a typical closed orbit is inserted in the calculations. At flat bottom, a closed orbit with maximal deviations of 40 mm is used, at flat top of 25 mm.

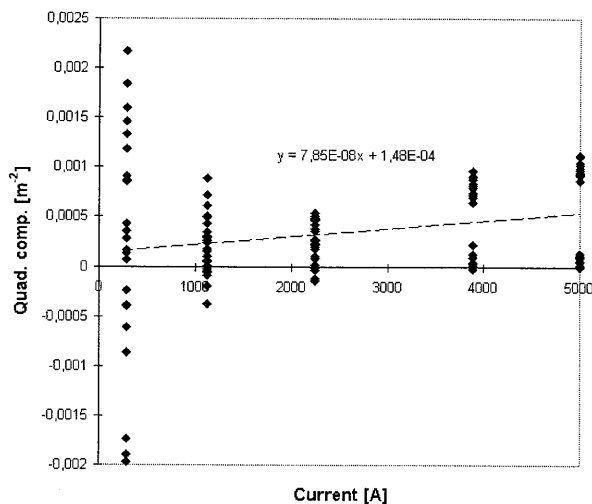


Figure 4.5: Quadrupole component with ideal closed orbit in dipole (see figure 4.4).

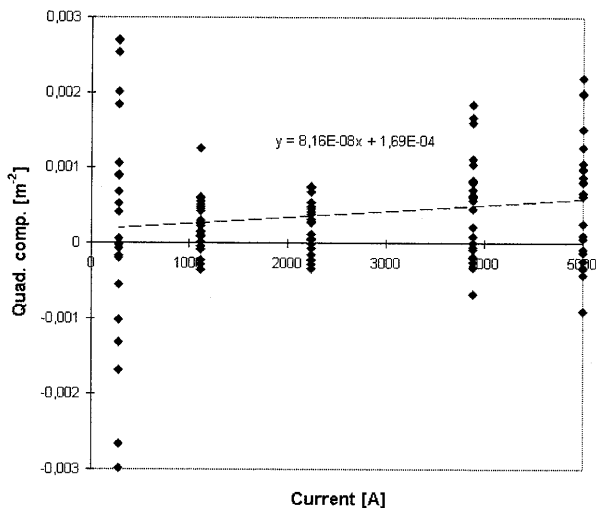


Figure 4.6: *Quadrupole component with typical closed orbit distortion.*

4.1.1 Tune-shift due to dipoles

The resulting magnetic field of a dipole yields a tune-shift. Here, the quadrupole and sextupole component of the dipoles are used to calculate their influence on the tune:

1. Quadrupole component of dipole: The tune-shift due to the quadrupole component of the dipole is given by:

$$\Delta Q = \frac{1}{4\pi} \oint \beta(s) \Delta k(s) ds \quad (4.3)$$

where $\beta(s)$ is the beta-function and $\Delta k(s)$ the quadrupole component of the dipole.

2. Sextupole component of dipole: With the following definition of the integrated sextupole strength

$$m = \frac{e}{2p_0} \frac{\partial^2 B_z}{\partial x^2} l_{se,x} \quad (4.4)$$

with $l_{se,x}$ the length of the sextupole. The quadrupole distortion ($\Delta K(s)$) of the horizontal displaced sextupole component of the dipoles are given by:

$$\Delta K(s) = 2m\Delta x \quad (4.5)$$

with Δx the horizontal displacement of the incoming beam, this leads to the tune-shift of:

$$\Delta Q = \frac{1}{4\pi} \oint \beta(s) \Delta K(s) ds. \quad (4.6)$$

Assuming a uncorrelated randomly distributed beam displacement, the rms-value of the tune-shift due to the sextupole contribution is [1]

$$\langle \Delta Q \rangle = \frac{\sqrt{M}}{2\pi} \sqrt{m^2 \beta^2} \langle \Delta x \rangle \quad (4.7)$$

where M is the total number of dipoles and the bar indicates the averaged value of the corresponding parameter. For an average displacement $\langle \Delta x \rangle$ of 0.035 m, and 0.015 m at flat bottom and flat top, respectively the tune-shift due to these sextupole components in the dipoles is approximately 0.0013.

We can calculate the tune-shift due to the dipoles. The tune-shift due to the quadrupole and sextupole components of the dipoles as function of the excitation current assuming an ideal orbit is shown in figure 4.7. For a closed orbit deviation which is non-zero, the tune-shift changes by an amount of about 0.01 with deviations of about 10 mm.

The prediction of the tune-shift has been confirmed experimentally. At a momentum of 3320 MeV/c the closed orbit was shifted with maximal deviations from -30 mm to +30 mm and the tune-shift (measure for quadrupole component of dipole) and the chromaticity (measure for sextupole component of dipole) were measured. The measured tune-shift was 0.037 (calculated 0.043) for an orbit deviation of 30 mm and -0.046 (calculated -0.072) for an orbit deviation of -30 mm. The sextupole component of the dipole was constant (within measurement inaccuracy) for all measurements.

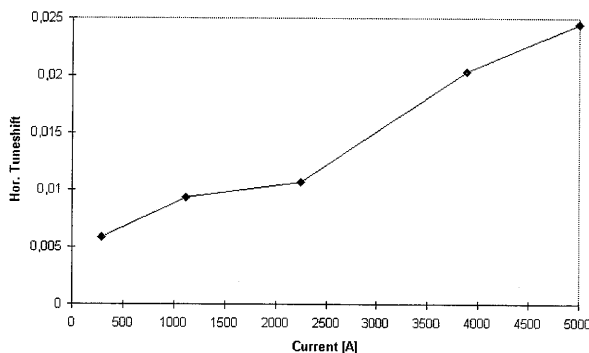


Figure 4.7: *Tune-shift as function of current with ideal closed orbit.*

The magnetic field measurements of the dipoles allow the determination of even higher-order field components. The examination of the third-order (octupole component of the dipoles) shows that it is about 0.01 m^{-4} , see figure 4.8. The large spread at the lowest currents is due to the measurement inaccuracies and the geometrical differences between the dipole magnets. The large spread at the highest currents are due to fit-errors.

Higher-order magnetic field components of the dipoles are negligible.

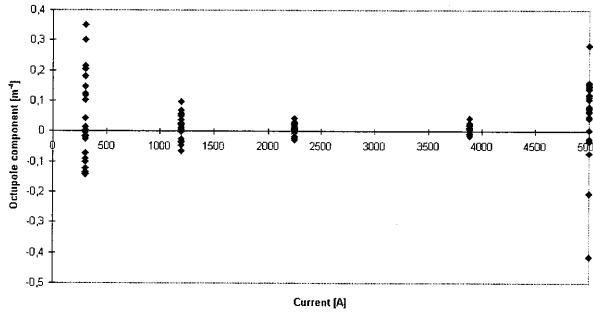


Figure 4.8: *Octupole component of all dipoles as function of current.*

4.2 Hamilton formalism for non-linear equations

For the study of non-linear resonances, the non-linear Hamilton equations of motion needs to be solved. For this purpose, the following procedure is used. A number of canonical transformations is applied which ensures that each multipole component has an one to one relationship with a term in the Hamiltonian and the lowest-order linear terms are removed. Stable and unstable fixed points, islands of stable motion, separatrices and layers which lead to unstable motion introduced in the following paragraphs can be calculated.

Taking the vector potential as obtained in Eq. 4.2, ignoring the vertical plane and taking the approximation $h \rightarrow 0$, the Hamiltonian becomes

$$H = \frac{p_x^2}{2} + \sum_{n=0} \frac{1}{B\rho} \frac{1}{n!} \frac{\partial^{n-1} B_z}{\partial x^{n-1}} x^n. \quad (4.8)$$

It is visible that each order of a multipole contributes a term to the Hamiltonian. Dipole, quadrupole and sextupole magnets are distributed in azimuth around the focusing lattice. The s -dependence in the linear approximation can be removed by a canonical transformation, see chapter 2. The s -dependence of higher-order magnetic fields can not be removed that simply, even in action-angle variables. To reveal the magnitude of the disturbance of the perfect circle, a transformation has to be applied that removes the s -dependence of the Hamiltonian. This transformation has been done by Wilson [5] and only the result is shown. The Hamiltonian from Eq. 4.8 can be written as the sum of a linear part $H_0 = QJ/R$ and a term $U(J, \phi, s)$ containing the non-linear perturbations.

$$H_1 = H_0(J) + U(J, \phi, s) \quad (4.9)$$

A generating function (F_2) generates the identity transformation with a small perturbation function $\chi(J, \phi, s)$.

$$F_2(J_2, \phi, s) = J_2 \phi + \chi(J_2, \phi, s). \quad (4.10)$$

The new and old coordinates are simply related by the first derivatives of the quantity $\chi(J, \phi, s)$

$$\begin{aligned} J &= J_2 + \frac{\partial}{\partial \phi} \chi(J_2, \phi, s), \\ \phi_2 &= \phi + \frac{\partial}{\partial J_2} \chi(J_2, \phi, s). \end{aligned} \quad (4.11)$$

The new Hamiltonian will then be

$$H_2 = H_1 + \frac{\partial \chi(J_2, \phi, s)}{\partial s}. \quad (4.12)$$

The function χ must be chosen in such a way that its differential $\partial\chi/\partial s$ cancels the s -dependence in H_2 , making H_2 a constant of motion. When H_1 is written as function of J_2 and ϕ_2 and the second-order terms are neglected we will get the following Hamiltonian:

$$\tilde{H}_2(\phi, J_2, s) = \frac{QJ_2}{R} + \frac{Q}{R} \frac{\partial \chi}{\partial \phi_2} + \frac{\partial \chi}{\partial s} + U(\phi_2, J_2, s) \quad (4.13)$$

The independent variable is still s , but it is more convenient to use the angle $\theta = s/R$. After a transformation, this gives the Hamiltonian

$$H_3(\phi_3, J_3, \theta) = QJ_3 + Q \frac{\partial \chi}{\partial \phi_3} + \frac{\partial \chi}{\partial \theta} + RU(\phi_3, J_3, \theta) \quad (4.14)$$

with $\phi_3 = \phi_2$, $J_3 = J_2$ and $H_4 = RH_3$. Separate terms containing a s -dependence (read θ -dependence) in the Hamiltonian have to be removed. If the perturbation $U(\phi_3, J_3, \theta)$ is known, the differential equation can be found and solved to find χ .

4.3 Non-linear resonances

Close to a resonance particular harmonics of the error distribution have to be taken into account. Assuming that the perturbation is periodic in both ϕ and θ and it can be expanded as a Fourier series:

$$U = \sum_{m=0}^{\infty} \sum_{n=0}^{\infty} U_{mn} e^{i(n\phi_3 - m\theta)} \quad (4.15)$$

with the corresponding coefficients

$$U_{mn} = \frac{1}{4\pi^2} \int_0^{2\pi} \int_{\phi_3}^{\phi_3+2\pi} U e^{i(n\phi_3 - m\theta)} d\theta d\phi_3. \quad (4.16)$$

Analogously to the previous section the solution for the θ -dependent component of the function χ is calculated:

$$\chi = i \sum_m \sum_n \frac{RU_{mn}}{nQ - m} e^{i(n\phi_3 - m\theta)}. \quad (4.17)$$

Again, χ can be used to calculate the non-linear distortion of the circular flowline. Close to the resonant condition the denominator becomes small, because $nQ = m$. The first-order approximation is no longer valid at this point. There is a transformation that gives a Hamiltonian H_4 which is an invariant of the motion and yields contours in phase space for a resonant term. When the generating function F_2 is used with the following form

$$F_2(\phi_3, J_4, \theta) = \phi_3 - \frac{m}{n}\theta J_4, \quad (4.18)$$

we find the new angle coordinate $J_4 = J_3$ and $\phi_4 = (\phi_3 - m\theta/n)$ with the corresponding Hamiltonian for one particular resonance

$$H_4 = \left(Q - \frac{m}{n}\right) J_4 + RU_{00}(J_4) + RU_{mn}e^{in\phi_4}. \quad (4.19)$$

The value of Q is the unperturbed tune for zero amplitude particles. The new angle coordinate means that the reference frame rotates so that for $\phi_4 = 0$ the angle θ advances n turns while ϕ_3 advances m oscillation periods. The result of this transformation is the "freezing" of the resonance in phase space. In the following subsections, we will present some calculations that show some resonances in phase space. The U_{00} term is zero for odd multipoles. Here U_{mn} is the double Fourier coefficient with respect to ϕ_4 and θ and written explicitly for any multipole with $2n$ poles

$$U_{mn} = \frac{J_1^{n/2} 2^{n/2}}{n!(B\rho)2^{n-1}} \left[\frac{1}{2\pi R} \int_0^{2\pi R} \beta^{n/2} B^{(n-1)} \exp\left(i \int_0^s n\left(\frac{1}{\beta} - \frac{Q}{R}\right) ds'\right) e^{-ims/R} ds \right]. \quad (4.20)$$

The term $B^{(n-1)}$ indicates the derivative of magnetic field component $\partial^{n-1} B_z / \partial x^{n-1}$.

4.3.1 Third-order resonance

A sextupole-driven resonance will now be taken into consideration. We suppose that the Hamiltonian expressed in Cartesian coordinates has the following form:

$$H = \frac{p_x^2}{2} + \frac{k(s)}{2} x^2 + \frac{1}{6B\rho} \frac{\partial^2 B_z}{\partial x^2} x^3. \quad (4.21)$$

It describes the linear motion of particles in the horizontal plane with one sextupole distortion. In action-angle variables (see chapter 2) the Hamiltonian is given by:

$$H_1 = \frac{Q}{R} J + \frac{(2J\beta(s))^{3/2}}{6B\rho} \frac{\partial^2 B_z}{\partial x^2} \cos^3 \phi \quad (4.22)$$

with $x = \sqrt{2J\beta(s)} \cos \phi$ and an alternative definition for ϕ :

$$\phi = \frac{Q}{R} s. \quad (4.23)$$

The trigonometrical relation

$$\cos^3 \phi = \frac{1}{4}(\cos 3\phi + 3 \cos \phi) \quad (4.24)$$

shows that the second term does not drive the non-integer third-order resonance and can be neglected. The second term in Eq. 4.22 is the perturbation U (with the approximation of a single short sextupole) and after applying the result from Eq. 4.19 H_4 becomes

$$H_4 = \left(Q - \frac{m}{3}\right)J_4 + RU_{m3} \cos 3\phi_4. \quad (4.25)$$

Rewriting H_4 after defining the following constants $\delta = Q - m/3$ and $\varepsilon = RU_{m3}/J_4^{3/2}$ gives the following Hamilton equation

$$H = \delta J_4 + \varepsilon J_4^{3/2} \cos(3\phi_4). \quad (4.26)$$

If the coefficient of the second term is small, either because the amplitude is small or the driving strength is weak, the contour in phase space will be close to a circle ($J_4 = \text{constant}$). The same will be true if the distance to the resonance, δ , is large.

Contours of constant H in $J_4 - \phi_4$ space are shown in figure 4.9 (sextupole at 0.13 T/m^2) in cartesian (left) and polar coordinates for which the radial component $\sqrt{2J_4}$ is used (right). With no sextupoles, the contours would be straight lines parallel with the x -axis (in polar coordinates circles). Here, a stable motion is seen for particles with small amplitudes. When the amplitude of the particle gets larger the motion becomes unbound and diverges towards infinite amplitude. The line defining the vertical asymptote is called the separatrix.

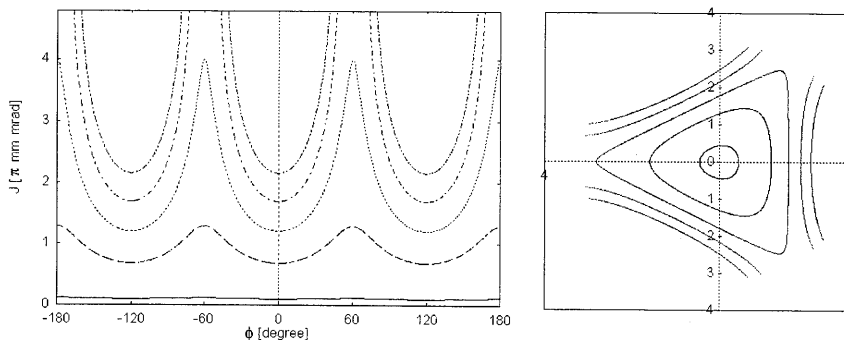


Figure 4.9: Contours of constant H in $J - \phi_4$ space with one sextupole excited at 0.13 T/m^2 . The contours have values of $0.01, 0.085, 0.16, 0.235$ and 0.31 .

Looking at the Hamilton equations for 4.26 the equations of motion become

$$\begin{aligned}\frac{\partial J}{\partial s} &= -\partial H/\partial \phi_4 = 3\varepsilon J^{3/2} \sin 3\phi_4, \\ \frac{\partial \phi_4}{\partial s} &= \partial H/\partial J = \delta + \frac{3}{2}\varepsilon J^{1/2} \cos 3\phi_4.\end{aligned}\quad (4.27)$$

When both expressions are zero a particle will stagnate in phase space, lying on a "fixed point". They are called stable fixed and unstable fixed points. In figure 4.9 no stable fixed points (islands) are visible. The position of the fixed points can be calculated using equation 4.27 in the case of a third-integer resonance. The motion as function of J will be zero whenever $\partial J/\partial s = 0$, corresponding with $\sin 3\phi_4 = 0$. Simultaneously $\partial \phi_4/\partial s$ must be zero. Above the resonance, δ is positive so that $\partial \phi_4/\partial s = 0$ only if $\cos 3\phi_4 = -1$. These conditions define three fixed points at $\phi_4 = \pi/3$, $\phi_4 = 3\pi/3$, $\phi_4 = 5\pi/3$. The amplitude of the "fixed point" is $J_{fp} = (2\delta/3\varepsilon)^2$.

In measurements we see that the tune depends on the amplitude. With larger amplitudes the tune increases. Therefore, in the Hamiltonian of Eq. 4.26 an extra term needs to be inserted, namely a detuning parameter $\alpha_{xx}J_x^2$. The Hamiltonian will look like:

$$H = \delta J + \varepsilon J^{3/2} \cos(3\phi_4) + \frac{1}{2}\alpha_{xx}J^2. \quad (4.28)$$

This term is responsible for the detuning because of an average sextupole and octupole strength of the dipole magnets in the ring that increases the tune when the amplitude of the beam is increased, see [2]. This effect has been measured and the coefficient α_{xx} is determined. The experimental procedure starts with a single bunch being kicked with various angular deflections by a pulsed deflection magnet (kicker). The subsequent beam-centroid displacement (betatron motion) is measured by two beam position monitors (BPM's). The turn-by-turn beam positions are digitised and recorded in FIFO memories. In this way the data of 200 (with 4K FIFO-length) or of 3200 (64K FIFO-length) successive turns are recorded. For more details, see [3]. The measured horizontal tune is fitted with the following function

$$Q(a) = Q_0 + \frac{1}{2}\alpha_{xx}a^2 \quad (4.29)$$

where the amplitude (a) is related to the action-angle variable $J \equiv \frac{1}{2}a^2$. The measured tune-shift is shown in figure 4.10.

The detuning factor α_{xx} has a value of about 1500 m^{-2} . Measurements with BPM24 yield similar results. Third-order resonance islands can be observed whenever the condition, $|48\pi\varepsilon/\alpha_{xx}J^{1/2}| \leq 1$, is satisfied [4]. Thus a weak third-order resonance with large detuning gives rise to third-order resonance islands. For a third-order slow extraction process, control of the detuning parameter is important in achieving good efficiency.

4.3.2 Fifth-order resonance

All single resonance Hamilton equations can be treated similar to the resonance of the past paragraph. Here, we have chosen to show a calculation done with the

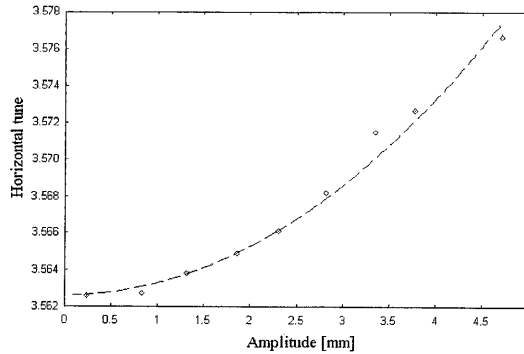


Figure 4.10: *Horizontal tune-dependence as function of the kick-amplitude at 1250 MeV/c as measured with BPM21. The dots are the measured tunes and the dashed line indicates the fitted curve.*

numerical code SIXTRACK [6]. The COSY-lattice and the non-linear magnetic fields are inserted and an additional sextupole (MXL01) has a relative strength of 10 m^{-3} . In figure 4.11 a phase space plot from a numerical calculation is shown with several contours (particle amplitude 2, 3, 4, 5 mm, respectively). Due to the sextupole, the resonance is excited and the unperturbed circles become more and more distorted with larger amplitudes. At a certain amplitude the particles are trapped inside resonance islands (five in this case). Trajectories circulate around these points within the island. The unstable fixed points are at the junction of the islands. Particles with amplitudes larger than 5 mm are outside of the stable area. Therefore their motion is unbound and their trajectory diverges and the particles collide against the beampipe.

At the centre of the resonance islands stable fixed points are situated. In order to calculate the position and width of these islands, the invariant Hamiltonian (Eq. 4.28 altered for fifth integer resonance) is used and the non-linear shift α_{xx} is included. The perturbed tune Q ($n = 5$) is given by

$$Q \approx \frac{\partial H}{\partial J} = \delta + \alpha_{xx}J + \frac{n}{2}\varepsilon J^{n/2-1} \cos m\phi_4. \quad (4.30)$$

The first two terms cancel on average when J has a resonant value J_r defined by $\alpha_{xx}J_r = -\delta$. Looking at small changes in J about J_r yields

$$(J_r - J) = -\frac{n}{2} \frac{\varepsilon}{\alpha_{xx}} J_r^{n/2-1} \cos m\phi_4. \quad (4.31)$$

Differentiation of Eq. 4.31 yields the amplitude of the fixed points. Together with $\partial H / \partial \phi_4 = 0$ the fixed points can be calculated. Stable and unstable fixed points at $\cos m\phi_4 = -1$ and $\cos m\phi_4 = +1$ are present. The fixed points are separated in J by $n\varepsilon / \alpha_{xx} J^{n/2-1}$. Within the islands, the particles circulate around these fixed

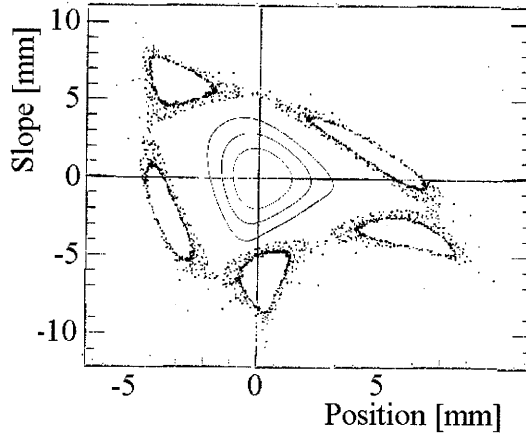


Figure 4.11: *Single resonance of fifth-order induced by MXL01. Horizontal tune of 3.5775 at the centre.*

points. The width of the islands can be calculated and is found to be

$$\Delta J_u = 2\sqrt{\frac{\varepsilon J_u^{n/2}}{\alpha_{xx}}}, \quad (4.32)$$

where J_u is that of an unstable fixed point.

4.4 Measurements of resonances

In chapter 1, the electron cooler is described and how it can be used to reduce the transverse and longitudinal motion of the protons. For the measurements in this section the proton beam was cooled at injection energy (45 MeV). For the measurements a single bunch is kicked and the betatron motion is recorded at several BPM's. The electron cooler is used to decrease the momentum spread in the bunch and so to increase the number of turns after which the coherence of the beam is lost. In figure 4.12 the number of turns that are excited after the kick (indicated with arrow) is about 40000. Without e-cooler this would be 300 turns due to the large tune-spread within the beam.

To investigate resonances, the phase-space coordinates x and p_x need to be measured. Experimentally, p_x is not a convenient quantity to measure. The variables that are actually measured are the positions x_1 and x_2 at the two BPM's which are separated in betatron phase by ϕ_{12} . After a linear transformation from phase-space coordinates from BPM1 to BPM2 (including the Twiss parameter ϕ_{12} , β_x and α_x) the following expression is found for p_{x1} after the elimination of α_x

$$p_{x1} = -x_1 \cot \phi_{12} + \frac{\sqrt{\beta_{x1}/\beta_{x2}}}{\sin \phi_{12}} x_2. \quad (4.33)$$

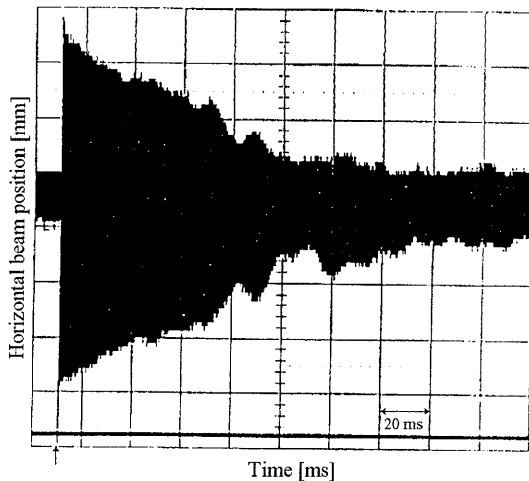


Figure 4.12: *Horizontal analogue beam position after excitation with a single bunch kick. The kick is indicated with an arrow at the bottom of the picture.*

The values of ϕ_{12} and β_{x1} and β_{x2} are needed to transform the position variables to the normalised momentum. The values can be obtained from numerical calculations.

4.4.1 Measurement of the linear coupling resonance $Q_x - Q_z$

For electron cooling solenoid fields are necessary. These fields give rise to coupling phenomena. The first coupling resonance investigated is the difference resonance $Q_x - Q_z = 0$. The tune is shifted to a point where the horizontal and vertical tune are close to each other. In figure 4.13 the measured horizontal and vertical tunes are shown.

The Hamiltonian describing the betatron motion in the presence of linear coupling $Q_x - Q_z = l$ can be approximated with [7]

$$H = \nu_x J_x + \nu_z J_z + \frac{1}{2} \alpha_{xx} J_x^2 + \alpha_{xz} J_x J_z + \frac{1}{2} \alpha_{zz} J_z^2 + C \sqrt{J_x J_z} \cos(\phi_x - \phi_z - l\theta + \chi), \quad (4.34)$$

where α_{xx} , α_{xz} and α_{zz} are the non-linear detuning parameters and C and χ are the amplitude and phase of the coupling constant. The Hamiltonian can be transformed into a resonant precessing frame by using the generating function

$$F_2(\phi_x, \phi_z, J_1, J_2) = (\phi_x - \phi_z - l\theta + \chi) J_1 + \phi_z J_2, \quad (4.35)$$

to obtain action-angle variables given by $\phi_1 = \phi_x - \phi_z - l\theta + \chi$, $\phi_2 = \phi_z$, $J_1 = J_x$ and the constant $J_2 = J_x + J_z$. The new Hamiltonian is given by H_2 with

$$H_2(J_1, \phi_1, J_2) = \delta_1 J_1 + \frac{1}{2} \alpha_{11} J_1^2 + C \sqrt{J_1 (J_2 - J_1)} \cos \phi_1 + \nu_z J_2 + \frac{1}{2} \alpha_{zz} J_2^2. \quad (4.36)$$

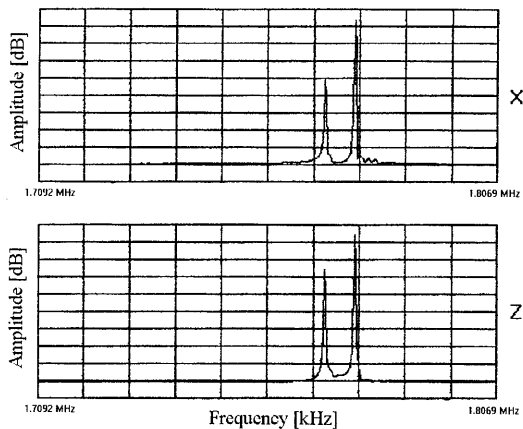


Figure 4.13: *Horizontal and vertical tune spectrum. In both spectra two peaks are visible that correspond with tunes of 3.626 and 3.634.*

Here, $\delta_1 = \nu_x - \nu_z - l + (\alpha_{xx} - \alpha_{zz})J_2$ and $\alpha_{11} = \alpha_{xx} - 2\alpha_{xz} + \alpha_{zz}$ is the effective detuning parameter at the resonance. Here, the investigated coupling resonance has $l = 0$.

For simplicity, the detuning parameters (α_{xx} , α_{xz} and α_{zz}) are set to zero. The stable fixed points for the coupling resonance are calculated from the condition that $\partial J_1 / \partial \theta = 0$ and $\partial \phi_1 / \partial \theta = 0$ in the Hamilton equations of motion, given by

$$\begin{aligned} \frac{\partial J_1}{\partial \theta} &= -\frac{\partial H_2}{\partial \phi_1} = C\sqrt{J_1(J_2 - J_1)} \sin \phi_1, \\ \frac{\partial \phi_1}{\partial \theta} &= \frac{\partial H_2}{\partial J_1} = \delta + \frac{C(J_2 - 2J_1)}{2\sqrt{J_1(J_2 - J_1)}} \cos \phi_1, \end{aligned} \quad (4.37)$$

resulting in fixed points at $\phi = 0$ and $\phi = \pi$ for $J_1 = \frac{1}{2}J_2$ when the distance from the resonance δ is zero. Using the Hamilton equations from 4.37 the following relation can be obtained

$$\frac{\partial^2 J_1}{\partial \theta^2} + C^2 J_1 = \frac{1}{2}C^2 J_2. \quad (4.38)$$

The solution at the linear coupling resonance is given by

$$J_1 = \sqrt{\frac{1}{4}J_2^2 - T^2} \cos(C\theta + \varphi) + \frac{1}{2}J_2, \quad (4.39)$$

where φ is an initial phase factor and $T = E/C$ with $|T| \leq \frac{1}{2}J_2$ and $E = C\sqrt{J_1(J_2 - J_1)} \cos \phi_1$. The oscillations about the fixed point are independent of the amplitude. Particles with different betatron tunes will be orbiting around different fixed points with different oscillation frequency.

The amplitude and phase of the complex coupling constant are given by [7]:

$$C e^{i\chi} = \frac{1}{2\pi} \int_0^{2\pi R} \sqrt{\beta_x(s)\beta_z(s)} A_{xx}(s) e^{i[\phi_x - \phi_z - (\nu_x - \nu_z)\theta]} ds, \quad (4.40)$$

where $\nu_x = Q_x/2\pi$, $\nu_z = Q_z/2\pi$ and

$$A_{xx}(s) = \left[\frac{1}{B\rho} \frac{\partial B_z}{\partial z} - \frac{B_{||}}{4B\rho} \left(\frac{1}{\beta_x} \frac{d\beta_x}{ds} - \frac{1}{\beta_z} \frac{d\beta_z}{ds} \right) - i \frac{B_{||}}{2B\rho} \left(\frac{1}{\beta_x} + \frac{1}{\beta_z} \right) \right]. \quad (4.41)$$

Here $(B\rho)^{-1} \partial B_z / \partial z$ and $B_{||} / B\rho$ are respectively the skew quadrupole and the solenoid field strengths, C is often called the magnitude of the resonance and χ the phase. When the horizontal and vertical tunes are near each other (or identical) both motions are coupled. This results in oscillations about the fixed points. The "island" tune is equal to C . For a given bunch with identical betatron tune, the particles inside the bunch will be orbiting around the two different fixed points at different "island" tunes. Therefore, the two fixed points give rise to the existence of two separate peaks with a minimal distance in both frequency spectra. The minimal tune separation between the two betatron oscillations is given by the magnitude of the coupling constant. For accelerators with periodic focusing and defocusing cell structure, the linear coupling constant is dominantly real. In our case, Eq. 4.40 is used to calculate the minimal tune separation of 0.010 (neglecting the imaginary part), the measurements shows 0.008 ± 0.001 which is in agreement with the calculation.

The beam is kicked horizontally and a BPM-signal is observed. In figure 4.14 and figure 4.15 some data for the horizontal and vertical motion near this resonance are shown. We notice in the horizontal plane that the beam starts with maximal amplitude (because of the kick). The growth in oscillation amplitude in one dimension with the corresponding decrease in amplitude in the other dimension is a characteristic of the non-linear difference resonance.

Within this time-scale there are no indications of damping of the signal (≤ 4 ms). For further evaluation, the beam position of each turn is measured digitally and saved. The monitors BPM21 and BPM24 are separated in betatron phase by $\pi/2$. Data have been taken with these two BPM's.

After changing the measured data (x, p_x) to normalised coordinates

$$Q = \sqrt{2J_1} \cos \phi_1 \text{ and } P = -\sqrt{2J_1} \sin \phi_1 \quad (4.42)$$

the measured points are plotted. In figure 4.16 the Poincaré map is presented in the resonant precessing frame. Here, the tunes are shifted so they cross the resonance.

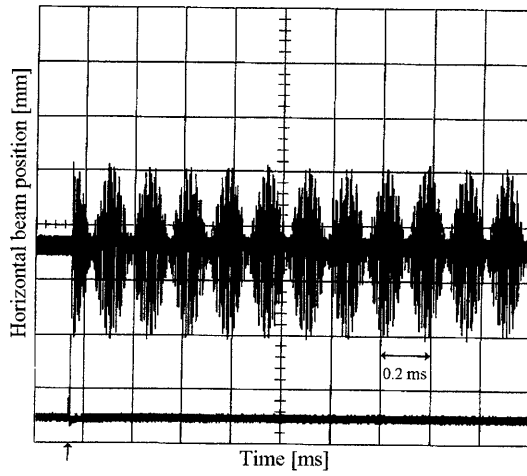


Figure 4.14: Analogue signal of horizontal BPM08. The kick is indicated with arrow at bottom of picture.

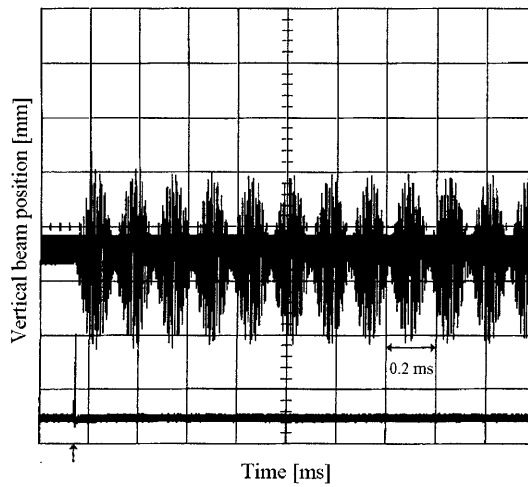


Figure 4.15: Analogue signal of vertical BPM09. The kick is indicated with arrow at bottom of picture.

In the first plot (a) the tunes are far from each other and the plot shows an almost unperturbed circular motion. In the second plot (b), the particles are on the edge of the difference resonance (constraint to 1 side of the figure). In the following picture (c) the width is increased. In picture (d) the centre of the resonance is reached. In the following pictures (e, f) the tune is shifted away from the resonance and in plot (g) the circle is unperturbed again. The phase depends on the position of the BPM's and turned out to be $\chi = -0.79$ to rotate the plot so that the coupling arc is in upright position.

The invariant circle is visible in all figures. Because the kick amplitude has the same size during the measurements and only the working point is varied, the circles have the same size. Locked on the difference resonance (d), the particles are in the resonant precessing frame and move from the centre upwards to the top and then outwards on both directions to close the curve in the centre again.

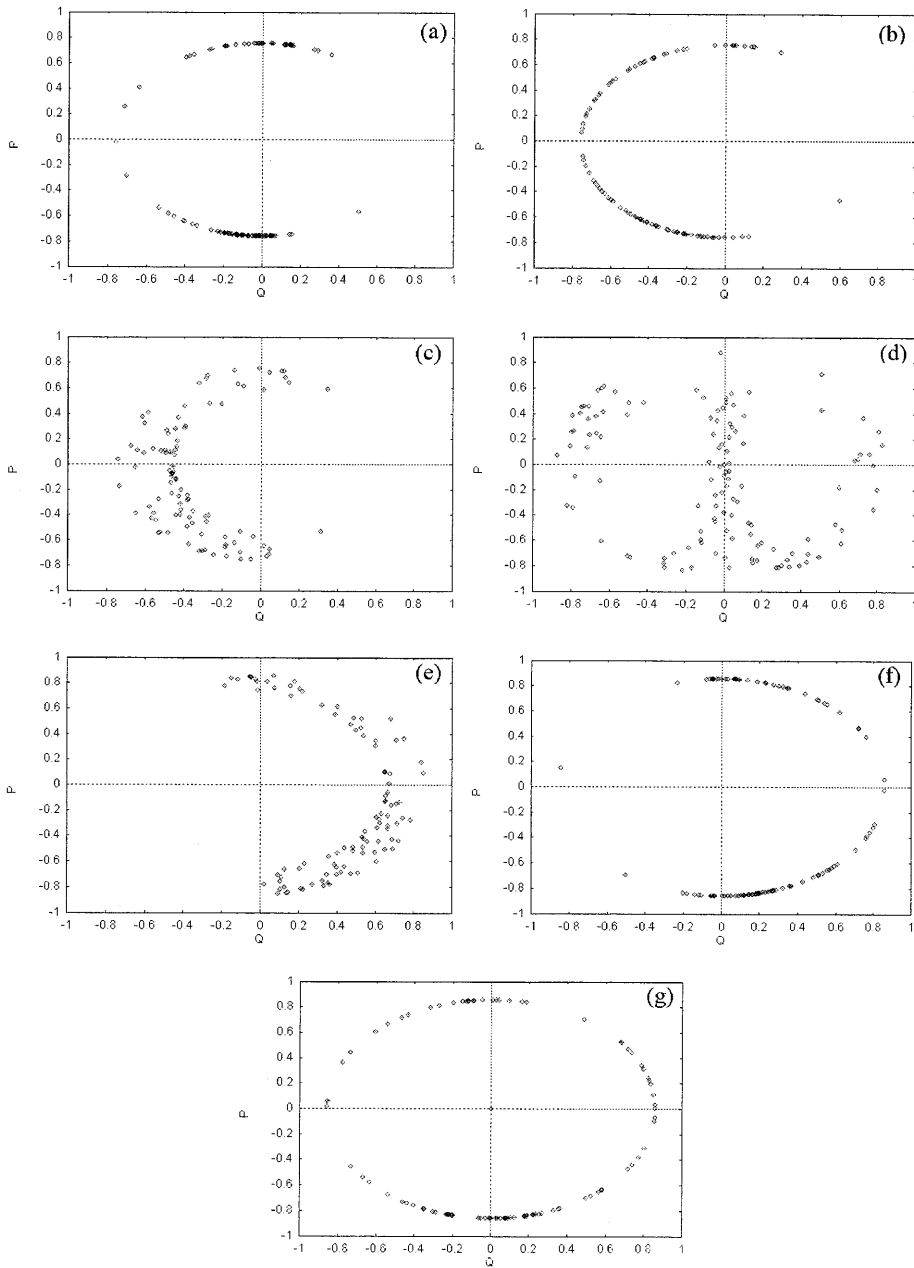


Figure 4.16: *The Poincaré map in the resonant precessing frame as measured for several working points. The tunes are shifted to cross the resonance (a - g), figure (d) shows the centre of the resonance.*

4.4.2 Measurement of third integer resonance 1

The third-order resonance at $3Q_x = 11$ was experimentally investigated. The working point is shifted to be away from the difference resonance and near the horizontal third-order resonance ($Q_x = 3.656$, $Q_y = 3.538$). The sextupole excitation is done with $MXL13 = -3\%$. The kick amplitude is varied with the following values: 1.2 mrad, 1.4 mrad and 1.6 mrad. The measured beam positions are measured and digitised. The resulting curves are converted to phase-space coordinates (x , p_x) and shown in figure 4.17. The diamonds, crosses and squares indicate increasing kick amplitude with constant sextupole strength.

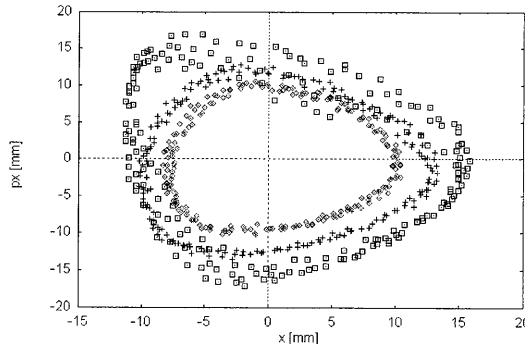


Figure 4.17: Measured data in horizontal phase space coordinates, the horizontal tune is 3.656, sextupole $MXL13 = -3\%$. Horizontal kick amplitude varied from 1.2 mrad, 1.4 mrad and 1.6 mrad.

The non-linear term usually does not perturb the particle motion in phase space except when the betatron motion is near a resonance. In this case the circle is distorted. These measured datapoints can be plotted in $J - \phi$ space as shown in figure 4.18.

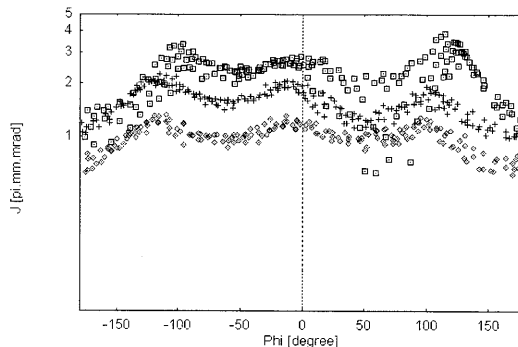


Figure 4.18: Data from figure 4.17 shown in $J - \phi$ space.

From the data plotted in figure 4.18 the size of $\epsilon J^{3/2}$ as function of J is deter-

mined, see Eq. 4.26. The resulting values are plotted in figure 4.19. With higher kick amplitudes it is more difficult to determine ε and the errorbar is larger. With Eq. 4.16 ε can be calculated since the sextupole strength of our non-linear excitation is known.

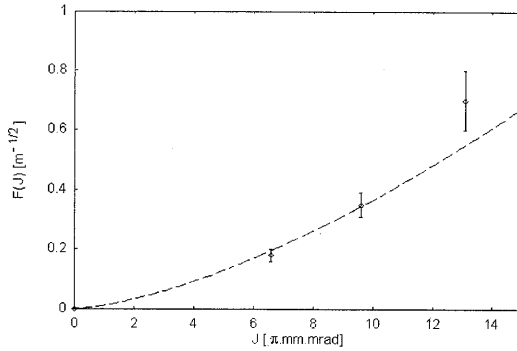


Figure 4.19: *The experimental values of $\varepsilon J^{3/2}$ as function of J . The errorbars indicate the measured points and the dashed line indicates the calculated curve (with $\varepsilon = 12 \text{ m}^{-2}$).*

The measured data and the predicted curve are roughly in agreement with each other. Beam losses occur with larger amplitude due to the aperture of the beam pipe. The calculated ε is 18.8 m^{-2} , showing some difference with the measured data.

4.4.3 Measurement of third integer resonance 2

A second measurement to investigate the third-order resonance was done. The dynamic aperture was large enough to observe stable fixed points beyond the one at the origin. Consequently, an island structure is observed in this case. Experimental investigation of this structure, starting at small amplitudes, will now be described. The transverse displacements x_1 and x_2 measured at two positions separated by a phase advance of $\pi/2$ can be used to make a phase-space plot which will be shown below. The BPM's: BPM21 and BPM24 are fitted with the 64K FIFO memory and used for the measurements. With the base tune (tune with $\varepsilon=0$) just below $11/3$, after three turns the particle returns close to where it started. The effect of the non-linearity is to make the tune increase with increasing amplitude, and so there is one amplitude, for which the tune is exactly $11/3$, and the repetition is perfect. Furthermore, there is a frequency entrainment effect causing all nearby amplitudes to "lock-on" to exactly the same tune of $11/3$, which accounts for the islands. When the beam is kicked with a small amplitude the particles are not kicked upon the resonance. At a certain amplitude the "lock-on" is visible, see figure 4.20. The sextupole strength for MXL was -8 % in these measurements. Another measurement in which sextupole $MXL1=-4$ % yielded similar results.

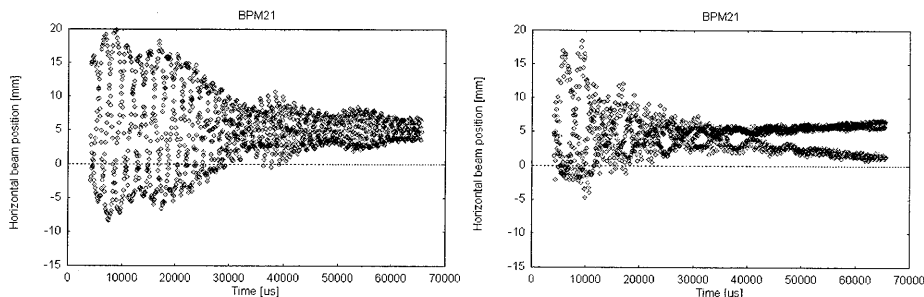


Figure 4.20: Turn-by-turn data from BPM21 with kick amplitude of 2.4 mrad and 2.8 mrad.

When the kick amplitude is increased to 3.2 mrad or higher the beam is kicked on the resonance islands. In figure 4.21 the data of BPM21 and BPM24 is shown as function of time.

When the data of BPM21 and BPM24 are combined to yield a Poincaré map the three resonance islands are visible as is shown in figure 4.22. When the kick excitation is larger the beam is excited to amplitudes that are larger than those belonging to the resonance islands.

The beam is captured in about 20 turns (kick deflection is 4 mrad) and then it stays in the stable region of the resonance. The capture in the islands is time-dependent. The interactions with the beampipe and coupling effects between the transverse and the longitudinal motion of the particles are the main reasons for this time-dependent behavior. The effect is not fully understood and needs further

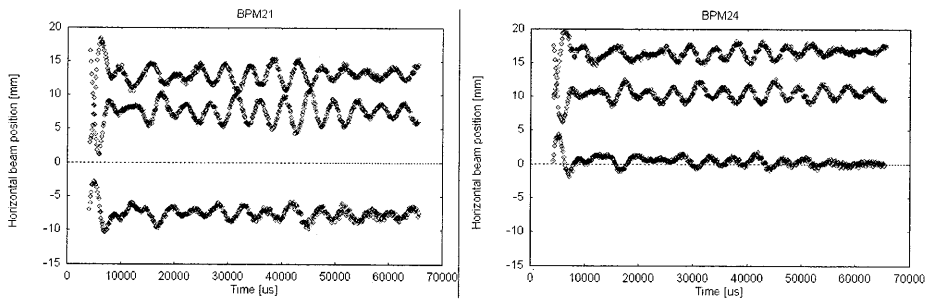


Figure 4.21: Turn-by-turn data from *BPM21* and *BPM24* with kick amplitude of 3.2 mrad.

investigation. The width of the islands is about 4 mm. The calculated width is 3.1 mm, see Eq. 4.32 with $J_u = 4.5 \pi \cdot \text{mm} \cdot \text{mrad}$.

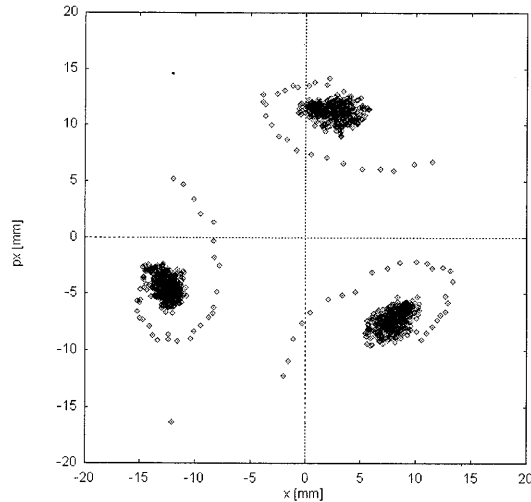


Figure 4.22: The Poincaré map where $MXL = -8\%$ and the horizontal tune is 3.666 with a kick amplitude of 3.2 mrad.

The particles inside the islands circulate around the stable fixed point. This is visible when a piece of the data of an island is extracted and plotted. Looking at figure 4.23 the motion of the particles inside the resonance is visible. After 37 turns the beam returns to its original position inside the island. The island structure can also be measured online using the analogue signals of two BPM's, see [8].

The motion around the stable fixed point is damped after a few thousand turns. When the kick deflection is larger the damping increases. For example, with a kick of 3.6 mrad the motion is damped after about 1000 turns and for a kick of 4 mrad

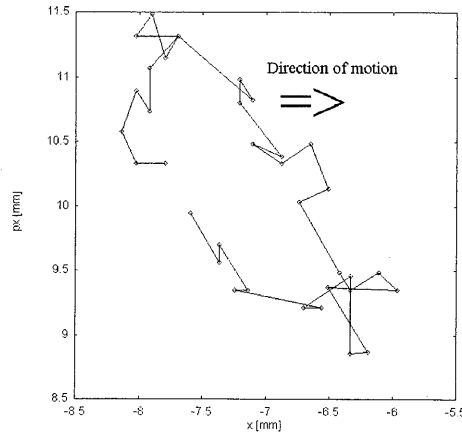


Figure 4.23: *The Poincaré map of an island. The particles circulate clockwise around the stable fixed point.*

the motion is damped after 500 turns. The reason for this time-dependent behavior of the beam is not understood.

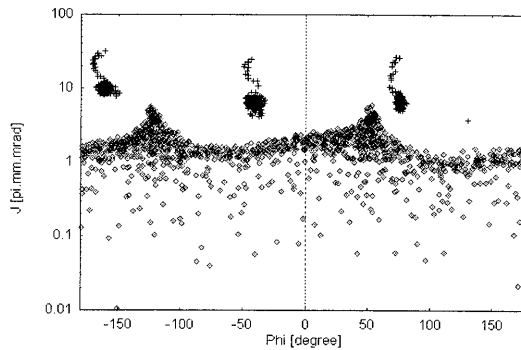


Figure 4.24: *Measured data in $J - \phi$ space. Two data-sets, one with kick excitation 1.6 mrad (indicated with diamonds) and another with kick excitation of 4 mrad (indicated with crosses).*

In figure 4.24 measured data is presented in $J - \phi$ space. The first data-set was taken with a kick of 1.6 mrad. The signal is damped in a few thousand turns. The spikes indicate the position of the unstable fixed points where larger amplitudes indicate unstable motion. Between the unstable fixed point the island-structure is visible (kick excitation 4 mrad). The beam is kicked to 25π .mm.mrad after which the signal is damped until the circular motion about the stable fixed point is reached. The amplitude of the stable fixed point is 8π .mm.mrad, the width of the islands is 4π .mm.mrad and the distance between the islands is 120° . The distance

from the resonance without kick is $\delta=0.01$. The calculated positions of the stable fixed point is done with $J_{fp} = (2\delta/3\varepsilon)^2$ and is 9π .mm.mrad.

Numerical verification was done using the numerical code SIXTRACK. The sextupole magnet MXL was powered to -8 % and the tune was shifted near the third integer resonance. The amplitude of the tracked particle was varied for several cases. The particle was tracked over 10000 turns before the calculation was stopped. The results for several amplitudes is shown in figure 4.25.

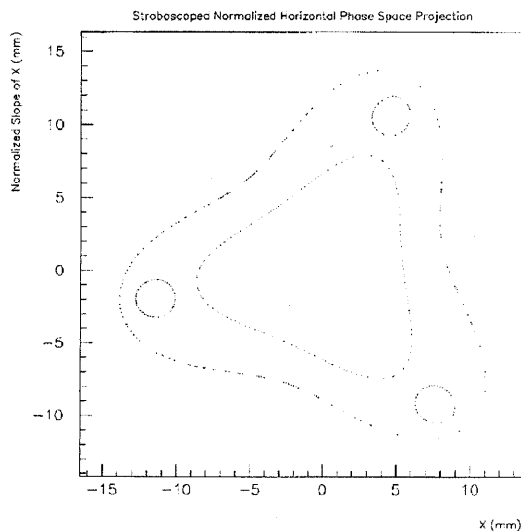


Figure 4.25: *SIXTRACK* calculation near the third integer resonance with $MXL=-8$ %. The amplitude of the beam is 8, 11 and 14 mm.

The deformation of the circular motion due to the sextupole strength is visible. Also the existence of an island structure is shown in the figure. Octupole components are present in the magnetic field distribution of the dipole magnets. They are responsible for the island structure in the measurement. These magnetic field components are also included in the *SIXTRACK* calculation. When the amplitude is further increased in the calculation the island structure vanishes again. Comparison between the calculation and the measurements is shown in figure 4.26. The numerical calculation with *SIXTRACK* (indicated with three circles) is compared with the corresponding measurement of figure 4.22 (dots).

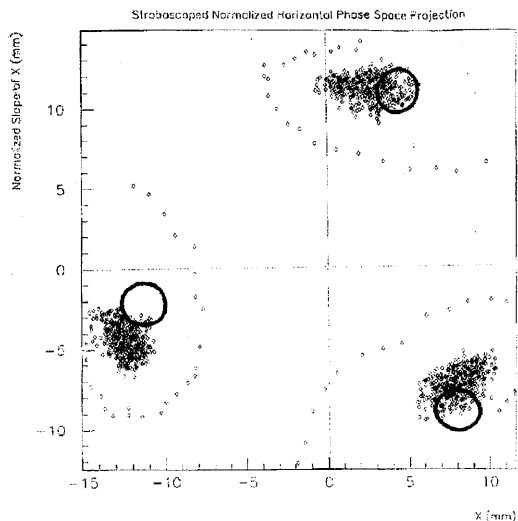


Figure 4.26: *SIXTRACK* calculation near the third integer resonance with $MXL=-8\%$ (three circles). Measurement of stable islands indicated with dots.

4.4.4 Calibration of the fast quadrupole by means of the half integer resonance

A fast quadrupole (JQ2) in the ring allows a fast tune-shift within approximately $10\ \mu\text{s}$ after which the tune is shifted back to its original value within 10-40 ms. The fast quadrupole is used for the spin preservation during the crossing of a depolarising resonance. For the calibration of the quadrupole the tune-shifting property is used.

Suppose there is a gradient error somewhere in the ring. For example, the effect of an error in a quadrupole is that of an extra thin lens. When the tune is near $2Q_y = n$ with $n = 7$ in the case of COSY this could result in no stability. When the tune is near this resonance the beam is lost. A vertical working point was chosen and the quadrupole was powered to move the tune near the half-integer resonance. The maximal tune-shift depends on the β -function at the position of the fast quadrupole, the momentum of the beam and the gradient of the quadrupole, see 4.3. The current of the fast quadrupole was increased until the beam was completely lost. Then, the vertical working point was moved between 3.541 and 3.579 and with the fast quadrupole again a fast tune-shift was done to shift the vertical tune to 3.500. With several of these points it is possible to calibrate the fast quadrupole as function of the current. Measurements show that the beam is lost in $800\ \mu\text{s}$ (approximately 1200 turns) when the tune is on the resonance. In figure 4.27 the current of JQ2, for which the beam is completely lost, is plotted as function of the vertical tune.

From the fitted curve in figure 4.27 the width of the half integer resonance

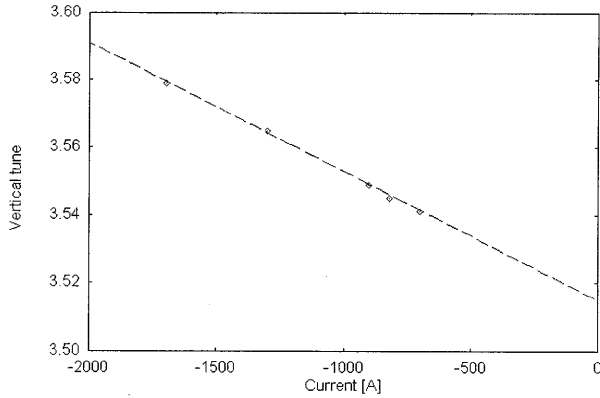


Figure 4.27: *Current of fast quadrupole jump as function of the vertical tune to reach the half integer resonance. The dots indicate the measured points and the dashed line a fitted curve.*

can be determined. A measurement at 1.92 GeV/c yields a width of 0.02 ± 0.002 . Calculations of the dynamic aperture of the ring with SIXTRACK show that the aperture is zero near 3.500. The numerical calculated width of the resonance is 0.015. The same measurement is repeated at a momentum of 3.32 GeV/c yielding similar results.

Bibliography

- [1] A. Wrulich, *Tolerances for sextupole Displacement Errors*, DESY HERA 85-11 (1985).
- [2] T. Satogata et al., *Driven Response of a Trapped Particle Beam*, Phys. Rev. Letters **68** 12 (1992), p.1838.
- [3] J. Bojowald et al., *Diagnostic Tools for the Resonant Extraction at COSY-Juelich*, DIPAC '95 (Travemünde).
- [4] S.Y. Lee, *Review of Nonlinear Beam Dynamics Experiments*, Inst. Phys. Conf. Ser. No. 131, p.249.
- [5] E.J.N. Wilson, *Nonlinear Resonances*, Proc. of CERN Accelerator School on General Accelerator Physics, CERN 87-03 (1987), p.41.
- [6] F. Schmidt, SIXTRACK, Version 1, *Single particle tracking code treating transverse motion with synchrotron oscillations in a symplectic manner*, CERN/SL/90-11(AP) (1990).
- [7] J.Y. Liu et al., *Determination of the linear coupling resonance strength using two-dimensional invariant tori*, Phys. Rev. E **49** 3 (1994) p.2347.
- [8] L.H.A. Leunissen, J. Dietrich, R. Maier, I. Mohos, D. Prasuhn, H.J. Stein, *Online analysis of measurement of third integer resonance in phase space*, to be published.

Chapter 5

Determination of Hamilton coefficients

The non-linear equations of motion can be solved using Lie algebraic tools. The third-order Hamilton coefficients can be determined from measurements with a method in which the particles are excited transverse with steerer magnets. This method is presented here and corresponding measurements are shown.

5.1 Non-linear equations of motion

Returning to the relativistic Hamiltonian, we see that this equation can be solved as shown in the previous chapter. However, these equations can be solved in another way, namely using Lie algebraic tools [1] [2] [3]. The particle motion is described by the following canonically conjugated coordinates:

$$\begin{aligned} H; & & -t, \\ p_1 = p_x - eA_x; & & x, \\ p_2 = p_y - eA_y; & & y, \\ p_3 = p_z - eA_z; & & z, \end{aligned} \tag{5.1}$$

The spatial coordinates as well as the conjugated momenta will be denoted by the canonically conjugate variables q_i and p_i , where the index i indicates the corresponding axis of the coordinate system.

It is convenient to use a more compact notation for the phase space variables q and p . Therefore, the q_i and p_i are collected into a vector with 6 variables $\vec{z} = (z_1, z_2, z_3, z_4, z_5, z_6)$ where $z_{2n} = p_n$ and $z_{2n-1} = q_n$ for $n = 1 \dots 3$. Let $z_1 \dots z_6$ be a set of canonical variables for a Hamilton dynamical system. Suppose a transformation (mapping) is made to a new set of variables $\bar{z}_1 \dots \bar{z}_6$. Such a transformation which acts on z_i and propagates them through a certain time t will be called a mapping and will be denoted by the symbol \mathcal{M} [3],

$$\mathcal{M} : z_i \rightarrow \bar{z}_i. \tag{5.2}$$

Furthermore, let M be a Jacobian matrix of map \mathcal{M} , with the matrix elements:

$$M_{ij} = \frac{\partial \bar{z}_i}{\partial z_j}. \quad (5.3)$$

The map \mathcal{M} is said to be symplectic if the corresponding matrix M is a symplectic matrix. This is true if the symplectic condition $M^T J M = J$ or $M J M^T = J$ holds (the index T means that the matrix M has to be transposed). Here, J is a 6×6 matrix and is given by:

$$J = \begin{pmatrix} 0 & 1 & 0 & 0 & 0 & 0 \\ -1 & 0 & 0 & 0 & 0 & 0 \\ 0 & 0 & 0 & 1 & 0 & 0 \\ 0 & 0 & -1 & 0 & 0 & 0 \\ 0 & 0 & 0 & 0 & 0 & 1 \\ 0 & 0 & 0 & 0 & -1 & 0 \end{pmatrix} \quad (5.4)$$

For the Hamilton systems under consideration, the mapping is symplectic. Let H be the Hamiltonian of some dynamical system which is explicitly time-dependent, then $\exp(-t : H :)$ is the Lie transformation associated with H . This transformation can be used to define a map \mathcal{M} which produces a new variable \bar{z} by the rule

$$\bar{z}_i = \exp(-t : H :) z_i, \quad i=1..6. \quad (5.5)$$

Note that the time t may be regarded as a simple parameter. Here, the Lie operator $: H : f$ is defined in terms of Poisson brackets by:

$$: H : f = [H, f] = \sum_{i=1}^3 \left[\frac{\partial H}{\partial q_i} \frac{\partial f}{\partial p_i} - \frac{\partial f}{\partial p_i} \frac{\partial H}{\partial q_i} \right]. \quad (5.6)$$

In an analogous way, powers of $: H :$ are defined by taking repeated Poisson brackets. For example, $: H :^0$ is defined to be the identity operator. Furthermore, $: H :^2$ is defined by the relation

$$: H :^2 f = [H, [H, f]]. \quad (5.7)$$

The Lie-transformation associated with the Lie operator is defined by

$$\exp(: H :) = \sum_{n=0}^{\infty} \frac{: H :^n}{n!} \quad (5.8)$$

The Lie transformation has several remarkable properties. One of these properties is the so called factorization property. We will go into detail about this property, because it is very useful in calculating transfer maps, for example for optical elements in accelerators.

5.1.1 Factorisation properties of Lie transformations

The factorisation theorem is given by [2].

Let \mathcal{M} be a symplectic mapping which maps the origin into itself. That is, the relation between the \bar{z}_i 's and z_i 's is assumed to be expressible in a power series of the form $\bar{z}_i = \sum_j R_{ij} z_j$ + higher-order terms in z_i . Where R_{ij} is the first-order transfer matrix.

Under these conditions the map \mathcal{M} can be written as a product of Lie-transformations (factored product representations, see [1]),

$$\mathcal{M} = \dots \exp(: f_3 :) \exp(: f_2 :) \exp(: f_1 :) \exp(: f_0 :), \quad (5.9)$$

where the functions f_m are homogeneous polynomials of exact order m in the variables $z_1 \dots z_6$.

Suppose, the factored product representation is truncated at any point. Then the resulting expression is still a symplectic map because each term in the product is a symplectic map. Also, if truncation consists of dropping all terms beyond $\exp(: f_m :)$ for some m , then the truncated map still is in agreement with the original map up to order $(m - 1)$ in z .

If one drops all terms beyond those involving the quadratic polynomials, this will lead to a lowest order approximation, called the first-order or linear approximation. The remaining factors $\dots \exp(: f_4 :) \exp(: f_3 :)$ represent non-linear corrections to the first-order approximation.

5.2 Non-linear Hamiltonian coefficients

It is now possible to calculate the transfer matrix M of a particle when its Hamiltonian is known and to write it in matrix form.

To solve the Hamilton flow for a particular problem, the first step is to expand H in a power series about the design orbit to give an expression in the form

$$H = H_0 + H_1 + H_2 + H_3 + \dots \quad (5.10)$$

where H_m denotes a homogeneous polynomial of exact order m . In a polynomial of order m , only the terms z_i^m , $z_i^{m-1} z_j$, $z_i^{m-2} z_j^2 \dots z_i z_j^{m-1}$ and z_j^m occur. For a Hamilton flow which maps the origin into itself, the function H_0 is the constant part of the Hamiltonian and the function H_1 can be set to zero by a transformation. The polynomial H_2 describes the paraxial approximation and the sum of the polynomials $H_3 + H_4 + \dots$ describes the higher-order corrections. Substitution of 5.10 in 5.5 yields

$$\begin{aligned} \mathcal{M} &= \exp[-t(: H_0 : + : H_1 : + : H_2 : + : H_3 : + \dots)] \\ &= \dots \exp(: f_3 :) \exp(: f_2 :) \exp(: f_1 :) \exp(: f_0 :). \end{aligned} \quad (5.11)$$

Since the constant part of the Hamiltonian is independent of phase-space coordinates, the Lie operator $: H_0 :$ operating on phase-space coordinates always yields zero. The operator $: H_1 :$ operating on phase-space coordinates also yields zero. Therefore, $\exp(: f_0 :)$ and $\exp(: f_1 :)$ are unity operators.

The calculation of f_2 and f_3 can be carried out with the aid of the formal integral identity, see ref. [2]. One finds the results

$$f_2 = -t \int_0^1 d\tau \exp[\tau t : H_1 :] H_2 \quad (5.12)$$

$$f_3 = -t \int_0^1 d\tau \exp[\tau t : H_2 :] H_3 \quad (5.13)$$

$$f_4 = -t \int_0^1 d\tau \exp[\tau t : H_3 :] H_4 \quad (5.14)$$

etc. where f_2 can be written as $f_2 = -tH_2$ since the operator $\exp(: H_1 :)$ is the unity operator. So in order to calculate the second-order coefficients, the first-order solution needs to be known and so on.

5.3 Example: magnetic sextupole

Consider an ideal magnetic sextupole of length L . End effects are neglected and a perfect magnetic-field symmetry is assumed. The definition of the coordinates is shown in figure 5.1.

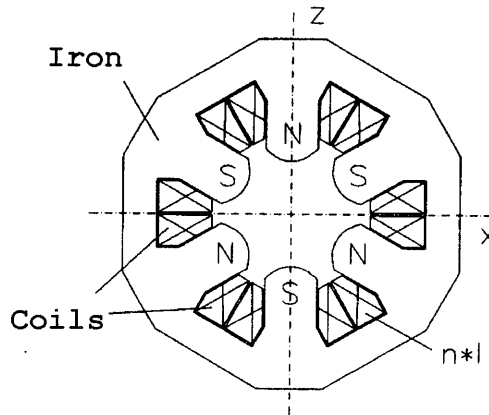


Figure 5.1: Definition of a cartesian coordinate system for the description of charged particle trajectories in a sextupole.

The Hamiltonian \mathcal{H} which describes the motion of an ultra relativistic charged particle in a magnetic sextupole is given by:

$$\mathcal{H} = \sqrt{m_0^2 c^4 + c^2(P_s - eA_s)^2 + c^2(P_x - eA_x)^2 + c^2(P_z - eA_z)^2} \quad (5.15)$$

where c is the speed of light, m_0 the restmass of the particle and P_i the canonical momentum. The following vector potential is applicable:

$$\begin{aligned} A_x &= A_z = 0 \\ A_s &= m(xz^2 - \frac{x^3}{3}), \end{aligned} \quad (5.16)$$

with $m = \partial^2 B_z / \partial x^2$. The reference orbit of a reference particle passes through the center of the sextupole. The reference orbit can be written by the equations:

$$\begin{aligned} P_s &= 0, & s &= ct + \text{constant} \\ P_x &= 0, & x &= 0 \\ P_z &= 0, & z &= 0. \end{aligned} \quad (5.17)$$

After a transformation to the following Hamiltonian $K = -P_s$, where s is the independent variable

$$K = -\sqrt{\frac{E^2}{c^2} - m_0^2 c^2 - P_x^2 - P_z^2 - em(xz^2 - \frac{x^3}{3})} \quad (5.18)$$

we describe the particle movement with respect to the reference trajectory with the energy $-E = \sqrt{m_0^2 c^4 + c^2 P_t^2}$. After a canonical transformation with a generating function F_2 we get a new Hamiltonian H which maps the origin onto itself (polynomials in H_1 are zero):

$$\begin{aligned} F_2 &= xp_x + zp_z + (t - \frac{s}{c})(E_0 + E_t) \\ H &= K + \frac{\partial F_2}{\partial s}. \end{aligned} \quad (5.19)$$

Here, t , x and z are the old coordinates, the p_i 's are new canonical momenta and $-E_0$ is the reference energy of the particle. The Hamiltonian is given by:

$$H = -\sqrt{\frac{(E_0 + E_t)^2}{c^2} - m_0^2 c^2 - p_x^2 - p_z^2 - em(xz^2 - \frac{x^3}{3})} - \frac{(E_0 + E_t)}{c}. \quad (5.20)$$

Writing the Hamiltonian as a sum of homogeneous polynomials of order m in t , x , z , E_t , p_x and p_z yields

$$H = H_0 + H_1 + H_2 + H_3 + \dots \quad (5.21)$$

with

$$\begin{aligned} H_0 &= \frac{m_0^2 c^2}{p_0}, \\ H_1 &= 0, \\ H_2 &= \frac{p_x^2}{2p_0} + \frac{p_z^2}{2p_0} + \frac{m_0^2 E_t^2}{2p_0^3}, \\ H_3 &= \frac{m_0^2 E_t^3}{2cp_0^4} + \frac{E_t(p_x^2 + p_z^2)}{2cp_0^2} - em(xz^2 - \frac{x^3}{3}), \end{aligned} \quad (5.22)$$

with p_0 the design mechanical momentum. The transfer matrix \mathcal{M} is then given by

$$\mathcal{M} = \exp(-l : H :) = \exp(-l : (H_2 + H_3 + \dots) :), \quad (5.23)$$

here is l the independent variable (distance through sextupole). We will now calculate the transfer matrix to second-order.

5.3.1 First-order terms

The second-order Hamiltonian can be split into three parts, i.e. for the two independent transverse dimensions and the time-dependent direction. This separation is not necessary, but it simplifies the calculations. The separation is given by:

$$H_2 = H_2^s + H_2^x + H_2^z, \quad (5.24)$$

with

$$\begin{aligned} H_2^s &= \frac{m_0^2 E_t^2}{2p_0^3} \\ H_2^x &= \frac{p_x^2}{2p_0} \\ H_2^z &= \frac{p_z^2}{2p_0} \end{aligned} \quad (5.25)$$

The first-order transfer matrix for the x -direction is given by:

$$\exp(-l : H_2^x :) \begin{pmatrix} x \\ p_x \end{pmatrix} = \begin{pmatrix} 1 & l \\ 0 & p_0 \end{pmatrix} \begin{pmatrix} x \\ p_x \end{pmatrix}, \quad (5.26)$$

and the same transfer matrix holds for the vertical direction.

5.3.2 Second-order terms

For this, H_3 is split into three parts for convenience. This separation is given by:

$$H_3 = H_3^M + H_3^{p1} + H_3^{p2} \quad (5.27)$$

with,

$$\begin{aligned} H_3^M &= -em(xz^2 - \frac{x^3}{3}) \\ H_3^{p1} &= \frac{m_0^2 E_t^3}{2cp_0^4} \\ H_3^{p2} &= \frac{E_t(p_x^2 + p_z^2)}{2cp_0^2}. \end{aligned} \quad (5.28)$$

To calculate the second-order terms of a sextupole, the following function must be evaluated

$$f = -l \int_0^1 d\tau \exp(\tau l : H_2 :) H_3. \quad (5.29)$$

This can be done for all three terms of H separately. Since $\exp(-l : H_2 :)$ is known, the integral can be easily calculated. The calculations finally yield:

$$f = -lH_3^{p1} - lH_3^{p2} + f_M \quad (5.30)$$

with the transverse second-order term f_M given by:

$$\begin{aligned} f_M = & -eml \left[xz^2 - \frac{x^3}{3} + \frac{l}{2p_0} (x^2 p_x - 2xz p_z - z^2 p_x) \right. \\ & \left. + \frac{l^2}{3p_0^2} (x p_z^2 + 2z p_x p_z - x p_x^2) + \frac{l^3}{4p_0^2} \left(\frac{p_x^2}{3} - p_x p_z^2 \right) \right]. \end{aligned} \quad (5.31)$$

Observe that the first two terms of f depend on t . This means that these two terms describe the chromatic effects of a sextupole.

Looking at the transverse second-order effects of the motion of a charged particle in a sextupole and only considering a mono-energetic beam results in $E_t = 0$. To calculate the second-order coefficients of, for example, the horizontal motion through the whole sextupole with length L , the following mapping has to be carried out:

$$\mathcal{M}x = \exp(: f :) \exp(: H_2 :) x + \mathcal{O}(3), \quad (5.32)$$

which is:

$$\mathcal{M}x = \exp(: f :) x - \frac{L}{p_0} \exp(: f :) p_x. \quad (5.33)$$

For simplicity, a beam with no transverse momenta is taken so that \mathcal{M} is

$$\mathcal{M}x = x + \frac{emL^2}{2p_0} (z^2 - x^2) \quad (5.34)$$

However, in the general case we have $E_t \neq 0$, $p_x \neq 0$ and $p_z \neq 0$. The second-order coefficients for the horizontal motion are now given by:

$$\begin{aligned} \mathcal{M} = & x + \frac{Lp_x}{p_0} + \frac{emL^2}{2p_0} (z^2 - x^2) + \frac{5emL^3}{3p_0^2} (z p_z - x p_x) + \frac{emL^4}{12p_0^3} (p_z^2 - p_x^2) \\ & - \frac{L}{cp_0^2} E_t p_x + \mathcal{O}(3), \end{aligned} \quad (5.35)$$

and for the vertical motion:

$$\begin{aligned} \mathcal{M} = & z + \frac{Lp_z}{p_0} + \frac{emL^2}{p_0} xz + \frac{emL^3}{3p_0^2} (x p_z + z p_x) + \frac{emL^4}{6p_0^3} (p_x p_z) \\ & - \frac{L}{cp_0^2} E_t p_z + \mathcal{O}(3), \end{aligned} \quad (5.36)$$

Here we see the dependence on the second-order terms of a sextupole in the horizontal plane. Therefore, large second-order effects can be seen at low energy with long sextupoles within a large magnetic field.

5.4 Third-order Hamiltonian coefficients

A method has been developed to measure the third-order Hamilton coefficients [4]. This method utilises two horizontal and two vertical steerers (orbit correction dipoles) that are excited by low frequency signals that are far of the betatron oscillations (around 100 Hz) and have small amplitudes (about 0.1 mrad). The response of the beam is measured by at least four BPM's (beam position monitors), two horizontal and two vertical ones. The BPM signal is dominated by the signals at the excitation frequencies. When the correctors are excited at four different frequencies, a total of 17 different frequencies can be observed in the frequency spectrum at each of the BPM's. These mixing frequencies are generated by non-linearities in the accelerator ring and the Hamilton coefficients can be extracted from the amplitudes of the mixing frequencies. The theoretical background is presented in this section. The orbit response due to the third-order non-linearities that are expected at the BPM's is calculated.

We want to determine the third-order resonance terms that characterise the one-turn map \mathcal{M} , which now can be written as $\mathcal{M} = \exp(- : H :)R$. Here, R is the first-order transfer matrix and H is the third-order Hamiltonian which has the following form

$$\begin{aligned}
 H_3 = & h_1 x^3 + h_2 x^2 x' + h_3 x^2 z + h_4 x^2 z' + h_5 x x'^2 + h_6 x x' z + h_7 x x' z' + h_8 x z^2 \\
 & + h_9 x z z' + h_{10} x z'^2 + h_{11} x'^3 + h_{12} x'^2 z + h_{13} x'^2 z' + h_{14} x' z^2 + h_{15} x' z z' \\
 & + h_{16} x' z'^2 + h_{17} z^3 + h_{18} z^2 z' + h_{19} z z'^2 + h_{20} z'^3.
 \end{aligned} \tag{5.37}$$

The steerer magnets as well as the BPM's are positioned at several places in the accelerator ring. All calculations are done with respect to the beginning of the beamline (chosen to be the start of the target telescope) and the steerer kick can be back-propagated to give:

$$\vec{\varepsilon} = \hat{R}_c^{-1} \begin{pmatrix} 0 \\ \varepsilon_c \sin \omega_c t \\ 0 \\ 0 \end{pmatrix}, \vec{\varepsilon} = \hat{R}_c^{-1} \begin{pmatrix} 0 \\ 0 \\ 0 \\ \varepsilon_c \sin \omega_c t \end{pmatrix}, \tag{5.38}$$

for a horizontal, respectively, vertical steerer and where \hat{R}_c is the transfer matrix from the start of the beamline to the corrector c . The frequency is denoted by ω_c and its amplitude by ε_c . The start of the beamline is denoted by $\vec{x} = (x, x', z, z')$. The total map can be written as

$$\vec{x}_f = \exp(- : H_3 :) R(\vec{x}_i + \vec{\varepsilon}) \tag{5.39}$$

where $\vec{\varepsilon} = \sum_{c=1}^4 \vec{\varepsilon}_c$ is the sum of the back-propagated kicks of the four correctors. Since the frequencies are very small, the orbit will follow the corrector kicks and oscillations around the new reference orbit are the result. This gives a stationary point ($x_f = x_i$) and Eq. 5.39 yields

$$\vec{x} = (\exp(- : H_3 :) - 1) R(\vec{x} + \vec{\varepsilon}) + R(\vec{x} + \vec{\varepsilon}) \tag{5.40}$$

which can be written as

$$\vec{x} = (1 - R)^{-1} [R\vec{\varepsilon} - :H_3 : (R(\vec{x} + \vec{\varepsilon}))]. \quad (5.41)$$

Here the exponential is expanded in first-order. The Lie operator $:H_3 :$ operates on the quantity $R(\vec{x} + \vec{\varepsilon})$ resulting in a non-linear equation. Because the Hamiltonian H_3 is a third-order polynomial and the explicit evaluation of $:H_3 :$ yields a quadratic expression in the components of \vec{x} . These equations can be solved by calculating the individual Poisson brackets and yields

$$\begin{aligned} [H_3, x] &= -h_2x^2 - 2h_5xx' - h_6xz - h_7xz' - 3h_{11}x'^2 - 2h_{12}x'z - 2h_{13}x'z' - h_{14}z^2 \\ &\quad - h_{15}zz' - h_{16}z'^2 \\ [H_3, x'] &= 2h_1x^2 + 2h_2xx' + 2h_3xz + 2h_4xz' + h_5x'^2 + h_6x'z + h_7x'z' \\ &\quad + h_8z^2 + h_9zz' + h_{10}z'^2 \\ [H_3, z] &= -h_4x^2 - h_7xx' - h_9xz - 2h_{10}xz' - h_{13}x'^2 - h_{15}x'z - 2h_{16}x'z' - h_{18}z^2 \\ &\quad - 2h_{19}zz' - 3h_{20}z'^2 \\ [H_3, z'] &= h_3x^2 + h_6xx' + 2h_8xz + h_9xz' + h_{12}x'^2 + 2h_{14}x'z + h_{15}x'z' + 2h_{17}z^2 \\ &\quad + 2h_{18}zz' + h_{19}z'^2 \end{aligned} \quad (5.42)$$

The previous equations can be rewritten as a matrix equation in the following manner

$$[H_3, x_\alpha] = \sum_{j=1}^{20} \sum_{k=1}^{10} a_{\alpha jk} h_j z_k \quad (5.43)$$

where the four components of \vec{x} are x_α , defining z_k as a vector that contains the ten quadratic monomials in the following order: x^2 , xx' , xz , xz' , x'^2 , $x'z$, $x'z'$, z^2 , zz' , z'^2 , and a $4 \times 20 \times 10$ matrix $a_{\alpha jk}$ contains the numerical coefficients of Eq. 5.42 and the index j runs over all third-order monomials. The solution of equation 5.41 can now be presented as a superposition of the excitation frequencies and their mixing frequencies

$$\vec{x} = \vec{x}_0 + \sum_{c=1}^4 \vec{x}_{1,c} \sin \omega_c t + \sum_{j=1}^{16} \vec{x}_{2,j} \cos \tilde{\omega}_j t \quad (5.44)$$

where $\tilde{\omega}_j$ runs over the mixing frequencies, subscript c labels the four correctors and subscripts 0, 1 and 2 label the frequency mixing order. Notice that the mixing frequencies only have a cosine-like response. They are defined in the following order: $2f_1$, $f_1 + f_2$, $f_1 - f_2$, $f_1 + f_3$, $f_1 - f_3$, $f_1 + f_4$, $f_1 - f_4$, $2f_2$, $f_2 + f_3$, $f_2 - f_3$, $f_2 + f_4$, $f_2 - f_4$, $2f_3$, $f_3 + f_4$, $f_3 - f_4$, $2f_4$ corresponding to the four excitation frequencies f_1 , f_2 , f_3 and f_4 .

1. The first-order response of the orbit with respect to the excitation signals is given by

$$\sum_{c=1}^4 \vec{x}_{1,c} \sin \omega_c t = (1 - R)^{-1} R \vec{\varepsilon}. \quad (5.45)$$

2. The next iteration is to calculate the second-order response by inserting the left hand side of the first-order solution into Eq. 5.41 and calculate the Lie-operator. We get

$$\vec{x}_0 + \sum_{j=1}^{16} \vec{x}_{2,j} \cos \tilde{\omega}_j t = -(1-R)^{-1} : H_3 : \left[R \left(\sum_{c=1}^4 \vec{x}_{1,c} \sin \omega_c t + \vec{\epsilon} \right) \right]. \quad (5.46)$$

The left hand side describes the response of the beam position at the start of the beamline to the excitations due to third-order aberrations. In order to get the response at the position of a BPM $\vec{x} = (x, x', z, z')$ must be propagated to the BPM position by multiplying with the transfer matrix from the start of the beamline to the BPM. The BPM pattern is contained in the first or third component of the vector

$$\vec{R} \left(\vec{x}_0 + \sum_{j=1}^{16} \vec{x}_{2,j} \cos \tilde{\omega}_j t \right) \quad (5.47)$$

for the horizontal, respectively the vertical plane. A vector $\vec{v}_c \sin \omega_c t = (1-R)^{-1} R \vec{\epsilon}_c$ is defined. After applying the Lie operator and evaluating the result, the cosine-like response of the beam, is clearly seen, see [4]:

$$\begin{aligned} & \sum_{c=1}^4 \vec{v}_{c,\alpha} \sin \omega_c t \sum_{j=1}^4 \vec{v}_{j,\beta} \sin \omega_j t = \sum_{m=1}^{17} b_{km} \cos \tilde{\omega}_m t = \\ & \frac{1}{2} \sum_{j=1}^4 \nu_{c,\alpha} \nu_{j,\beta} + \frac{1}{2} \sum_{c < j}^4 (\nu_{c,\alpha} \nu_{j,\beta} + \nu_{j,\alpha} \nu_{c,\beta}) \cos(\omega_c - \omega_j) t \\ & - \frac{1}{2} \sum_{j=1}^4 \nu_{c,\alpha} \nu_{j,\beta} \cos 2\omega_j t - \frac{1}{2} \sum_{c < j}^4 (\nu_{c,\alpha} \nu_{j,\beta} + \nu_{j,\alpha} \nu_{c,\beta}) \cos(\omega_c + \omega_j) t. \end{aligned} \quad (5.48)$$

The indices α and β denote the four components of the vector \vec{v}_c . Here we defined a 10×17 matrix b_{km} where k runs over the ten different monomials of the second-order Hamiltonian and m runs over the 17 different frequencies.

5.5 Calculation of third-order Hamilton orbit response

The presented method in the preceding paragraph can be coded in a computer. The matrices R , $a_{\alpha j k}$ and $b_{k m}$ can be calculated using the numerical code COSY INFINITY. In the calculations misalignments and magnetic field deviations of the dipole magnets are included. The first-order transfer matrix and the third-order coefficients h_i can be calculated using this program. From there on, the Poisson brackets (Lie transformation) can be calculated and the matrix $a_{\alpha j k}$ is determined. After back-propagating the corrector magnets to the start of the beamline (using \vec{R}^{-1} for each of them) the vector \vec{v}_c is calculated and the matrix $b_{k m}$ is determined. All the information about the orbit correctors like their position and amplitude are contained in the matrix $b_{k m}$. Equation 5.46 can finally be written as a matrix representation

$$c_{\alpha j m} = \sum_{\beta=1}^4 (1-R)_{\alpha\beta}^{-1} \sum_{k=1}^{10} a_{\beta k j} b_{k m}. \quad (5.49)$$

The matrix $c_{\alpha jm}$ contains the information by how much coordinate x_α at the start of the beamline changes at frequency $\tilde{\omega}_m$ due to the Hamilton aberration h_j and the four excitation frequencies ω_c . Now we know the response of the beam at injection it is possible to determine the response at a particular BPM by left-multiplying $c_{\alpha jm}$ with the transfer matrix \tilde{R} from the start of the beamline upto the particular BPM. For a horizontal BPM ($\beta = 1$) or vertical BPM ($\beta = 3$) the result is

$$T(m, j) = \sum_{\alpha=1}^4 \hat{R}_{\beta\alpha} c_{\alpha jm}. \quad (5.50)$$

The matrix T contains the dependence of the amplitude belonging to the frequency $\tilde{\omega}_m$ due to aberration h_j .

5.6 Simulations of orbit response

In this paragraph the response at a BPM as function of the steerer excitation is calculated. This is necessary to determine whether it is possible to detect the mixing frequencies to study the influence of sextupole excitation. First, the third-order aberrations (third-order Hamilton coefficients) have to be calculated. Then, the four steerer magnets are used for the excitation of the beam with four different frequencies. Finally, the response at a BPM is calculated and the corresponding Fast-Fourier-Transformation-spectrum is calculated.

The third-order Hamilton aberrations due to fringing fields and misalignments are shown in figure 5.2.

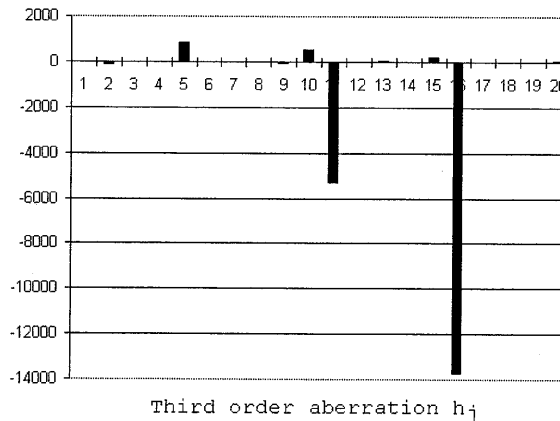


Figure 5.2: The third-order Hamilton coefficients in the horizontal plane as calculated with COSY INFINITY for a specific optic of the accelerator ring.

The same calculations have been done with one difference, all sextupoles are excited at 50% of their maximal value. This is done to show the growth of the

aberrations and the result is shown in figure 5.3. Only a few of the third-order terms are large and have a small influence on the orbit.

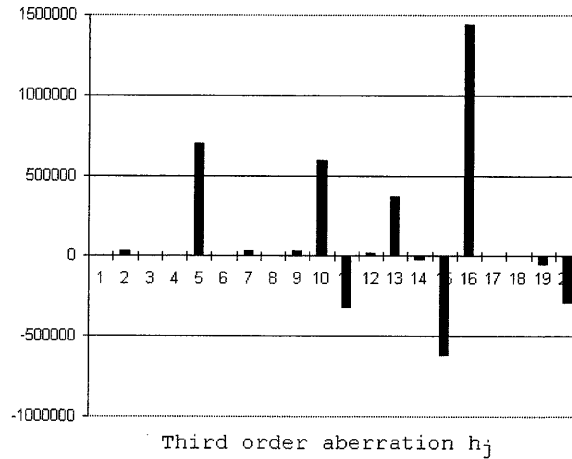


Figure 5.3: The third-order Hamilton coefficients in the horizontal plane as calculated with COSY INFINITY for a specific optic of the accelerator ring with all sextupoles (MXL1, MXL2, MXL3, MXL4, MXL10, MXL11, MXL12, MXL13, MXL, MXG, XMS) excited at 50% of their maximal strengths.

For the excitation of the beam, the steerers SH01, SH03, SV02 and SV04 are used and the orbit is calculated at BPM01. The orbit excitation is for all steerers equal and 1 mrad. The excitation frequencies are: 100 Hz at SH01, 110 Hz at SH03, 125 Hz at SV02 and 175 Hz at SV04. Here, the matrix $c_{\alpha jm}$ is calculated and the orbit response written in a file of 8192 datapoints corresponding to a period of 8.192 seconds. Because of the 2^{13} datapoints, this data can be used for a Fast-Fourier-Transformation. We clearly observe the excitation frequencies at the BPM01 with amplitudes of about 2 mm. In the corresponding FFT-spectra these frequencies are visible as large peaks with a certain width as shown in figure 5.4 for the horizontal plane and in figure 5.5 for the vertical plane. In the horizontal plane the 100 Hz and 110 Hz peaks of the horizontal steerers are visible. The same spectrum can be analysed at BPM01 in the vertical plane. This FFT-spectrum is shown in figure 5.5. In this figure we see the two vertical excitations at 125 Hz and 175 Hz. Due to coupling between the horizontal and vertical plane, the horizontal excitation frequencies are also visible. Also a second harmonic term at 350 Hz is visible.

The resulting Fourier-coefficients were then used to determine the amplitude and phase of the signal which was calculated at the position of BPM01. Because of the finite number of turns the peaks have a certain width.

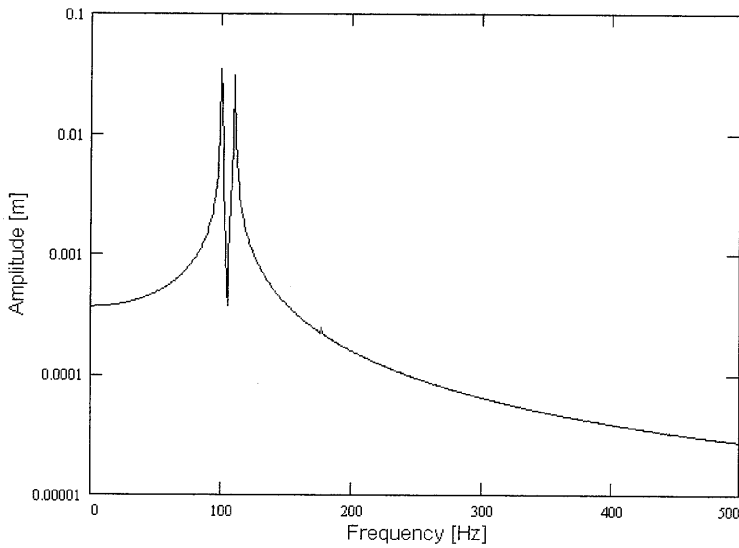


Figure 5.4: *The FFT-spectrum of the beam response at BPM01 in the horizontal plane without sextupole excitation. The excitation frequencies in the horizontal plane are visible as two peaks at 100 Hz and 110 Hz.*

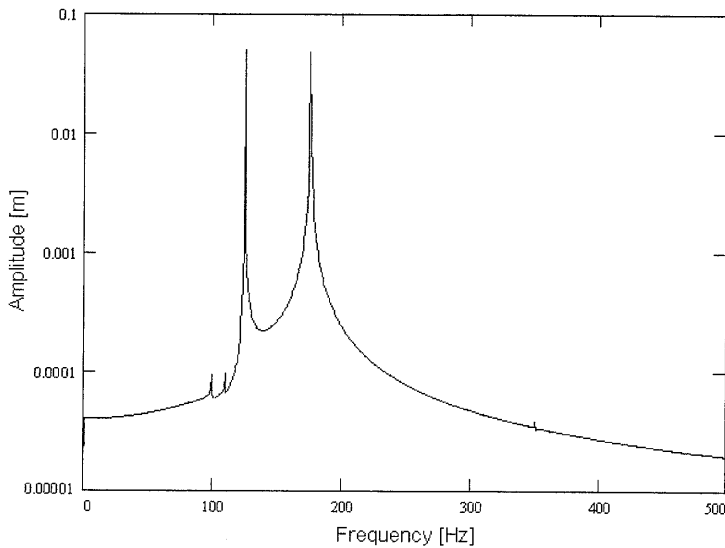


Figure 5.5: *The FFT-spectrum of the beam response at BPM01 in the vertical plane without sextupole excitation. The excitation frequencies in the vertical plane are visible as two peaks at 125 Hz and 175 Hz.*

If all sextupoles are turned off, the amplitude of the mixing frequencies become very small. The signals of the mixing frequencies are weaker than the signals of the excitation frequencies and therefore are more difficult to see. To remove the excitation frequencies from the FFT-spectrum, a digital notch-filter is constructed. This filter allows us to remove these specific frequencies. They are exactly known, so the notch-filter consists of a file with the exact same length as the datafile with the orbit response containing the excitation frequencies with the right amplitude and without mixing frequencies. The result of these calculations are shown in the following figures. First of all, the beam response is shown without excitation of any sextupoles in the ring in the horizontal (figure 5.6) and vertical plane (figure 5.7).

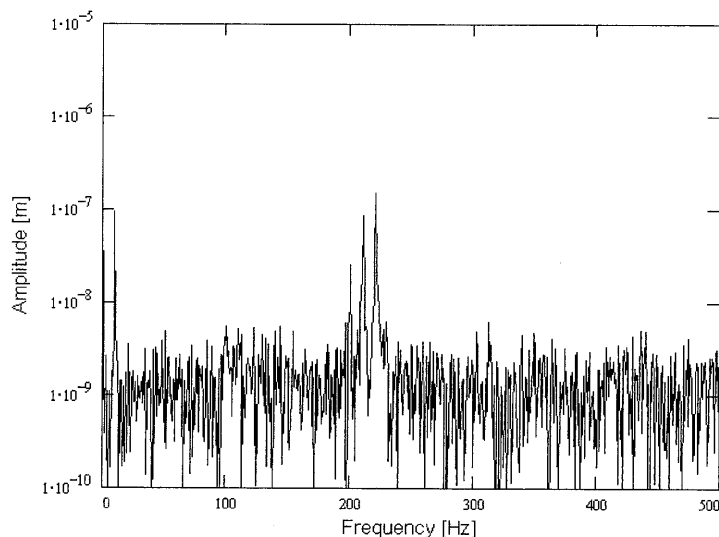


Figure 5.6: *The FFT-spectrum of the beam response at BPM01 in the horizontal plane without exciting sextupoles after the excitation frequencies were removed from the spectrum.*

In the horizontal plane four small peaks are visible that suggest a small non-linear contribution with frequencies of about 10, 200, 210 Hz and 220 Hz. These frequencies correspond to the mixing frequencies $f_1 - f_2$, $2f_1$, $f_1 + f_2$ and $2f_2$. In the vertical plane, we see some more resonance frequencies. About 10 frequencies are visible in this spectrum and the largest amplitudes belong to the frequencies $2f_4$ and $f_4 - f_3$.

We now show some calculations in which all sextupoles (MXL1, MXL2, MXL3, MXL4, MXL10, MXL11, MXL12, MXL13, MXL, MXG, MXS) are excited at 50% of their maximal strength. In these spectra we see all 17 response frequencies with the calculated amplitude at the horizontal BPM01. In figure 5.8 and figure 5.9 the horizontal, respectively the vertical response is shown.

In the horizontal and vertical plane, the small dips at the position of the filtered

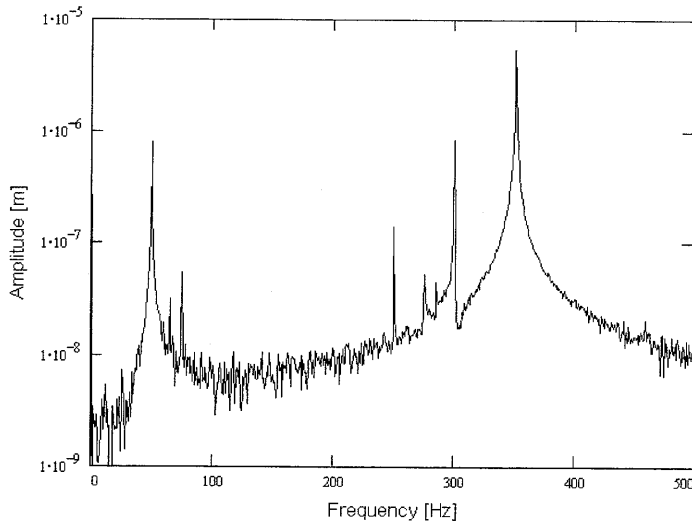


Figure 5.7: *The FFT-spectrum of the beam response at BPM01 in the vertical plane without exciting sextupoles after the excitation frequencies were removed from the spectrum.*

frequencies are visible. Furthermore, in the horizontal and vertical plane all mixing frequencies and their amplitudes are shown. The signals measured in the vertical plane are larger than the ones in the horizontal plane. The same calculations can be done using different steerers and other BPM's yielding similar results.

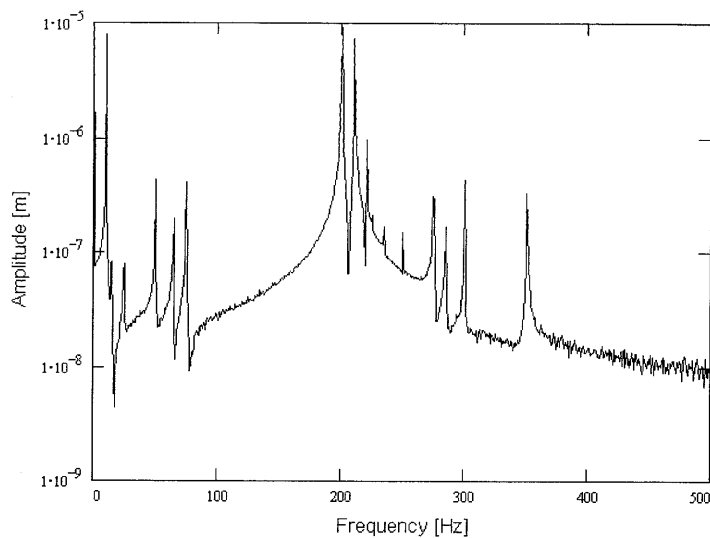


Figure 5.8: *The FFT-spectrum of the beam response at BPM01 in the horizontal plane with excitation of all sextupoles at 50% after the excitation frequencies were removed from the spectrum.*

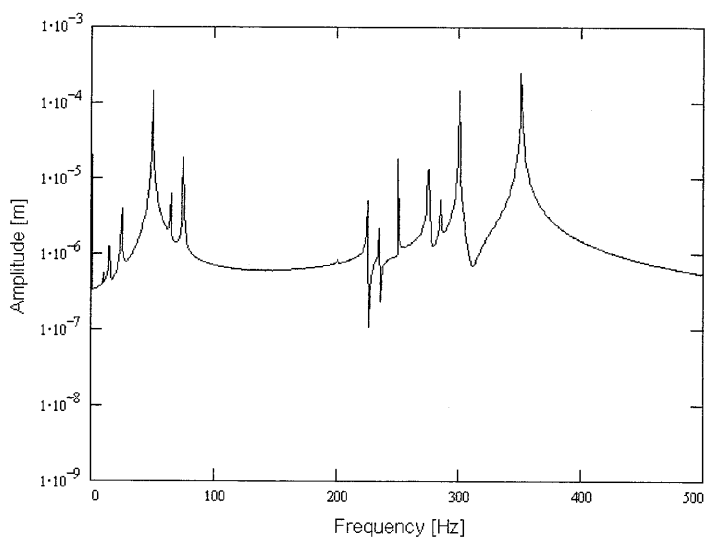


Figure 5.9: *The FFT-spectrum of the beam response at BPM01 in the vertical plane with excitation of all sextupoles at 50% after the excitation frequencies were removed from the spectrum.*

5.7 Wobbling measurements

5.7.1 Introduction

For the excitation of the beam two horizontal and two vertical correctors are needed. The experimental setup at COSY is as follows: the power supplies of the four steerer magnets are connected to frequency generators. Each power supply is a current source. The frequency and amplitude of each individual input signal can be varied. The frequency range is between 0-300 Hz and the amplitude of the steerer excitation depends on the self induction of the magnets. At higher excitation the power supply is reaching its maximal output voltage. In figure 5.10 the limitations of the power supply at higher frequencies is shown.

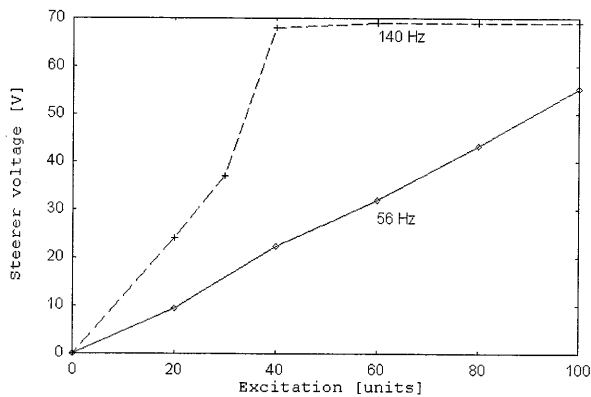


Figure 5.10: Steerer amplitude calibration as function of the applied frequency. The first measurement is at 56 Hz (solid line). At 140 Hz (dashed line) the limitation of the power supply at higher excitations is shown.

The power supply is capable to change the current with a velocity of $di/dt=120$ A/s. Therefore, larger amplitudes are not possible. When the maximal amplitude is reached, higher-order frequencies are present in the amplified signal. They become dominantly strong when the excitation amplitude is increased further. Although the maximal amplitude given to the steerer magnets can not be increased, the non-linear excitation grows as function of the excitation amplitude.

For the measurements SH01, SH03 are the used horizontal steerer magnets. In the vertical plane the steerer magnets SV04 and SV06 are used. The response of the closed orbit to the steerer excitation is measured with a spectrum analyser at different BPM's. As shown in the previous section, the BPM's between the last steerer magnet and the non-linear distortion can be used for measuring the orbit response. The analogue signals of the BPM's can be monitored with an inaccuracy of 2.3 Hz due to the resolution. The signal contains background noise which is reduced by averaging about twenty-five different measurements. Because the amplitude of the steerer is small at high energies the measurements are done at injection energy.

The non-linear coefficients are best visible when the closed orbit deviations are small. For this reason the closed orbit deviations are compensated. To get good results, the beam should be electron cooled. However, experiments show that electron cooling solenoids cause large coupling effects that strongly influence the results. Therefore, electron cooling was not used for the measurements presented here.

5.7.2 Unperturbed measurement with steerer magnets

In this paragraph the measured response at a BPM is presented in the horizontal and vertical plane without excitation of sextupole magnets. In the response signal, see figure 5.11, a centre frequency is visible. This frequency shows the revolution frequency of the circulating beam, at injection energy this is about 489 kHz. In figure 5.11 the dashed line indicates a measurement without steerer magnets, the solid line is a measurement with the horizontal and vertical steerer magnets (SH01=56 Hz SH03=107 Hz, SV04=131 Hz and SV06=140 Hz corresponding with f_1 , f_2 , f_3 and f_4) in the horizontal plane. We see in the spectra frequency peaks at 200 Hz and 300 Hz with respect to the centre frequency which are noise peaks due to power supply ripple. The steerer excitations occur as small peaks symmetrical around the revolution frequency. The excitation frequencies were chosen to ensure that all sum and difference frequencies do not coincide with each other and the distance between the peaks is as large as possible. The vertical steerer signals are not visible, but a peak at 216 Hz indicate $2f_2$ is present in the signal. Calculations show that the peak at 216 Hz is naturally excited in the accelerator with these settings.

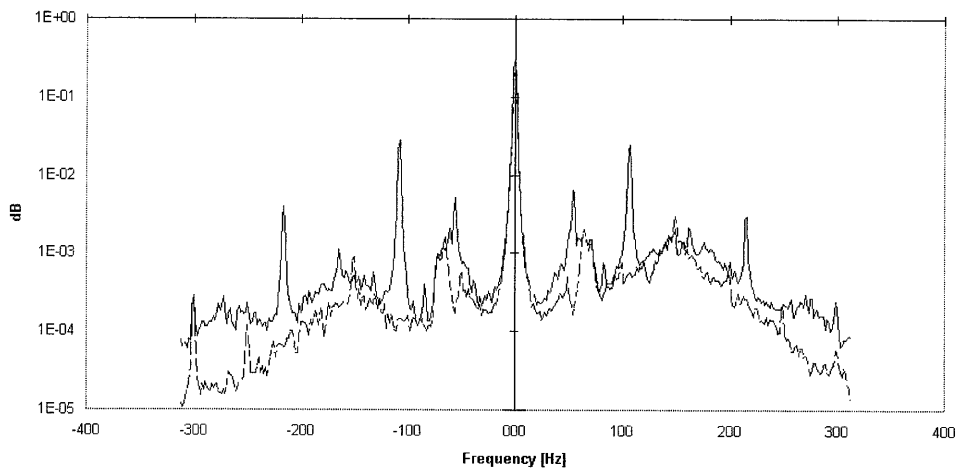


Figure 5.11: Measured horizontal orbit response at 295 MeV/c without steerer excitation (dashed line) and without sextupole excitation. Measured orbit response to steerer excitation at 56, 107 Hz horizontally and 131, 140 Hz vertically (solid line). The frequency of the circulating beam is 488.9 kHz (centre of graph).

In figure 5.12 the measured vertical orbit response spectrum is presented in

which the revolution frequency is again in the middle. Also the noise peaks of 250 Hz and 300 Hz are also visible (measurement without steerer magnets: dashed line). In figure 5.12 the vertical steerer peaks of 131 Hz and 140 Hz are visible and peaks between 200 and 300 Hz (indicated with solid line). Due to the low resolution of this spectrum the two peaks are not completely separated.

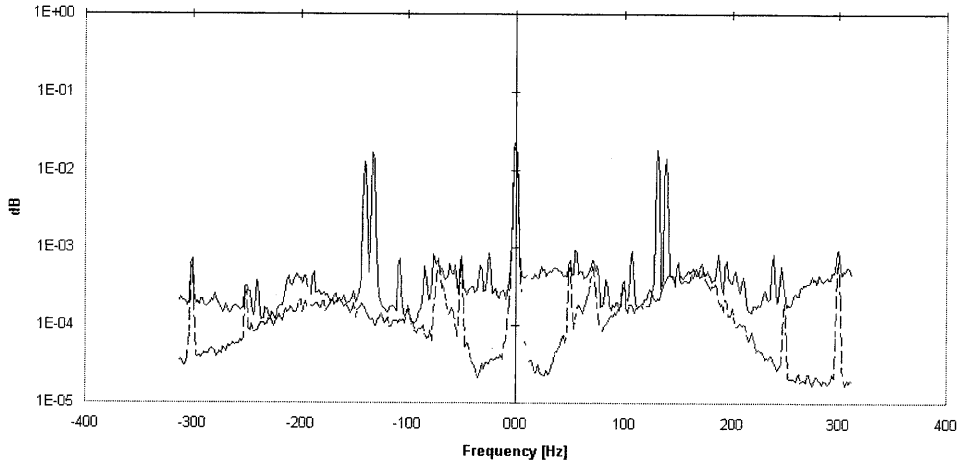


Figure 5.12: Measured vertical orbit response at 295 MeV/c without steerer excitation (dashed line) and without sextupole excitation. Measured orbit response to steerer excitation at 56, 107 Hz horizontally and 131, 140 Hz vertically (solid line). The frequency of the circulating beam is 488.9 kHz (centre of graph).

5.7.3 Evaluation of data

The measured spectra contain noise and artefacts. Artefacts are measured signals that are not excited by the four steerer magnets. For example, due to power supply ripple additional peaks are present in the measured beam response. The noise can only be reduced by averaging the measured spectra. The artefacts can only be reduced by another method. Two frequency spectra are measured, one with and the other without wobbling. After these spectra are subtracted from each other the resulting curve shows that some peaks are not present anymore. For example, the 250 Hz and 300 Hz power supply ripple are not visible anymore.

The influence of a non-linearity on the beam is investigated. Because the mixing frequencies are not visible in the spectrum an additional non-linearity is introduced. For this purpose, a sextupole is switched on (typically MXL13). To remove the artefacts from the measured spectra four different spectra are measured. First a spectrum without using steerer magnets is measured. Then a spectrum with wobbling steerers is measured. The same is repeated with the sextupole on. For the noise reduction each spectrum is measured 25 times. In figure 5.13 the resulting

curves are shown. Here, BPM09H is used for measuring the horizontal spectrum and BPM17V for the vertical spectrum. Sextupole MXL13 is powered at 7% of its

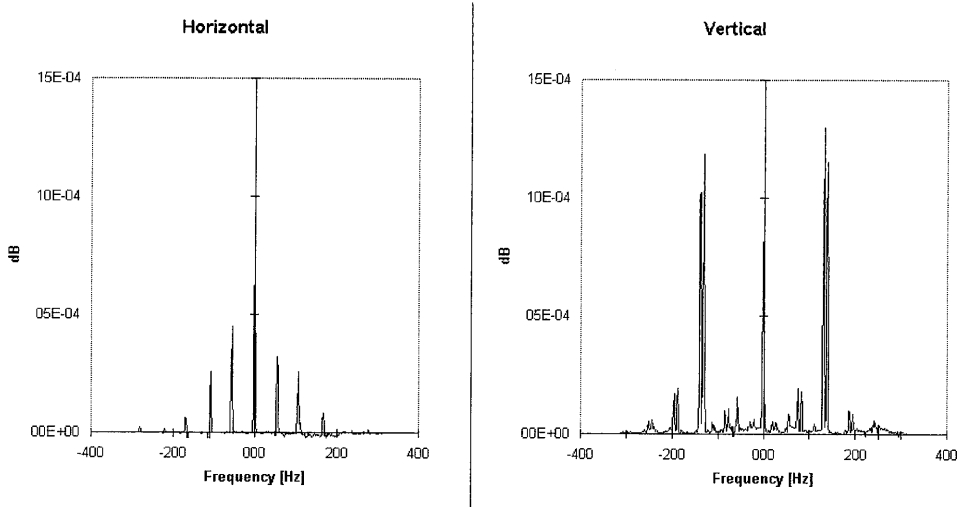


Figure 5.13: Measured horizontal and vertical frequency spectrum. The difference between a measurement with and without sextupole excitation (with MXL13) is plotted.

maximal current. In both spectra the excitation frequencies are visible (56 Hz and 107 Hz in the horizontal plane and 131 Hz and 140 Hz in the vertical plane). Some additional smaller peaks are seen in both spectra. These are the expected additional difference and sum frequencies. In this example the following frequencies are visible: 167 Hz ($f_1 + f_2$), 220 Hz ($2f_2$) and 280 Hz ($2f_4$) in the horizontal spectrum. In the vertical spectrum the measured frequencies of 22 Hz ($f_3 - f_2$), 31 Hz ($f_4 - f_2$), 188 Hz ($f_1 + f_3$), 195 Hz ($f_1 + f_4$) and 244 Hz ($f_2 + f_4$) are present.

The next step is to study the influence non-linear elements (sextupoles) in the ring in more detail. The non-linear terms are influenced by the position of the particles in the sextupole because the non-linear terms are dependent on x^2 , z^2 , $x'x$, xz and so on. The measurement shown above is repeated for several BPM's and the frequencies due to non-linear magnetic fields are searched for and the results are presented in table 5.1.

In the horizontal plane we expect to detect signals of $f_3 - f_4$, $f_1 - f_2$, $2f_1$, $f_1 + f_2$, $2f_2$, $2f_3$, $f_3 + f_4$ and $2f_4$. In the vertical plane we expect to see peaks of $f_2 - f_3$, $f_2 - f_4$, $f_1 - f_3$, $f_1 - f_4$, $f_1 + f_3$, $f_1 + f_4$, $f_2 + f_3$ and $f_2 + f_4$. This can be checked when the Hamiltonian in the case of a normal sextupole is investigated. In Eq. 5.35 only terms of x^2 , $x'x$, x'^2 , z^2 , $z'z$ and z'^2 are present in the horizontal plane. In the vertical plane only terms of xz , $x'z'$, xz' and $x'z'$ are excited in the transverse direction, see Eq. 5.36.

In the table, a cross (\times) is shown when a peak at that frequency is measured.

Frequency [Hz]	Frequency	BPM07H	BPM13H	BPM17V	BPM24V
9	$f_3 - f_4$.	.		
24	$f_2 - f_3$			×	×
33	$f_2 - f_4$			×	×
51	$f_1 - f_2$.	.		
75	$f_1 - f_3$		<u>×</u>	×	×
84	$f_1 - f_4$			×	×
112	$2f_1$.	.		
163	$f_1 + f_2$	×	×		
187	$f_1 + f_3$			×	×
196	$f_1 + f_4$			×	×
214	$2f_2$	×	×	<u>×</u>	<u>×</u>
238	$f_2 + f_3$			×	×
247	$f_2 + f_4$			×	×
262	$2f_3$.	.		
271	$f_3 + f_4$	×	.		
280	$2f_4$	×	×		

Table 5.1: *Mixing frequencies induced with sextupole $MXL13=-2\%$. Crosses indicate measured frequencies, underlined crosses indicate measured frequencies that are not predicted, dots indicate frequencies that were not observable in the measured response.*

In the vertical plane all peaks are present, in the horizontal plane not all could be measured. The dots (·) indicate peaks that should be present in the measured response. The underlined crosses (×) are measured and not expected. Theoretical predictions indicate that these peaks can not be generated by skew sextupoles or solenoid fields because they would strongly influence other peaks also. Studies of the power supply of the steerer magnets show that these frequencies may be excited through higher harmonics of the sin waveform that are supplied to the magnets.

5.7.4 Amplitude dependence of non-linear terms

The theoretical calculations show that the amplitude belonging to the mixing frequencies depends on the size of the kick by the steerer. Furthermore, the amplitude belonging to the mixing frequencies depends on the amplitude of the sextupole strength. In the following sections measurements are presented in which the influence of the steerer excitation and of the sextupole excitation are changed. In Eq. 5.48 it is shown that the linear increase of the sextupole strength yields a linear increase of the amplitude belonging to the mixing frequencies. This amplitude increases quadratically when the kick of the steerer magnets is increased linearly. To verify this result measurements are done and presented here.

First, measurements in which the amplitude of the excitation frequency is varied are shown. Secondly, measurements are shown in which the amplitude of the non-

linear excitation is altered. The experimental setup is as following: the frequency spectrum with a frequency range of $f_0 \pm 325$ Hz, with f_0 the revolution frequency, is measured at several BPM's (the sextupole magnets are off). Then the frequency spectrum is measured with the four steerer signals on. Both measurements are repeated with the sextupole magnet on. This yields the peaks due to the nonlinearities at one BPM for one setting of the steerer magnets and the sextupole setting. Either the sextupole strength is changed or the steerer excitation of all four steerers is increased or decreased. The measurement of one datapoint is time-consuming. Therefore, the typical number of datapoints in a figure is about 4 for each individual frequency. The error of the measured peaks is about 5 %. This error is so large because the peaks are determined out of the composition of 4 measured spectra. The noise from each spectrum gives an additional error on the peak-size.

Mixing frequencies response as function of steerer magnets

In this section the excitation of the steerer magnets is varied. For this purpose, the four steerer magnets are powered in three different modes. In table 5.2 the three modes are presented and the output of the frequency generator for each individual steerer is given. The excitations for the individual steerer magnets are different for the four frequencies. This is explained in the previous section.

Steerer:	Mode 1	Mode 2	Mode 3
SH01 (f_1)	23	31	39
SH03 (f_2)	44	58	73
SV04 (f_3)	53	71	89
SV06 (f_4)	60	80	100

Table 5.2: *Steerer excitation of the four steerer magnets at different experiments.*

The steerer magnets excitation is given in arbitrary units and the calibration to the amplified voltage to the steerer is given in figure 5.10. Because of the large number of peaks, only a few frequencies are presented here. First of all, the amplitude belonging to the frequencies $f_1 + f_4$ and $f_1 - f_4$ at BPM07V is shown in figure 5.14 and 5.15, respectively.

In the figures in this section the horizontal axis only shows the amplitude of steerer SH01 (mode 1: 23, mode 2: 31, mode 3: 39). To determine the excitation amplitude of the other steerer magnets table 5.2 is needed.

The same result is obtained when, for example, another BPM is used. For this purpose, the data measured with BPM09V are presented in figure 5.16 and 5.17.

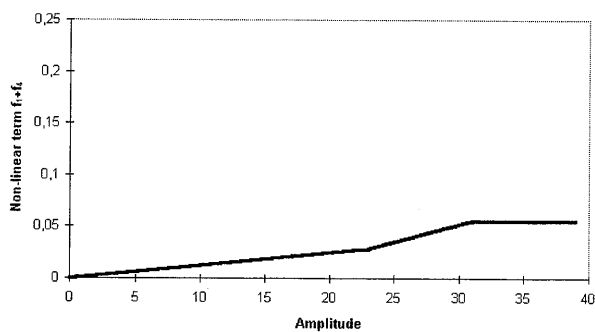


Figure 5.14: Measured vertical frequency of $f_1 + f_4$ at BPM07V as function of the excitation frequency of the steerer magnets. The sextupole MXL12=2% and MXL13=2%.

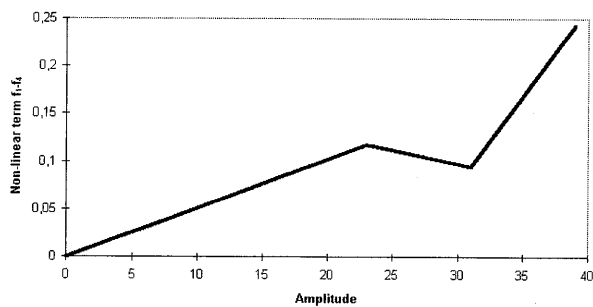


Figure 5.15: Measured vertical frequency of $f_1 - f_4$ at BPM07V as function of the excitation frequency of the steerer magnets. The sextupole MXL12=2% and MXL13=2%.

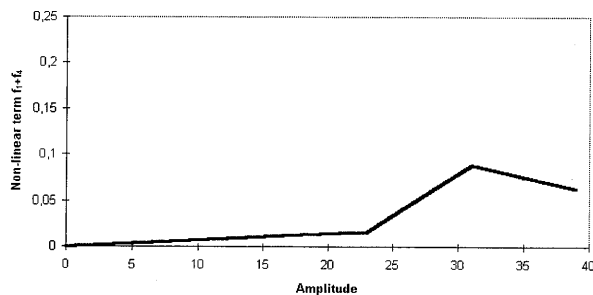


Figure 5.16: Measured vertical frequency of $f_1 + f_4$ at BPM09V as function of the excitation frequency of the steerer magnets. The sextupole MXL12=2% and MXL13=2%.

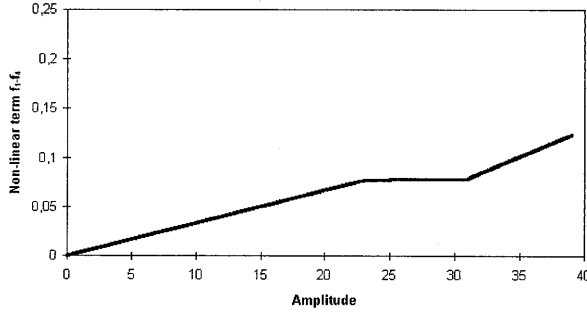


Figure 5.17: Measured vertical frequency of $f_1 - f_4$ at BPM09V as function of the excitation frequency of the steerer magnets. The sextupole MXL12=2% and MXL13=2%.

The amplitude of the response roughly increases linearly as function of the steerer amplitude. The induced field in steerer SV06 (f_4) is in saturation and does not change in the region. The amplitude change is only dependent of the change in steerer SH01 (f_1) and therefore $f_1 + f_4$ and $f_1 - f_4$ only depend on f_1 . The result is that only a linear increase is expected. The size of the mixing frequency is almost the same at the two different BPM's. Furthermore, the amplitude of the peak $f_1 + f_4$ (84 Hz) is the same as $f_1 - f_4$ (196 Hz). This is expected when we look at Eq. 5.48. Both $\cos(\omega_i - \omega_j)t$ and $\cos(\omega_i + \omega_j)t$ have the same amplitude. A numerical calculation of the amplitude of the mixing frequency $f_1 + f_4$ yields 0.3 (for both BPM's) for the third mode of the four steerer magnets. The numerical calculations give a reasonable indication for the measured size of the mixing frequency.

In figure 5.18 and 5.19 the expected quadratic increase of the frequency response as function of the excitation is seen. The amplitude is dependent on the excitation of both steerers (f_1 and f_2). Therefore, the measured curve in figure 5.19 increases quadratically. In figure 5.18 the amplitude depends only on f_2 . In Eq. 5.48 the term $\cos 2\omega_j t$ is responsible for the increase of the non-linearity. The frequency of the steerer is smaller and the point of saturation is at higher amplitudes, that were not used here to avoid beam losses. In these figures the measured signals at BPM22H are shown. Numerical calculations yield an amplitude of 0.1 for $2f_2$ and 0.6 for $f_1 + f_2$ when mode 3 of the steerer magnets is chosen (see table 5.2).

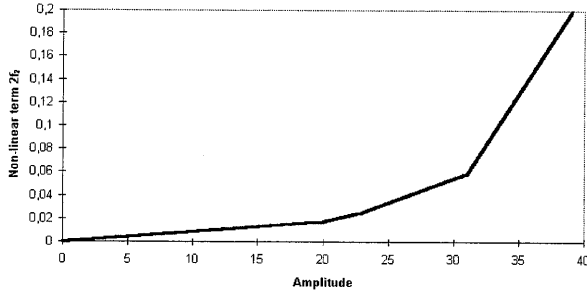


Figure 5.18: Measured horizontal frequency of $2f_2$ at BPM22H as function of the amplitude of the excitation frequency of the steerer magnets. The sextupole $MXL12=2\%$ and $MXL13=2\%$.

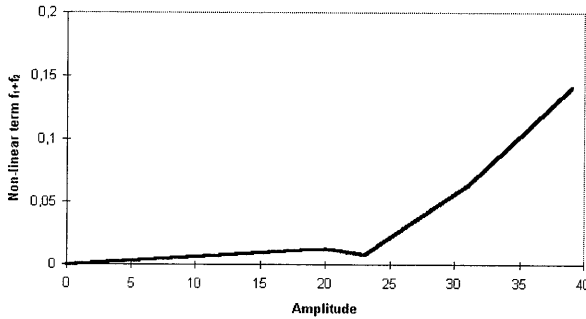


Figure 5.19: Measured horizontal frequency of $f_1 + f_2$ at BPM22H as function of the amplitude of the excitation frequency of the steerer magnets. The sextupole $MXL12=2\%$ and $MXL13=2\%$.

Mixing frequencies response as function of the sextupole strength

After the investigation of the dependence of the amplitude of the mixing frequencies, now the dependence on the sextupole strength is investigated. Therefore, the steerer excitation is kept constant. The excitation of SH01, SH03, SV04 and SV06 is the same as the setting of mode 3 in table 5.2. The sextupole excitation is varied to measure the influence of the non-linear magnetic field. The amplitude is varied for both sextupoles to be 1 % (-1 %), 2 % (-2 %), 3 % (-3 %) and 4 % (-4 %) for MXL12 (MXL13). The amplitude of one mixing frequency in the spectrum is shown as function of the sextupole strength. A few BPM's are chosen for the measuring of the frequency spectra. Again, only a few figures are shown to give an indication of the results. For the sextupole excitation MXL12 and MXL13 are used.

In figure 5.20 the response of the frequency $f_3 + f_4$ (271 Hz) at BPM08H is shown. At the highest amplitude a measurement error in the signal is visible.

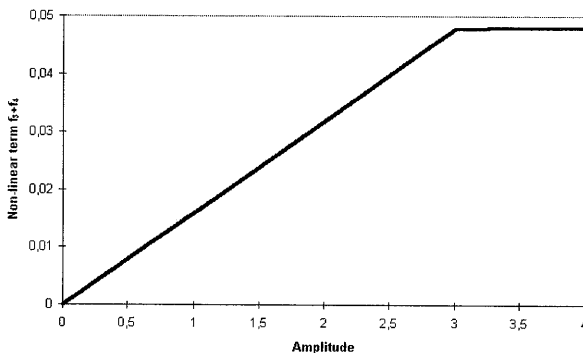


Figure 5.20: Measured frequency $f_3 + f_4$ at BPM08H as function of the amplitude of the sextupole strength of MXL12 and MXL13.

The same frequency is measured with BPM13H, see figure 5.21. Again a measurement error is visible at the highest excitation of the sextupoles.

In figure 5.22 the frequency response of the frequency $f_2 + f_3$ (238 Hz) at BPM07V is presented. The measurement shows an increase in the beam response when the sextupole strength is increased.

Other measurements show a large error when the measurements are repeated. It is difficult to determine the sextupole dependent behavior from this type of measurements. A reason could be the non-linear excitation of the steerer magnets. They excite the beam with a multiple of the excitation frequency. In the case of SH01, the excitation is 56 Hz. When the excitation is non-linear, the beam is also excited with frequencies of $n \cdot 56$ Hz. These can change the amplitude of the non-linear frequencies. In figure 5.23 the response of the frequency $f_1 + f_3$ at BPM17V is shown. The expected linear dependence on the sextupole strength is shown. The expected values for the sextupole strength (4 %) in figure 5.20 ... 5.23 for the amplitude belonging to the non-linear frequency are 0.1, 0.1, 0.22 and 0.01, respectively.

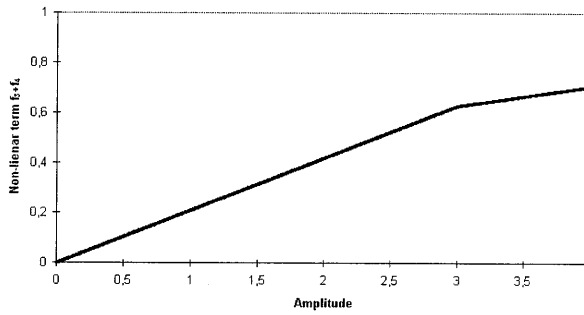


Figure 5.21: Measured frequency $f_3 + f_4$ at BPM13H as function of the sextupole strength of MXL12 and MXL13.

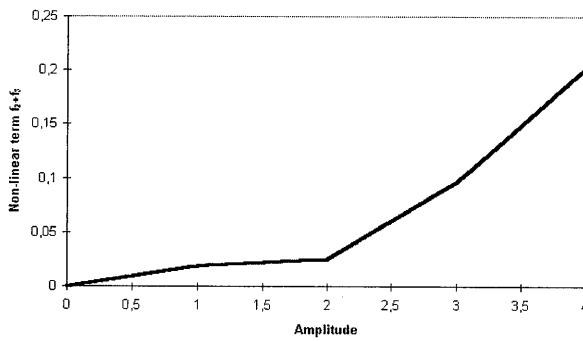


Figure 5.22: Measured frequency $f_2 + f_3$ at BPM07V as function of the sextupole strength of MXL12 and MXL13.

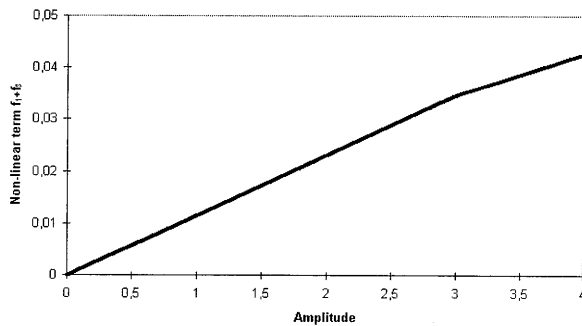


Figure 5.23: Measured frequency $f_1 + f_3$ at BPM17V as function of the sextupole strength of MXL12 and MXL13.

The calculations show that it is possible to estimate the amplitude of the mixing frequencies. The measurements were repeated with other BPM's and using other sextupoles. Comparison with numerical results obtained from calculations with the code COSY INFINITY shows that some results are roughly in agreement with the measured results. However, the measurements are not accurate due to the large errors.

5.7.5 Measurement errors

Measurements have been presented of the amplitudes of the mixing frequencies due to the non-linear magnetic fields. The amplitude of the peaks has been measured as function of the amplitude of the excitation. Also measurements in which the sextupole strength has been varied were shown. All measurements resulted in considerable errors for the measured values of the frequency amplitudes. The method can be useful to determine the effect of sextupole magnets on the beam properties. Numerical calculations give an indication of the amplitude of the measured peaks.

It is very difficult to determine the peaks in the spectrum. First of all, due to noise and artefacts in the measurement the amplitude of the peak can not accurately be measured. With averaging and subtracting measured spectra these errors were reduced. However, the amplitude of the excitation frequencies are small and therefore the beam response is difficult to measure. The amplitude is limited because of the power supplies. Due to saturation effects higher harmonics can be produced in the signals.

Furthermore, for each measurement a new bunch is injected in the accelerator. This results in a slightly different beam, which yields small errors. The measurements are performed at injection energy. The beam is kicked with an amplitude that is proportional to $1/B\rho$ and is therefore smaller at higher energies. At injection the acceptance of the beam pipe is completely used. The BPM's measure the beam centroid displacements which yields errors when the transverse beam size is large.

However, the detection can be better. This can be achieved by improving the steerer excitations. With other power supplies the amplitude can be increased to give larger amplitudes to the beam and the higher harmonics of the excitations should be reduced. The detection of the signals can be increased by using a spectrum analyser with a higher resolution.

Comparison with numerical results obtained from calculations with the code COSY INFINITY shows that the results are roughly in agreement with the measured results. This indicates that further development of the method presented here is useful.

Bibliography

- [1] A.J. Dragt, *Lectures on non-linear orbit dynamics*, AIP conference proc. **87** (1982) p.147.
- [2] A.J. Dragt and J.M. Finn, *Lie series and invariant functions for analytic symplectic maps*, Jour. of Math. Phys. **17** (1976) p.2215.
- [3] L.H.A. Leunissen, *Linear and non-linear effects on the electron optical trajectories of the race-track microtron Eindhoven*, Master's thesis, VDF/NK 94-34, Eindhoven University of Technology, The Netherlands (1994).
- [4] V. Ziemann, *Identification of Third-order Hamiltonian Coefficients from Forced Coherent Beam Oscillations*, CERN SL/95-94(AP) (1995).

Chapter 6

Conclusions

In this thesis the proton Cooler Synchrotron COSY is described. It consists of a cyclotron in which H^- particles are accelerated upto 45 MeV. After stripping injection the protons are accelerated to energies between 0.175 GeV and 2.5 GeV in the synchrotron. A theoretical and numerical study of the linear and non-linear transverse beam dynamics is carried out.

The extensive first-order study of beam properties in the synchrotron results in calibration factors for several elements in the ring. For this purpose a fitting procedure is introduced and used for measurements. First of all, the calibration factors of the steerer magnets are known for energies between 0.175 GeV and 2.5 GeV. It is shown that the calibration factor of the steerer magnets in the straight sections show a small energy dependence. In the arcs the energy dependence is much larger. The closed orbit deviation can be compensated with steerer magnets. This results in a closed orbit control in the mentioned energy range. The closed orbit deviations are reduced to values with a rms-value of about 1.5 mm. Secondly, the BPM scaling factors are determined and yield deviations from the ideal values which are smaller then 20 %. The fitted magnetic field errors of the quadrupoles are smaller then 0.8 %. The magnetic field errors of the quadrupoles are caused by fabrication inaccuracies and changes in the fringing field. The fringing field of a quadrupole is changed when an other magnet is placed in its vicinity. This shielding results in a change of the effective length of the quadrupole. Numerical calculations with the code MAFIA have shown that this effect is responsible for the magnetic field errors in the quadrupoles. The change in effective length is in agreement with the measurements from the fit-procedure. Also an experimental setup in which a quadrupole and steerer were positioned near each other yields approximately the same result as obtained from calculation.

Attention is paid to the misalignment of dipole magnets and quadrupole magnets on the particle trajectory. This results in a description of the closed orbit deviation from the reference trajectory. Measurements are in good agreement with the calculated closed orbit deviations.

Magnetic field measurements of the dipole magnets yields the transverse mag-

netic field distribution in the median plane. Numerical calculations show the influence on the transverse motion of the protons. First-order magnetic field errors result in a betatron tune-shift that depends on the closed orbit deviation in the dipole magnets. The second-order magnetic field error results in additional sextupoles in the ring. The first- and second-order components become larger with higher energies. Measurements show the expected betatron tune-shift due to the first-order magnetic field errors. The sextupole component in the dipole magnets is experimentally observed.

Hamilton mechanics is used to set up a general theory that describes the influence of coupling terms and resonances on the particle trajectory. After canonical transformations Hamilton equations are obtained that describe individual resonances. For example, the Hamiltonian for non-linear particle motion near the third-order resonance conditions has been deduced. First, a coupling resonance is investigated experimentally. Poincaré maps in the resonant rotation frame for the particle motion are obtained from the measurement as well as the linear coupling strength. The measured coupling strength is in agreement with the calculated coupling strength. Secondly, motion in the horizontal plane is measured for the betatron tune near the third-order resonance. Measurements show the influence of non-linear magnetic fields. The motion near the third-order resonance can result in resonance islands in which the beam is "locked". The islands are observed and numerical calculations with the code SIXTRACK yields the exact position and width of the three islands.

The non-linear equations of motion can be solved using Lie algebraic tools. This theory is applied to the equations of motion upto second-order. Two horizontal and two vertical steerer magnets are used to excite the beam with sinusoidal signals at four different frequencies. The response of the beam is measured with BPM's. The calibration of the excitation of the steerer magnets show that the power supplies are not capable to excite the beam to large amplitudes. Errors in the excitation signals result in measurement inaccuracies. Because the amplitude of the response signals are small they are difficult to determine. However, measurements show that it is possible to detect peaks due to non-linear effects in the beam response. The amplitude of signals with mixing frequencies is determined with fixed sextupole strength and fixed excitation of the steerer magnets. The amplitude of the signals with mixing frequencies due to the applied sextupole strength is measured. These measurements show a linear increase of the non-linear beam response as function of the sextupole strength. Then measurements were carried out in which the sextupole strength is fixed. Variation of the excitation strength of the steerers show a quadratic dependence on the amplitude of the signals containing mixing frequencies. Numerical calculations with COSY INFINITY yield information on the size of the third-order Hamilton coefficients. The results of the calculation give a good indication for the measured results. The presented method can be used for the measurement of third-order Hamilton coefficients.

Appendix

Position of the elements in the accelerator ring. The origin is set at the beginning of the target telescope (near the injection of the particles in the ring). The centre of the elements is given in the table.

Position [m]	Name element	Position [m]	Name element
4.86	MQT 1	23.95	MQT 11
5.29	BPM 02H	24.38	BPM 06H
5.45	BPM 02V	24.53	BPM 06V
5.86	MQT 2	24.95	MQT 12
6.72	MQT 3	25.49	SH 05
7.22	MXL 01	25.76	SV 06
7.72	MQT 4	27.18	TP2
8.22	SH 01	29.64	BPM 07H
8.52	SV 02	29.78	BPM 07V
10.65	BPM 03H	31.23	SV 08
10.80	BPM 03V	31.50	SH 07
12.29	WCM	32.03	MQT 13
13.99	SV 04	32.53	MXL 04
14.26	SH 03	33.03	MQT 14
14.79	MQT 5	33.89	MQT 15
15.22	BPM 04H	34.32	BPM 08H
15.37	BPM 04V	34.46	BPM 08V
15.79	MQT 6	34.89	MQT 16
16.65	MQT 7	40.66	SH 09
17.16	MXL 02	40.93	BPM 09H
17.65	MQT 8	41.09	BPM 09V
19.20	BPM 05H	41.37	MQU 1
19.35	BPM 05V	42.91	dipole 1
19.60	TP1	43.98	BPM 10H
22.09	MQT 9	44.14	BPM 10V
22.59	MXL 03	44.45	MQU 2
23.09	MQT 10	44.75	SV 10

Position [m]	Name element	Position [m]	Name element
45.99	dipole 2	86.69	SH 19
48.48	fast quadrupole 1	87.03	MQU 11
50.83	dipole 3	87.33	BPM 16V
52.03	SH 11	87.50	BPM 16H
52.37	MQU 3	88.57	dipole 12
52.69	MXL 05	90.11	MQU 12
53.91	dipole 4	90.38	BPM 17V
54.97	BPM 11H	90.53	BPM 17H
55.13	BPM 11V	90.80	SV 20
55.45	MQU 4	94.59	MQT 17
56.14	SV 12	95.02	BPM 18H
56.98	fast quadrupole 2	95.17	BPM 18V
58.32	MXL 06	95.59	MQT 18
58.70	MQU 5	96.02	scraper 1XX
59.02	SH 13	96.45	MQT 19
60.24	dipole 5	96.96	MXL 10
61.30	BPM 12H	97.45	MQT 20
61.47	BPM 12V	97.98	SH 21
61.78	MQU 6	98.25	SV 22
62.09	SV 14	100.25	CAVITY
63.32	dipole 6	102.65	BCT
64.69	MXL 07	103.75	SV 24
68.16	dipole 7	104.02	SH 23
69.21	BPM 13H	104.53	MQT 21
69.38	BPM 13V	104.95	BPM 19H
69.70	MQU 7	105.10	BPM 19V
70.25	TP3	105.53	MQT 22
71.24	dipole 8	105.95	scraper 2YY
72.32	BPM 14H	106.39	MQT 23
72.78	MQU 8	106.89	MXL 11
73.16	MXL 08	107.39	MQT 24
73.46	SH 16	110.88	BPM EC1H
75.66	SH 17	110.89	BPM EC1V
76.03	MQU 9	111.61	ECOOL
76.34	BPM 15V	112.33	BPM EC2H
76.50	BPM 15H	112.34	BPM EC2V
77.57	dipole 9	115.83	MQT 25
78.80	MXL 09	116.32	MXL 12
79.11	MQU 10	116.83	MQT 26
79.42	SV 18	117.25	scraper 3X
80.66	dipole 10	117.69	MQT 27
85.49	dipole 11	118.11	BPM 20H

Position [m]	Name element	Position [m]	Name element
118.27	BPM 20V	155.06	dipole 18
118.69	MQT 28	156.06	BPM 25H
119.22	SH 25	156.40	MXL 16
119.50	SV 26	158.41	BPM 26V
121.23	TPA	158.56	BPM 26H
124.97	SV 28	159.89	dipole 19
125.24	SH 27	161.10	SH 35
125.77	MQT 29	161.44	MQU 19
126.26	MXL 13	162.98	dipole 20
126.77	MQT 30	164.04	BPM 27H
127.19	scraper 4Y	164.20	BPM 27V
127.62	MQT 31	164.52	MQU 20
128.05	BPM 21H	164.90	MXL 17
128.20	BPM 21V	165.69	SV 36
128.62	MQT 32	166.82	SH 37
132.40	SH 29	167.77	MQU 21
132.67	BPM 22H	167.90	BPM 28H
132.83	BPM 22V	168.08	BPM 28V
133.11	MQU 13	169.31	dipole 21
134.65	dipole 13	170.55	MXL 18
135.71	BPM 23H	170.85	MQU 22
135.88	BPM 23V	171.16	SV 38
136.19	MQU 14	172.39	dipole 22
136.49	SH 30	173.65	SH 39
137.73	dipole 14	175.83	BPM 29H
140.81	SH 31	175.99	BPM 29V
141.56	electrostatic septum	177.22	dipole 23
142.56	dipole 15	178.76	MQU 23
144.10	MQU 15	179.10	SH 41
144.42	MXL 14	180.31	dipole 24
145.65	dipole 16	181.85	MQU 24
146.71	BPM 24H	182.12	BPM 01H
146.87	BPM 24V	182.27	BPM 01V
147.19	MQU 16	182.53	SV 40
147.82	SV 32		
148.15	magnetic septum		
149.43	SH 33		
150.05	MXL 15		
150.44	MQU 17		
151.98	dipole 17		
153.52	MQU 18		
153.82	SV 34		

Summary

In this thesis the proton accelerator COSY is described. It consists of a cyclotron in which H^- is accelerated upto 45 MeV. After stripping injection the protons are accelerated to energies between 0.175 GeV and 2.5 GeV in the synchrotron.

In chapter one the layout of the accelerator is described concisely. In the next chapters the particle trajectories with respect to the reference trajectory are calculated. First, the magnetic field is given to be ideal. Then, a numerical model is presented in which calibration factors for several elements are fitted. In the subsequent chapters the deviations from the ideal magnetic field distribution are added to the description. Finally, the influence of the magnetic field deviations are calculated with analytical and numerical tools and then compared with measurements.

An extensive first-order study of beam properties of COSY is given. For the calibration of the quadrupole magnets, correction magnets and beam position monitors (BPM's) a fit-procedure is applied. Firstly, the beam position is measured at all BPM's. Secondly, the beam position is shifted by applying a current on a single steerer magnet. This routine is repeated for all individual correction magnets. Finally, the measurements are compared with orbit calculations. The origin of the differences between the calculations and measurements lies in the calibration errors of the quadrupole magnets, steerer magnets and BPM's. With a fit-procedure in which the calibration constants are changed, the deviations between measurements and calculations is minimised to errors smaller than the measurement inaccuracy (< 0.2 mm). For example, the fitted calibration constants for the steerer magnets yields an improvement for the closed orbit control. A numerical study to determine the influence of fringing fields of the magnets is done. It shows that the fringing field of a magnet is changed when it is the neighbourhood of another magnet thus accounting for the change of calibration factors for the magnets.

Furthermore, attention is paid to misalignments of dipole and quadrupole magnets on the particle trajectory. The transverse magnetic field distribution is determined from the magnetic field measurements in the median plane. Numerical calculations show the influence of the measured magnetic field deviations on the transverse motion of the particles. For example, the tune-shift of the dipole magnets due to field errors is about 0.037 (for a given experimental setup) and calculations show a tune-shift of 0.043. The magnetic fields errors of second-order (sextupole component of the dipoles) can be compensated with separate sextupole magnets.

Attention is paid to a general theory that describes the influence of resonances and coupling terms on the particle motion. Hamilton mechanics is used for this theory. After canonical transformations Hamilton equations are obtained that describe individual resonances. Several resonances are investigated experimentally.

The non-linear equations of motion can be solved using Lie algebraic tools. This theory is applied to solve the motion of the protons upto second-order. With correction magnets the Hamilton coefficients of third-order can be measured (one order higher then the equations of motion). With two horizontal and two vertical steerer magnets a sinusoidal signal, each with an other frequency, is applied to the beam. The frequency response of the beam is measured with BPM's. The non-linear behavior is present when sum- and difference frequencies of the excitation frequencies are visible. Particle motion as function of non-linear magnetic fields can be studied by changing the sextupole strength. Variation of the amplitude of the excitation frequencies yields information about the size of the Hamilton coefficients.

Samenvatting

In dit proefschrift wordt de protonenversneller COSY beschreven. De voorversneller is een cyclotron waarin H^- wordt versneld tot 45 MeV. Na stripping injectie worden protonen versneld in de synchrotronring in een energiegebied van 0.175 GeV tot 2.5 GeV.

In hoofdstuk 1 wordt een korte inleiding over de versneller gegeven. In de volgende hoofdstukken worden de deeltjesbanen, relatief ten opzichte van een referentiebaan, berekend waarbij het magneetveld in eerste orde ideaal is. Vervolgens wordt een numeriek model gepresenteerd waarin elementen aan de hand van metingen gekalibreerd worden. In de verdere hoofdstukken worden de niet ideale magneetvelden aan de beschrijving toegevoegd. Daarna worden de eigenschappen van deze magneetvelden theoretisch en numeriek berekend en met metingen vergeleken.

Er wordt een uitgebreide, eerste orde studie van de bundeldynamica in COSY gegeven. Voor de kalibratie van de quadrupolen, correctiemagneten en monitors van de bundelpositie (zogenaamde BPM's) is een fit-procedure toegepast. Hierbij wordt de bundelpositie bij alle BPM's gemeten. Daarna wordt de bundel verschoven met behulp van een enkele correctiemagneet. Dan wordt de bundelpositie in de ring opnieuw gemeten. Dit wordt voor alle correctiemagneten herhaald. Alle metingen worden vergeleken met corresponderende berekeningen. De verschillen tussen de berekeningen en metingen ontstaan door verkeerde kalibraties van de quadrupolen, correctiemagneten en BPM's. Door een fitprocedure worden de verschillen geminimaliseerd en de kalibratieconstanten bepaald. Er is een numerieke analyse gemaakt over de afhankelijkheid van de kalibratieconstanten en de afstand van naast elkaar liggende magneten. Het magnetische randveld van een magneet wordt veranderd als het in een gebied dringt waar een andere magneet werkzaam is.

Verder is het effect van uitlijnfouten van de buigmagneten en quadrupolen op de deeltjesbaan onderzocht. Uit metingen van de magneetveldverdeling in het mediaanvlak van de afbuigmagneten zijn de niet-ideale magneetvelden bepaald. Uit numerieke berekeningen van de transversale bewegingen volgt de invloed van deze magneetvelden van hogere orde. De magneetvelden van tweede orde kunnen worden gecompenseerd door sextupolemagneten die zich in de deeltjesversneller bevinden.

Er is aandacht besteed aan een algemene theorie voor de beschrijving van de invloed van resonantie- en koppelingseffecten op de deeltjesbeweging. Voor het opstellen van deze theorie is gebruik gemaakt van het Hamiltonformalisme. Na het

toepassen van een aantal transformaties worden Hamiltonfuncties verkregen waarin verschillende effecten zichtbaar zijn. Een aantal transversale koppelresonanties zijn experimenteel onderzocht.

De niet-lineaire vergelijkingen van deeltjesbeweging kunnen met behulp van Lie-algebra opgelost worden. Deze theorie is toegepast om de baanvergelijkingen van tweede orde op te lossen. Met behulp van de correctiemagneten kunnen de Hamiltoncoëfficiënten (een orde hoger dan de baanvergelijkingen) gemeten worden. Twee horizontale en twee verticale correctors geven een sinus-vormig signaal met een bepaalde frequentie op de bundel (4 verschillende frequentie's). De frequentie respons van de bundel wordt met behulp van de BPM's gemeten. Het niet-lineaire gedrag van de deeltjesbaan is zichtbaar door het verschijnen van som- en verschil frequentie's. Door variëren van niet-lineaire magneetvelden (sextupolemagneten) kan inzicht verkregen worden over de deeltjesbeweging. Door de amplitude van het excitatie signaal te variëren verkrijgt men informatie over de Hamiltoncoëfficiënten.

Nawoord

Het promotie-onderzoek is verricht aan het Forschungszentrum Jülich in de periode van januari 1995 tot en met december 1997. Tijdens de promotie is er veel samenwerking met de versnellergroep van de vakgroep Deeltjesfysica van de Technische Universiteit Eindhoven geweest. Hierbij wil ik iedereen bedanken die bijgedragen heeft aan het totstandkomen van dit proefschrift voor zijn of haar enthousiasme en de plezierige samenwerking.

Dr. R. Maier heeft ervoor gezorgd dat ik de mogelijkheid heb gehad om me bij COSY zelfstandig te ontwikkelen tijdens het promotieonderzoek. Anderen, zoals Ulf Bechstedt, Jan Botman, Jürgen Dietrich, Sig Martin, Dieter Prasuhn, Alexander Schnase, Herbert Schneider, Jochen Stein en Hans Stockhorst ondersteunden me door hun specialistische kennis op velerlei gebied bij het onderzoek in te zetten.

Het uitvoeren van nachtdiensten is mede mogelijk gemaakt door de operators die steeds van dienst geweest zijn. Daarnaast wil ik Andreas Lehrach en Raymond Tölle noemen die mij zowel vakinhoudelijk als persoonlijk gesteund hebben tijdens de promotie.

Het is ondoenlijk al degenen die in meerdere of mindere mate aan het onderzoek hebben bijgedragen hier met name te noemen en persoonlijk te bedanken. Daarom volsta ik met het zeggen dat ik het werkklimaat bij COSY altijd als zeer prettig heb ervaren, en wil hiervoor alle collega's mijn hartelijke dank betuigen.

Danksagung

Die vorliegende Arbeit entstand in den Jahren 1995-97 am Institut für Kernphysik des Forschungszentrums Jülich. Während der Promotion gab es eine intensive Zusammenarbeit mit der Arbeitsgruppe Beschleunigerphysik der Technischen Universität Eindhoven. Ich danke allen, die zur Entstehung dieser Arbeit beigetragen haben für ihre Begeisterung und die gute Zusammenarbeit.

Herr Dr. R. Maier bot mir die Möglichkeit der freien Entfaltung während der Promotion. Dr. U. Bechstedt, Dr. J. Botman, Dr. J. Dietrich, Dr. S. Martin, Dr. D. Prasuhn, Dr. A. Schnase, Dipl. Ing. H. Schneider, Dr. J. Stein und Dr. H. Stockhorst unterstützten mich durch ihre Fachkenntnisse.

Die COSY-Operateure haben bei der Durchführung von Maschinenexperimenten mitgeholfen. Zudem möchte ich A. Lehrach und Dr. R. Tölle nennen, für zahlreiche Diskussionen und die freundschaftliche Atmosphäre.

Ich möchte auch den hier nicht genannten herzlich danken, die zu dieser Arbeit beigetragen haben. Die Aufnahme in das COSY-Team und das Arbeitsklima habe ich als sehr freundlich empfunden, wofür ich mich nochmals ganz besonders bedanken möchte.

Curriculum Vitae

- 27 juli 1968 Geboren in Heerlen
- 1980 - 1988 HAVO, VWO aan het Coriovallum College te Heerlen
- 1988 - 1994 Studie Technische Natuurkunde aan de
Technische Universiteit Eindhoven
- 1995 - 1997 Promovendus, werkzaam in Forschungszentrum Jülich GmbH,
Duitsland

Publications

European Particle Accelerator Conference:

- Webers, G.A., L.H.A. Leunissen, J.I.M. Botman, H.L. Hagedoorn, J.L. Delhez, Electron optical properties of the Eindhoven race-track microtron, EPAC 94, London. p.1042
- Tölle, R., Bechstedt, U., Dietrich, J., Lehrach, A., Leunissen, L.H.A., Maier, R., Martin, S., Prasuhn, D., Schnase, A., Schneider, H., Stockhorst, H., Conditioning the Cooler Synchrotron COSY for internal experiments, EPAC 96, Barcelona, p.572

Spin '96:

- A. Lehrach, U. Bechstedt, R. Bollmann, K. Büsser, O. Diehl, J. Dietrich, P.D. Eversheim, R. Gebel, F. Hinterberger, L.H.A. Leunissen, R. Maier, S. Martin, D. Prasuhn, H. Rohdjess, A. Schnase, H. Schneider, V. Schwarz, H. Stockhorst, R. Tölle, Status of Polarized Beam at COSY, Spin '96 Amsterdam, p.416

International Committee for Future Accelerators:

- U. Bechstedt, J. Dietrich, A. Lehrach, L.H.A. Leunissen, R. Maier, S. Martin, D. Prasuhn, A. Schnase, H. Schneider, H. Stockhorst, R. Tölle, The COoler SYnchrotron: COSY, ICFA Beam Dynamics Newsletter No. 13 (1997), p.39
- L.H.A. Leunissen, Beam dynamics experiments using the electron cooled beam at COSY, p.21

Annual report 1995 (Institut für Kernphysik Jül-3200):

- Experiment investigation of amplitude dependent tune, p.229
- Chromaticity measurements at COSY, p.231
- First vertical beamsize measurements, p.233
- Numerical models for COSY, p.258

- Closed orbit description in COSY, p.259

Annual report 1996 (Institut für Kernphysik Jül-3365):

- Calibration procedure for the COSY-accelerator, p.215
- Calibration measurements for the COSY-accelerator, p.217
- Dynamic aperture in COSY-accelerator, p.222
- Magnetic multipole components of COSY-dipoles, p.224
- Induced magnetic field between magnets in COSY lattice, p.226
- Tuning of the COSY telescopes, p.228
- Determination of third-order Hamilton coefficients, p.233
- Measurement of third-order Hamilton coefficients, p.235
- Supporting Accelerator Operation by Application Programs, p.238

Stellingen

behorende bij het proefschrift

**Non-linear transverse dynamics
at the Cooler Synchrotron COSY**

door

Leonardus Hendrikus Albertino Leunissen

Eindhoven, 8 december 1997

- I -

Versnellers worden zo compact mogelijk gebouwd. Daardoor is de magnetische beïnvloeding van naast elkaar gelegen magneten niet meer te verwaarlozen en voldoen de magneten niet meer aan hun specificaties.

dit proefschrift, hoofdstuk 3

- II -

Bij het versnellen van gepolariseerde protonen worden twee onafhankelijke soorten van sterk depolariserende resonanties gepaseerd. Er zijn verschillende methodes om verlies van polarisatie door deze resonanties te voorkomen. Alleen met een zogenaamde "Siberische slang" is het mogelijk om beide soorten depolarisatie te voorkomen.

A. Lehrach, Erarbeitung und Umsetzung eines Konzepts zur Beschleunigung polarisierter Protonen in COSY, proefschrift Universiteit van Bonn

- III -

Bij het gebruik van wetenschappelijke programmatuur dient men erop te letten dat de berekende resultaten niet juist behoeven te zijn. Het komt regelmatig voor dat zogenaamde "bugs" in programmatuur aanwezig zijn. Om inzicht te krijgen in een programma is het noodzakelijk om analytische methoden te gebruiken.

- IV -

Voor het bedrijven van ingewikkelde machines, zoals de elektronenkoeler in COSY, dient men veel tijd te investeren om de invloed van de bedieningsparameters te leren kennen. Eenvoudig proberen werkt in dit soort gevallen niet.

- V -

De toenemende mogelijkheden van het internet leiden tot een sterke toename van dataoverdracht. Het gevolg hiervan is dat de overdrachtssnelheid van informatie sterk moet toenemen om aan "de vraag" te voldoen. Gebruikers moeten daarom wederom steeds snellere computers en communicatielijnen aanschaffen.

- VI -

Voor bestraling van tumoren kan een protonenbundel beter gebruikt worden dan röntgenstraling.

- VII -

De 'exact envelope function theory' zoals afgeleid door Mike Burt heeft serieuze consequenties voor de dispersierelaties in vergelijking met wat men berekent als de oude randvoorwaarden gebruikt worden.

P.N. Stavrinou, R. van Dalen, Operator ordering and boundary conditions for valence band modelling; Application to [110] heterostructures, Phys.Rev. B 55 24 (1997)

- VIII -

Voor de verdere ontwikkeling van een bestaande deeltjesversneller is het raadzaam een kleine commissie van wetenschappers in te stellen. Deze dienen onafhankelijk van de reguliere diensten de mogelijkheid te hebben om metingen aan de versneller door te voeren om aan hand daarvan nieuwe ideeën te opperen en de verdere ontwikkeling te bevorderen.

- IX -

In de praktijk blijken benaderende analytische uitdrukkingen een goede benadering van de gemeten resultaten bij gecompliceerde machines te geven.

- X -

Voor de beschrijving van bundeloptiek is deeltjesversnellers wordt gebruik gemaakt van klassieke mechanica. Voor toekomstige deeltjesversnellers waarbij de energie van de bundel steeds groter wordt, de emittantie steeds kleiner wordt en de briljantie steeds hoger, wordt een quantummechanische behandeling van de bundeloptiek belangrijk.

R. Jagannathan, S.A. Khan, Quantum Mechanics of Accelerator Optics, Beam Dynamics Newsletters 13